

N-Heterocyclic Carbenes and their applications for nanomaterials

Rossella Mascia

Thesis submitted to the University of Nottingham for the degree of Master of Philosophy

September 2017



This Thesis is dedicated to my parents and my sister the most important people in my life.

Abstract

This thesis reports on the synthesis of **metallic Ni nanoparticles (NiNP) stabilised by N-heterocyclic carbenes (NHCs) carbene and trioctylphosphine (TOP)**. The synthetic procedure is based on the formation of a nickelacetylacetonate-oleylamine complex followed by the addition of the stabiliser. The NHCs are synthesised using two precursors; 2,6-dibromopyridine and benzimidazole. The precursors undergo alkylation to form the final product used as stabilising agent (capping agent). The stabilisers are chemically and physically characterised by NMR (Nuclear Magnetic Resonance), MS (Mass Spectrometry), CHN elemental analysis, TGA (Thermo Gravimetric Analysis) and XPS (X-Ray Photoemission Spectroscopy). TGA allows a comprehensive understanding of their thermal stability properties at varies temperature ranges. XPS analysis has been shown as a powerful tool to probe the electronic environment of the ionic compound structures, which allows correlating the binding energy to the different types of elements presents. Both the C1s and the N1s fitting models for the $[(C_nBzIm)_2Py]X_2$ are presented. The symmetry of the molecule represents a unique opportunity to assess the fitting model of the NHCs previously investigated only for geminal ILs. The new nickel nanoparticles are synthesised through thermal decomposition of nickel acetylacetonate-oleylamine complex. To identify the morphology of the NiNPs complementary electron and spectroscopy techniques are used. The Ni-NHCs and Ni-TOP nanoparticles are inserted in graphitised nanofibers using a well-known filling technique based on capillary forces. The new hybrid structures NiNPs@GNF are tested to tentatively explore their potential applications as electrochemical nanoreactors.

Abbreviations and Acronyms

B.E.	Binding energy
$CDCl_3$	Chloroform-deuterated
CD_3OD	Methanol-deuterated
CNT	Carbon nanotubes
CPS	Counts per second
DCM	Dichloromethane
DIPP	2,6-diisopropylphenyl
D_2O	Deuterium oxide
DMSO	Dimethyl sulfoxide
e.g.	for example
ESI-MS	Electrospray Ionisation Mass Spectrometry
et al.	and others
Et_2O	Ethanol
E-/Z-	Entgegen (Opposite) and Zusammen (Together)
eV	Electron volts
FWHM	Full Width at Half Maximum
GNF	Graphitised nanofibers
Hr	hour
Hz	Hertz
h	Planck's constant (=$6.626 \cdot 10^{-34}$ m^2 kg s^{-1})
IL	Ionic liquid
J	Coupling constant
K.E.	Kinetic energy
LMMG	low molecular mass gelator
mbar	millibar
MeOD	Methanol deuterated
Min	Minutes
M-NP	Metal nanoparticle
m/z	Mass charge ratio
n	number of carbons in alkyl chain in cations
NHCs	N-Heterocyclic carbenes
NMR	Nuclear magnetic resonance
NP	Nanoparticle

ORR	oxygen reduction reaction
ppb	Parts per billion
ppm	Parts per million
RSF	Relative sensitivity factor
SILP	Supported Ionic Liquid phase
SILPs	Supported Ionic Liquid Particles
SWNT	Single-walled Nanotube
TEM	Transmission Electron Microscopy
THF	Tetrahydrofuran
TOPs	Tryoctyl phosphines
UHV	Ultra high vacuum ($p \leq 1\ 10^{-8}$ mbar)
XPS	X-Ray photoemission spectroscopy
δ	Chemical shift
φ_s	Work function
λ	Mean free path
-ve	Negative
+ve	Positive
@	Into

Acknowledgements

Firstly, I would like to thank my supervisors, Prof. Andrei Khlobystov and Prof. Peter Licence for supporting me and proof reading this thesis.

I am indebted thankful Dr. Emily Smith for XPS training, help with data interpretation and stimulating conversation throughout the past 3 years.

I am deeply thankful to Ejike for help with Igor Pro, peak fitting who has also provided friendship, support and encouragement throughout my research.

I would like to thank Dr. Craig Stoppiello and Rhys Lodge for carrying out TEM measurements.

I would like to thank Thomas Bradley for the electrochemistry experiments.

For inspiring my interest in nanoscience research, I am grateful to Dr. Alessandro who also provided love, endless encouragement and support.

I must also thank the technical staff and IT service for all of their help, especially Mark, Clive and Pvail.

I am also grateful to all the people who supported me since the beginning, particularly Amalina, Ejike, Coby and Simona.

Finally, I would like to thank my family for all of their love and support throughout these three years. Without their constant love and support, this thesis would not have been possible.

Table of Contents

Abstract ... 3

Abbreviations and Acronyms ... 4

Chapter 1 ... 11

Introduction ... 11

1.1 Introduction ... 12

1.2 Aims and Objective of the literature review ... 15

1.3 Ionic Liquids ... 15

1.3.1 Ionic liquids metal nanoparticles ... 17

1.3.2 Supported Ionic Liquids ... 19

1.4 N-Heterocyclic Carbene ... 20

1.4.1 Low-molecular-mass gelators ... 21

1.5 Nanoparticles in hollow carbon nanostructures ... 22

1.5.1 Catalytic activity of metal nanoparticles inserted into composite material ... 28

1.6 X-Ray Photoemission Spectroscopy of Ionic Liquids ... 29

1.7 Aims and objective of this thesis ... 31

1.8 Bibliography ... 33

Chapter 2 ... 39

2.1 Introduction ... 40

2.2 Materials and Instrumentation ... 40

2.2.1 X-Ray photoemission spectroscopy: experimental record ... 41

2.3 Synthesis of Pyridine-Bridged Benzimidazolium salts ... 42

2.3.3 2,6-Bis(benzimidazole)pyridine, $(BzIm)_2Py$ from 2,6-dibromopyridine ... 42

2.3.4 2,6-Bis(benzimidazole)pyridine, $(BzIm)_2Py$ from 2,6-dichloropyridine ... 42

2.3.5 2,6-bis(octylbenzimidazolium) pyridine dibromide, $[(C_8BzIm)_2Py]Br_2$ ... 43

2.3.6 2,6-bis(Octylbenzimidazolium)$_2$pyridinetetrafluoroborate, $[(C_8BzIm)_2Py][BF_4]_2$ ... 44

2.3.7 2,6-bis(Octylbenzimidazolium) pyridine bis(trifluoromethylsulfonyl)amide, $[(C_8BzIm)_2Py][PF_6]_2$ ... 45

2.3.8 2,6-bis(octyllbenzimidazolium)pyridine bis(trifluoromethylsulfonyl)amide, $[(C_8BzIm)_2Py][NTf_2]_2$ ... 46

2.3.9 2,6-bis(butylbenzimidazolium)$_2$pyridine dibromide, $[(C_4BzIm)_2Py]Br_2$ ... 47

2.3.10 2,6-bis(butylbenzimidazolium)$_2$pyridine tetrafluoroborate, [(C$_4$BzIm)$_2$Py][BF$_4$]$_2$ 48

2.3.11 2,6-bis(butylbenzimidazolium)$_2$pyridine hexafluorophosphate, [(C$_4$BzIm)$_2$Py][PF$_6$]$_2$ 49

2.3.12 2,6-bis(butyllbenzimidazolium)pyridine bis(trifluoromethylsulfonyl) amide, [(C$_4$BzIm)$_2$Py][NTf$_2$]$_2$ 50

2.3.13 2,6-bis(dodecylbenzimidazolium)$_2$pyridine dibromide, [(C$_{12}$BzIm)$_2$Py]Br$_2$ 51

2.3.14 2,6-bis(dodecylbenzimidazolium)$_2$pyridine tetrafluoroborate, [(C$_{12}$BzIm)$_2$Py][BF$_4$]$_2$ 52

2.3.15 2,6-bis(dodecylbenzimidazolium)$_2$pyridine hexafluorophosphate, [(C$_{12}$BzIm)$_2$Py][PF$_6$]$_2$ 53

2.3.16 2,6-bis(dodecylbenzimidazolium)pyridine bis(trifluoromethylsulfonyl) amide, [(C$_{12}$BzIm)$_2$Py][NTf$_2$]$_2$ 54

2.4 Synthesis of nickel nanoparticles 55

2.4.1 Nickel phosphorus stabilised nanoparticles 55

2.4.2 Nickel N-Heterocyclic Carbene stabilised nanoparticles 55

2.5 The encapsulation of nanoparticles into hollow carbon nanostructures 56

2.5.1 Insertion of nickel nanoparticles into multiwalled carbon nanofibers 56

2.6 Material characterisation techniques 56

2.6.1 Sample handling 56

2.6.2 Chemical analysis 57

2.6.3. Material characterisation techniques 62

2.6.4. Thermogravimetric analysis 69

2.6.5 Gas Chromatography Mass Spectrometer 70

2.6.6 Nuclear magnetic resonance 70

2.6.7 Elemental Analysis 71

2.6.8 Electrochemistry 71

2.6.8.2 Technical details of the electrochemical experiments 74

2.6.9 Data handling 75

2.7 Summary 78

2.8 Bibliography 79

Chapter 3 81

3.1 Introduction 82

3.2 Aim and objectives 82

3.3 Ligand synthesis 84
3.3.1 2,6-Bis(benzimidazole)pyridine, [2,6-bis(BzIm)$_2$Py] 84
3.3.2 Alkylation reaction of ligand structures 86
3.3.3 Anionic exchange reactions 86
3.4 Thermogravimetric studies 87
3.5 X-ray Photoemission Spectroscopy of bis(benzimidazolin-2-ylidene) salts 92
3.5.1 Wide and high resolution scan 93
3.5.2 Peak fitting the [(C$_8$BzIm)$_2$Py]X$_2$ C 1s region 99
***3.5.3* Peak fitting the [(C$_n$BzIm)$_2$Py][Ntf$_2$]$_2$ C 1s region** 103
3.5.4 Effect of the anion on the cation 104
3.6 Conclusion and future studies 106
3.7 Bibliography 107
Chapter 4 109
4.1 Introduction 110
4.2 Aims and objective of this chapter 114
4.3 Result and discussion 115
4.3.1 Size distribution of nanoparticles 115
4.3.2 Nickel nanoparticles stabilised by NHCs 115
4.3.3 Characterisation of the nickel nanoparticles stabilised by trioctylphosphine 116
4.3.4 Characterisation of the NiNPs stabilised by N-Heterocyclic Carbene 118
4.3.5 Comparison of TOP and NHCs stabilised nickel nanoparticles 121
4.3.6 IR Trioctyl phosphine and N-Heterocyclic Carbene stabilised Nickel nanoparticles 124
4.4 Encapsulation of nickel nanoparticles into multi-walled nanofibers: host-guest interactions 125
4.4.1 Insertion of nickel nanoparticles into graphitised nanofibers ... 127
4.4.2 Insertion of NiNPs stabilised by N-Heterocyclic carbene into graphitised nanofibers 129
4.4.3 TEM Imaging: EDX mapping on nanoparticles 132
4.5.1 Testing the catalytic activity of the Nickel nanoparticlesfor the oxidation of propargyl alcohol 135
4.6 Summary and future work 141
4.7 Bibliography 143

Conclusions and future work 147
Bibliography 151
Appendix 152

Chapter 1

Introduction

1.1 Introduction

The craftsmen of the ancient eras 'unconsciously' were skilled at manufacturing nanomaterials. They were working in a branch of nanotechnology called nanocomposites known as well as nano hybrid materials, in which bulk materials were combined with nanoparticles and or carbon nanostructures. The combination of nano and bulk materials resulted to improve the functional properties of the hybrid/composite materials. One of the most notorious examples of ancient artefacts containing nanocomposites was the Lycurgus cup, which was an exquisite decorative Roman treasure made about A. D. 400. The peculiar feature of the cup was a glass which changes colour when light was shone through it. The glass was containing noble metals (gold, silver) nanoparticles, which were arranged in such a way to make the glass look green in reflected light but, when light passes through the cup, it shown a brilliant red.[1,2] There were other examples such as Damascus steel swords in the Middle East made between A.D. 300 and A.D. 1700. They were known for their impressive strength, shatter resistance and exceptionally sharp edges. The steel blades contained oriented nanoscale wire and nanotube like structures.[3] The Renaissance Mediterranean world pottery was often decorated with lustre (iridescent metallic glaze), containing silver and copper nanoparticles responsible for their optical properties.[4] Craftsmen were not aware of the science behind either the exceptional strength of the swords or the optical properties of the potteries. Craftsmen were passing their skills and know-how down through generations. Nowadays, nanotechnologists can build on this ancient wisdom. They possess state of the art fabrication tools and analytical instruments to get a greater understanding of the science behind nanoentities and their properties. This allowed nanotechnologist to achieve exciting new products and device faster than the craftsmen in the ancient era.

Nanoparticles are capable to act as a bridge between bulk materials and atomic or supermolecular structures. The physical properties of bulk materials are not in function of their size or mass.[1] Conversely, nanoparticles show size dependent properties due to the considerable

amount of surface versus atoms as compared to the bulk. This leads to a large specific surface, as shown in Figure 1.1.[5]

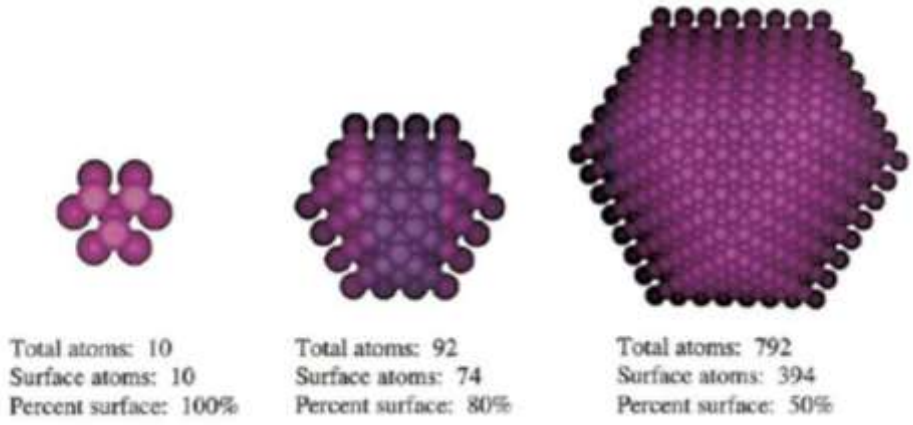


Figure 1.1 Schematic representation of surface to bulk atoms of NPs with different scales, 10 atoms, 92 atoms and 792 atoms.[6]

The functional properties of particles change as their size decrease towards the nano-meter level. Accordingly, the control of the nanoparticle size is related to the possibility of influencing their functional properties. The additional properties of NPs that dictate their microscopic and macroscopic behaviours are summarized in Figure 1.2.[6]

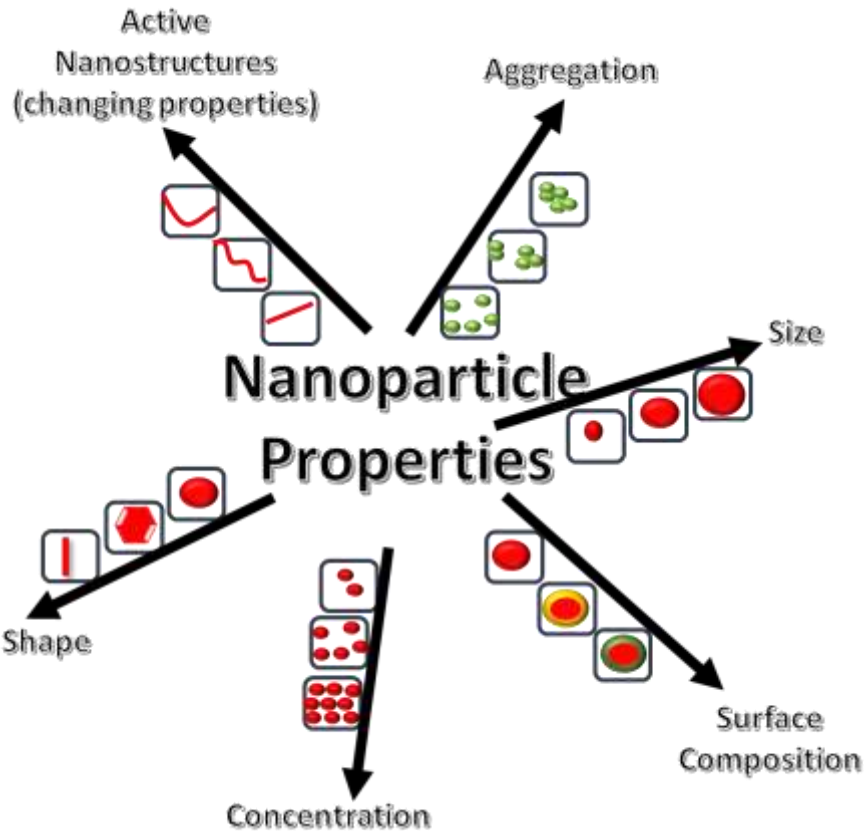


Figure 1.2 Schematic representation of the nanoparticle properties.

Nanoparticles can be divided into categories capped and uncapped. The advantages of having capped nanoparticles are their controllable size and the presence an external defined protective layer strongly connected to the particle. The capped NPs contains organic layers that prevent the corrosions of transition metals such Ni, Fe, Co etc.[7] The organic layer might also prevent the direct contact between the particles with the support, avoiding any carbonization and etching of the support as shown already for uncapped or corroded metal transition particles residing on carbon supports.[8-10] The synergetic effect between the metal core and the capping layer might unveil unprecedented functional properties. The metal core can also be used as a template and as a catalyst to the transformation of the capping layer to carbon cups in a solid-state reaction in airless condition for potential magnetic, optical and catalytic applications.[11]

1.2 Aims and Objective of the literature review

The main aim of the literature review is to generate a scientific perspective of the complex field of the ILs–M-NPs interactions, which are of fundamental importance for the grafting of NPs stabilised in ionic liquid media. Different synthetic approaches and properties are discussed in section 1.3. A brief survey of the applications of ILs systems in Section 1.3 clearly illustrates the great potential of this type of ionic materials.

Some formidable challenges, related to the use of metal nanoparticles in combination with ionic liquids, still need to be resolved in order to avoid catalyst losses, loss of catalytic activity and recyclability. This project is set to tackle these outstanding problems in ILs applied in catalysis using NHC ligands to stabilise metallic nanoparticles. These categories of compounds are often not classified as ILs due to their physical status at room temperature, as they are normally solids. Moreover, the typical problems of ILs faced in catalysis can be overcome by attaching the NHCs stabilised nanoparticles to a carbon support to form a nanoreactor with extremely good retention on the carbon surface due to electrostatic interaction with the reacting substrate enhanced by the nanoconfinement. To compare the effect of the stabiliser on the morphology of the particles, it is synthesised a second type of NiNP using the same synthetic approach although stabilised with a commercial solution of trioctyl phosphine (TOP). The NiNPs-TOP are also attached to a carbon support. The two new nanoreactors aim to solve the outstanding problem of selectivity, stability and recyclability of metal catalyst and its support, an issue that has a global impact.[12]

1.3 Ionic Liquids

Ionic liquids (ILs) are liquids that consist exclusively of ions, typically organic salts. The term “Ionic liquids” generally indicates compounds that are liquid below 100 °C.[13] They possess negligible vapour pressures and can be mixed together to obtain mixture with different physical and chemical properties.[13,14] ILs are ideal alternative to aqueous and toxic flammable volatile organic solvents. They contribute to waste prevention, safety of chemical process and products, placing these materials at the forefront of green application.[14-17] The physical and chemical properties can be tuned by exchanging anions and cations and designing specific

functionalities into them.[15] They are constituted normally by nitrogen or phosphorus organic cation with alkyl chains. One of the most common is the 1-alkyl-3-methylimidazolium cation, whereas the most common anions cited in the ionic liquid literature are Br^-, Cl^-, $[PF_6]^-$ and $[BF_4]^-$. Several uses are possible in catalysis, organic synthesis, nanoparticles and transition metal complexes.[12,17-21]

Ionic liquids are compounds that start to be engineered and studied as not just solvents but as ligands, co-catalysts, and stabilizing agents of catalytic cycles.[12] The advantages of ILs in both homogeneous and heterogeneous catalysis are presented in several reactions e.g. hydroformylation, olefins metathesis and cross coupling reactions.[12,22,23] These reactions represent very important tools in the organic synthesis. The most common catalysts are Ruthenium or Palladium in a homogeneous phase. [24,25] In order to overcome the problem of the separation of the product from the reaction mixture a biphasic system is considered where ionic liquids are able to dissolve the substrates. [24, 22] Despite improvements of the synthesis with the utilisation of ILs, mass transfer limitations sometimes caused negligible solubilisation of the reagents. This problem is significantly overcome, introducing ionic moiety in the catalytic skeleton to assure better dissolution withing ILs medium.[12,26]

Supported ionic liquid materials have been prepared using amorphous silica or alumina as support and studied their catalytic properties for olefin metathesis.[27] Unfortunately, leaching of the immobilised transition metal catalysts/complexes from ILs can occur eventually, and thus reducing their catalytic activity. Answers to these problems are required in order to improve the olefin metathesis in ILs. [12,27] A trivial application of ionic liquids in organic synthesis is represented by catalyst nanoparticles where remarkably the Heck reaction is performed with Palladium nanoparticles in ILs medium.[12] The precursor of palladium forms a cluster of metallic palladium which takes active part in the transformation and the reaction medium is represented by ionic liquids which stabilise the nanoparticles.[28] Interesting, porphyrin-functionalised ligand in butylpyridine tetraboron phosphate shows catalytic activity enhanced by a strong ionic and π-π interactions between the catalyst and the ILs.[29]

Homogeneous catalysis, despite its proficiency in terms of selectivity and activity compared to heterogeneous catalysis, shows a clear deficiency on separation and recycling of the catalyst.[30] Nevertheless, the heterogeneous catalysis optimized synthesis can be developed with a small amount of ILs, that despite of their overlooked qualities present 'non green' attributes as toxicity and non-biodegradability.[13,14,31- 34]

1.3.1 Ionic liquids metal nanoparticles

Metal nanoparticles can be synthesised in ionic liquids (ILs) matrix without any additional stabilisers. The electrostatic and steric properties of ILs allow the stabilization of particles without the need of surfactants, polymers or capping ligands, Figure 1.3.[35]

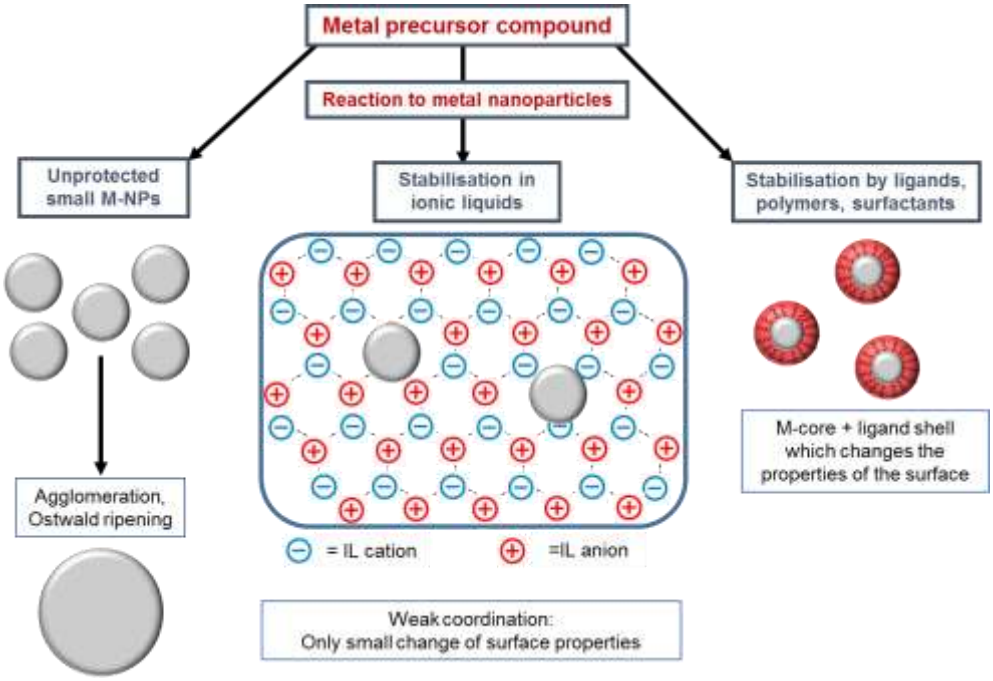


Figure 1.3 Representation of the formation of metal nanoparticles (M-NPs) in three case scenario: unprotected small M-NPs agglomerates to larger nanoparticles unless prevent electronic and steric stabilisation in ionic liquids or stabiliser.

ILs acts as a nano-templates that stabilises metal nanoparticles on the basis of their ionic nature, high polarity, high dielectric constant and supramolecular network, without the need of additional protective ligands, Figure 1.4.[36-39] However, the lack of the stabiliser (capping agent) results in

the leaching of the immobilised metal particles from the ILs reducing their catalytic activity and also limits the control of their size and shape.[40] This can be a major disadvantage as the NP functional properties are in function of their size. Some of the physical property of metal particles-ionic liquids systems such as viscosity, conductivity and mass transport are affected by the size of the charged particles and ions; larger is their size smaller is the availability of holes to them to move in. Hence, large ion size is associated to mass transport limitation due to the presence of narrow holes.

Abbot *et al.* have developed a fundamental insight into viscosity, conductivity and mass transport in all types of ionic liquids. They have shown that the large ion size means that mass transport is limited by the availability of holes for ions to move into.[41,42] This means that viscosity can be modelled using the hole theory and the conductivity can be modelled using a Nernst Einstein model because the holes are effectively at infinite dilution. It is shown that classical diffusion does not occur in ionic liquids with ions moving by a series of jumps between suitably sized voids.[43] In addition, the ageing and corrosion of the metal core affects the NPs-ILs system particularly their physical and chemical properties. By contrast, ligands, polymers and surfactants give a protective layer which provides steric coverage to prevent both ripening of the particles during the synthesis and their corrosion post-synthesis, Figure 1.4.[40,44] However, for catalytic application, these surfaces coverage are also associated to partial or total de-activation of the metallic part. Therefore, effort should be devoted to reach the right organic capping agent which leaves the particles surfaces activated and protected.[45]

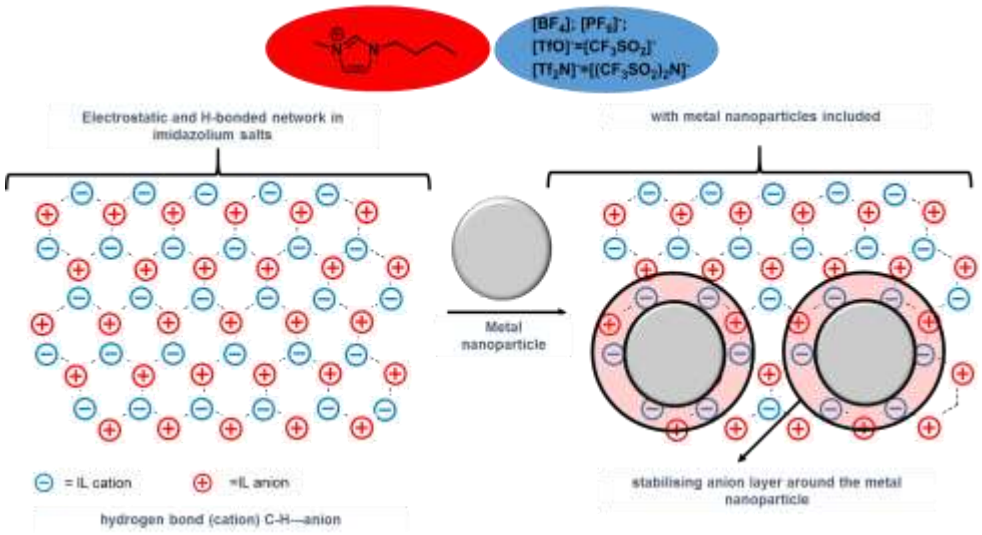


Figure 1.4 On the left, representation of the network structure of the 1,3-dialkyl-imidazolium-based ionic liquids projected in two dimensions. On the right, inclusion of metal nanoparticle in the supramolecular ILs network with electrostatic and steric stabilisation indicated through the formation of the stabilising anion layer around the metal nanoparticles.

1.3.2 Supported Ionic Liquids

The combination of the benefits of both homogeneous and heterogeneous catalysis leads to SILP (Supported ionic liquid phase). SILPs (Supported Ionic liquid particles), Figure 1.5, represent a good approach to overcome the separation problem including others favourable physical and chemical properties such as polarity, viscosity, thermal stability and solubilising power of the liquid phase on a solid bulk.[27,46]

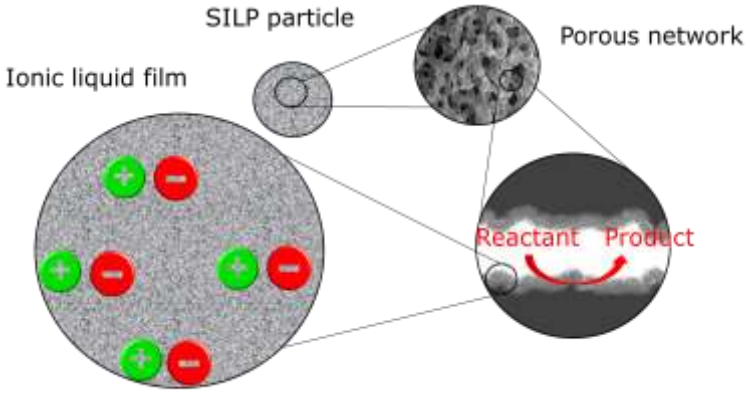


Figure 1.5 Supported ionic liquids particle (SILP): ionic liquid film on a porous network.

Solubility, partition coefficient, mass transfer are factors that can influence kinetically and thermodynamically the reaction under study. However, if the products are partially soluble in ILs media is preferable to perform the reaction in a single phase to avoid diffusional limitation and separate the products by extraction.[47] With respect of the ILs specifications, it is possible to transfer distinct properties of the fluid to the surface.[20] Hence, it is feasible to design a surface with specific defined properties and controlled chemical reactivity. ILs, functionalised with transition metal complex, can be anchored covalently on the surface of a support.[12] SILPs are good candidates as catalysts thank to their high surface area, film of liquid that avoid mass transport problem, thermal stability, and applicability in fixed bed technology and catalysis immobilisation.[48]

1.4 N-Heterocyclic Carbene

In this thesis NHCs Ionic Liquids based on the imidazole ring system are investigated which make a wide variety of ionic compounds. NHCs are knowns ligands for several transition metals.[49-54] In the field of inorganic chemistry. Low melting ionic liquid based on the imidazolium-based structures have attracted big interest in the field of transition metal complexes.[55] Numerous examples of ionic liquids are reported in the literature with copper(II), nickel(II) or cobalt(II).[55, 56] The reason why pincer ligand become very popular in transition metal catalysis is due to the extreme stability of the metal to ligand and ligand to metal interactions which includes a sigma donation bond and π-back donation bond. There are only few examples of the utilisation of symmetric NHCs ionic structures as stabiliser for nanoparticles. Perez-García *et al.* report bis-imidazolium amphiphiles to stabilise gold nanoparticles to be applied for drug delivery.[57] The compounds stabilise capped nanoparticles with a diameter between 2 and 12 nm, Figure 1.6.

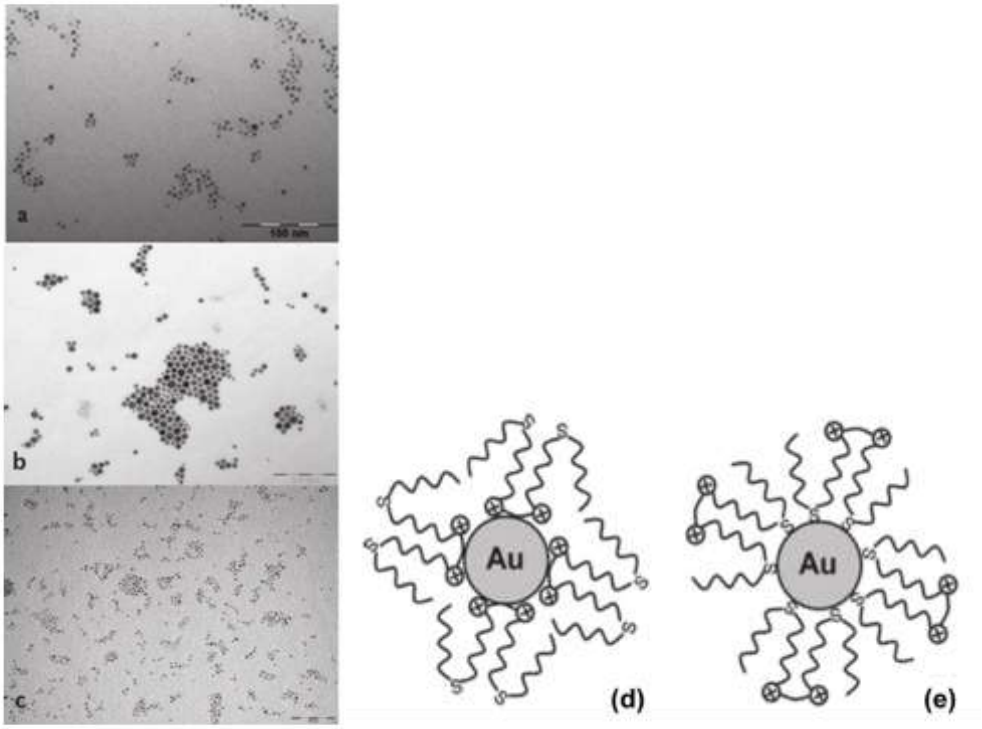
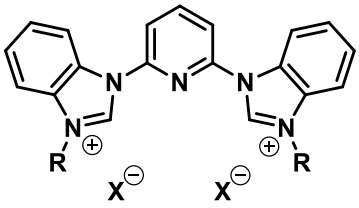


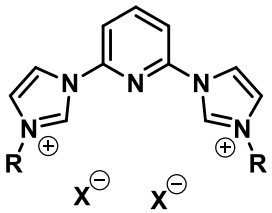
Figure 1.6 TEM pictures of the gold nanoparticles between (a) 1-5 nm (b) 8.8±2.2 and (c) 5.3±2.4 nm, scale bars are 100 nm for (a) (b) (c); some possible schematic representations of gold nanoparticles bound by imidazolium moieties (d) and S atom (e).[57]

1.4.1 Low-molecular-mass gelators

A peculiar application of NHCs benzimidazolium based structure presented in this report is reported by Tu *et al.*[58] The study is the application of a metallogel for catalytic application where a palladium complex mixed with different solvents, upon heating to reflux, realise a gelator which is applied to a model reaction. Low molecular mass gelators (LMMG) are compounds based on low molecular weight compounds.[59] They are normally made from metal complexes and small anions. The skeletons of these molecules are based on the imidazolium ring with its characteristic n-heterocyclic carbenes, Scheme 3.1.



R=n-$C_{16}H_{33}$; X=Br
R=n-$C_{16}H_{33}$; X=I
R=n-$C_{12}H_{25}$; X=I
R=n-C_8H_{17}; X=I
R=n-C_4H_9; X=I



R=n-$C_{16}H_{33}$; X=I

Scheme 3.1 Pyridine-bridged bis-benzimidazolium and bis-imidazolium salts.

Currently some reactions tested are the Suzuki-Miyaura cross-coupling reaction and the double Michael addition.[58,60] The analysis currently reported in the literature are TEM (Transmission Electron Microscopy) and crystallographic studies with particular interest in understanding the self-assembly of the molecules. Long chain substituted pincer structures form gels with a quite ordered distribution due to van der Waals interactions between the alkyl chains mainly constituted by hydrogen bonding and π stacking interactions.[61] Despite the characterisation of NHC functionalised material, little work has been done to understand the electronic distribution. XPS (X-Ray Photoemission Spectroscopy) is a useful technique to understand and study interactions between ionic and cationic moiety and how the variation of the structures might influence these interactions. This clearly opens a new perspective in the understanding of metallogel catalytic reactions which has never been analysed before with XPS. Metal free reaction has been proved for the N-alkylation suggesting the big impact of the NHCs type ligand.[61] Moreover, functionalised materials with NHCs enriched sites have been synthesised and proved for catalytic application,[62] positioning these material at the edge of the creation of powerful tool for new catalytic technologies.[63]

1.5 Nanoparticles in hollow carbon nanostructures

Nowadays, there are examples in the literature of metal nanoparticles embedded in ILs. However, the loss of the support and the leaching of the

catalyst while the reaction takes place, limit their use at this current stage.[12] Therefore effort are devoted to find new nanoparticles and ionic liquids systems different from conventional ionic liquids which tend to etch carbon supports rendering their use limited to proof of concept. This is presumably due to the fact that ILs are entirely made of ions and tends to form supramolecular structure as explained in section 1.3.1. On the other hand, nanotubes are highly conductive materials made of graphene sheets wrapped to form carbon cylinders.[9,64] Hence, the interaction nanotubes and ILs can be imagined as strongest as enough to maximise the electrostatic and van der waals interactions and destroy the carbon surfaces. In recent years, graphitised nanofibers have been used as a support to anchor nanoparticles and molecules at their step edges to form the state of art nanoreactor. Initially naked particles have been used for electrochemical and chemical reactions. However, these nanoparticles face many issues when used as a part of a nanoreactor. The lack of capping agent does not allow the perfect match of the host-guest interaction with the step edges of the carbon fibre as the area of surface contact is minimal, Figure 1.7 (c) and (d). This diminishes the confinement effect as the particles are bigger than 8 c (NP 2) 3.3 nm and are not anchored at the step edges (NP 2), Figure 1.8 b. [65]

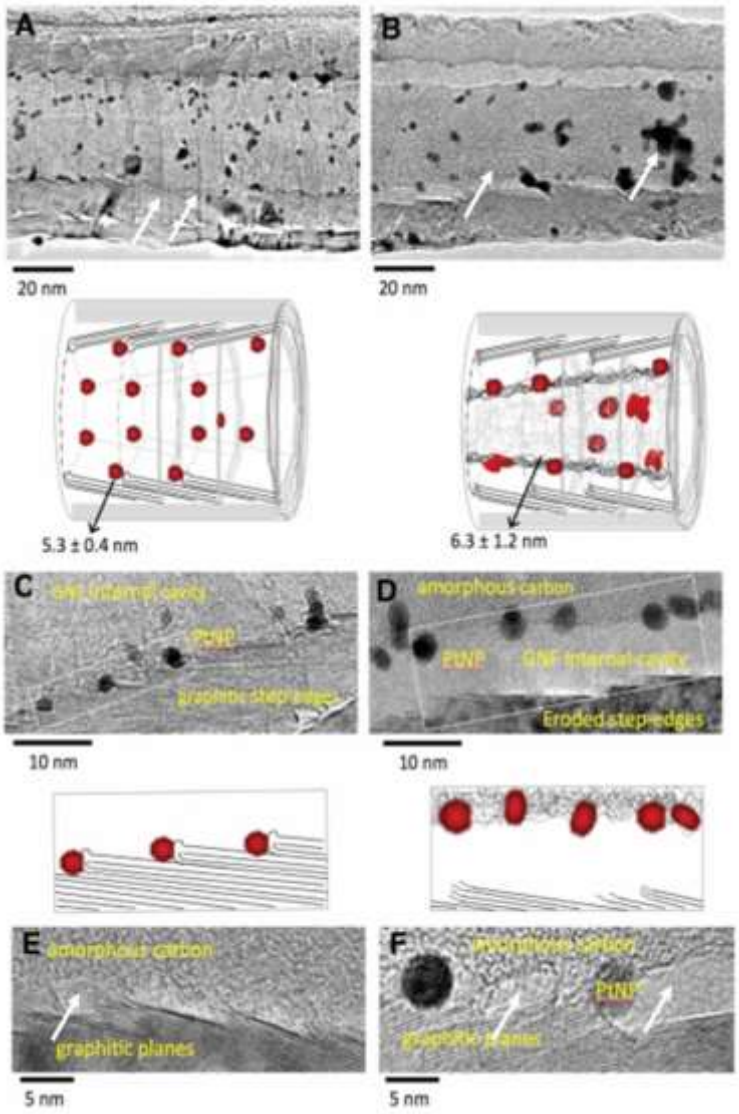


Figure 1.7 HRTEM images of PtNP@S-GNF before oxygen reduction reaction A) with some PtNP positioned at the graphitic step-edges and C) the internal cavity of GNF com-pletely free of NP (step-edges running across the GNF are clearly visible as transverse lines in the image). After exposure of PtNP@S-GNF to 50 000 potential cycles in the oxygen reduction reaction (ORR), B) internal cavity of GNF becomes filled with amorphous carbon located in the middle of the GNF, the white arrows shows the growth of th particles presumably due to coalescence. D) with all PtNP adhered to the amorphous carbon. Graphitic step-edges appear to be "unravelling" during the ORR giving rise to amorphous carbon, as clearly indicated by E) individual graphitic layers of GNF observed half-way

through amorphization. PtNP after 50 000 potential cycles remain inside GNF D) adhered to amorphous carbon or F) sandwiched between the amorphous carbon and GNF wall. In either case, It is claimed that a 5–10 nm gap formed between the inner wall of GNF and the layer of amorphous carbon allowing efficient access of reactants to catalytic centres PtNP during ORR. The white arrows show the etching on the step edge.[10]

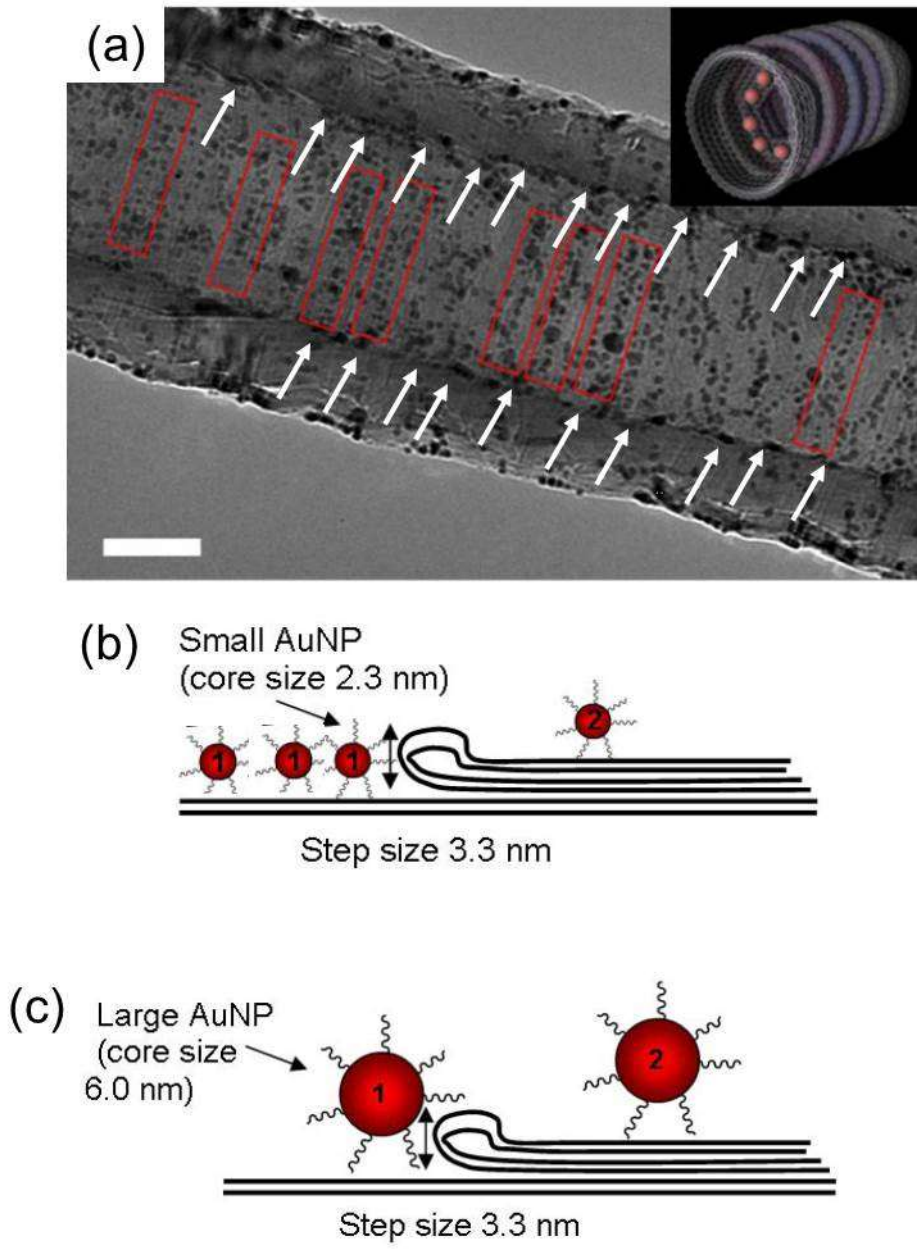


Figure 1.8 a) Bright-field TEM images and schematic diagrams illustrating the AuNPs adsorbed on the GNF outer surface (dark red) and anchored at

the graphitic step-edges within the GNF (light red) taken; (b) and (c) schematic representation of the interaction of the nanoparticles with the graphitic step edges (white arrows), showing the different interaction between NPs with comparable size and very different size.[66]

A and (a) of Figure 1.7 and 1.8 shows the lack of the nanoparticles at the step edges for the uncapped particles. The uncapped particles present diameter of 5.3 nm are bigger than the step edge of 3.3 nm. In this scenario the host guest interaction is not ideal compared to (b) Figure 1.7. The naked nanoparticles undergo carbonization while an external stimulus is applies as an electrical or the effect of the e-beam.[67] The applied voltage transform the graphitized interiors (nanocones) into amorphous carbon, Figure 1.7 (B), the interiors presents very different structural and electronic properties: *i.e*. short-range order, localized π electrons (a mixture of sp^2 and sp^3 hybridized carbon atoms) and a higher concentration of dangling bonds, as compared with graphitised cones.[10,68,69] Consequently, the charge transfer from amorphous carbon to the NP will be much lower than the graphene layer in nanocones.[70] This diminishes the stabilisation of the particles, as they are free to move to undergo coalescence to form aggregates shown in Figure 1.7 (B) indicated by the white arrows. The naked nanoparticles tend to be corroded (aged) when exposed to air which hinders their potential use as a nanoreactor. When an electrical potential or purely heat are applied to the nanoreactors/nanocomposite, the naked particle or oxidised particle reacts with the carbon support allowing the erosion of it via carbonization, Figure 1.7 A and Figure 1.9 (b-c).[67] G. Melinte *et al.* have shown in real time inside the column of a transmission electron microscope that naked and oxide particles tend to deteriorate the carbon support via the carbonization process which provokes the loss of the catalyst and the deterioration of the support as shown in Figure 1.9 (b), (c) and (d). The presence of them in the reaction mixture and final product limits the use of this carbon-metal nanostructure in electro catalysis to solely proof of concept**.** The life cycle assessment is poor as the nanoreactor cannot be used for a large scale production.[10] These problems can be tackled by anchoring capped nanoparticles at the step edges of nanofibers.[65] When a NP is positioned on the flat part of a GNF, Figure 1.8,

NP 2, the area of surface contact is minimal, but if the NP is residing at a step-edge, Figure 1.8 (b) NP 1, the surface of interaction increases significantly. Critically, if the size of the NP is commensurate with the size of the step-edge, the contact between the two surfaces is maximum, leading to a significant contribution of van der Waals forces and electrostatic interactions. The charge transfer between the nanocone graphene stacks and the adsorbed NP leads to highly ordered and stable composite superstructure and prevents the particles migration and coalescence. The synergetic interaction (confinement effect) between host and guest enhances the catalytic and electrochemical properties of the new nanoreactor.[65]

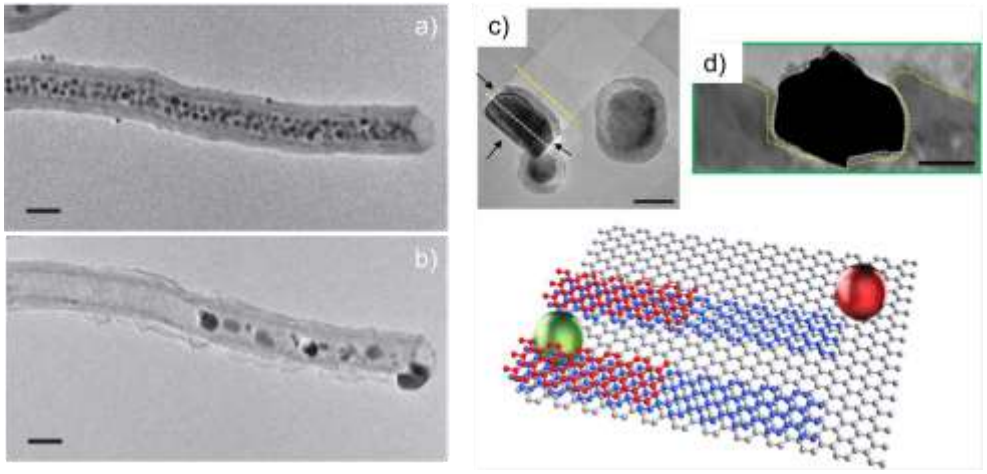


Figure 1.9 (a) $Fe_{3-x}O_4$ NPs-filled CNT (Carbon nanotubes) (prior the application of a voltage to the composite) and (b) metallic Fe/Fe_xC_y NPs-filled CNT (Carbon nanotubes) (post the application of a voltage to the composite); (c) and (d) The relationship between the active NP and the corresponding trench created when the composite was heated. (c) TEM projection of a trench and the corresponding digging NP (scale bar, 20nm). The external oxide layer is consumed (black arrowed) post the application of heat in airless condition. (d) Superposition of the XZ slices of the NP and the trench (yellow line) showing the close relationship between the 3D shape of the NP and the trench profile created. Scale bars are 50 nm (a) (b), 10nm (c) (d).[67,71]

1.5.1 Catalytic activity of metal nanoparticles inserted into composite material

The strategies most commonly followed for the synthesis of new drugs include the use of complex transition metal ligand which present all the problem well-presented above in this chapter such as losses of the catalyst poisoning of the product. [72] The utilisation of complex ligand synthesis is often due to the difficulty to control a synthetic reaction pathway to obtain the desired product.[73] Hence, one of the major challenge of synthetic chemistry is to realise selective catalysis, the second one is to meet the outstanding challenges of recyclability, selectivity and reusability. One of the solution in order to obtain selective catalysis is the use of carbon material to confine the substrates. Porous carbon material are widely used in electrochemistry mainly due to their wide electrochemical potential window, large surface area, chemical inertness and a well-defined topology.[74,75] Carbon nanostructures such as single walled nanotubes, hollow graphitised nanofibers can be functionalised with small molecule offering a confined environment for guests molecules facilitating reaction pathways performed inside the internal cavities.[76] The spatial confinement imposed by the nanoscale channels allows the formation of unique products even inaccessible by conventional synthetic methods, and can also direct well-known organic and inorganic reactions to modify their selectivity as compared to the bulk phase.[77] An interesting example reports the selective bromination of N-phenylacetamide which is highly selective for the para- substituted product when the reaction is performed in the presence of single walled nanotubes reaching 97%. The addition of bromide can occurs para, along the linear length, due to the narrow cavity of the nanotube, which could not be possible in the case of the orto-brominated product. [78] Also the influence of the confinement affect the selectivity of a reaction shown for the Heck coupling reaction catalysed by Pd(II)Salen either in combination or in absence of GNF.[76] The E-/Z-isomer distribution in Heck coupling reactions is directed by the insertion of the palladium salen catalyst into GNF.[79] Moreover, the supported catalyst influences catalytic activity and recyclability. More interestingly, the carbon surface can be considered as a cage which act as an electrode in which the substrates go inside react and after the reaction they leave the narrow

cavity of the nanotubes. [80] In a recent study, it has been compared an electrochemically active organometallic complex inside a hosting nanocarbon, a SWNT, and in bulk solution. In bulk solution the complex proceeds through an electrochemical oxidation, followed by the reaction with the nucleophilic solvent and ended with the electrochemical reduction of the newly formed complex whereas the supported catalyst undergoes only a simple oxidation and reduction. The result is incredibly different in both scenario probing of the mechanisms of interactions between redox active guest molecules and carbon nanotubes due primarily to steric confinement.[80] All these recent examples show the great potential can be made in synthetic chemistry only using carbon based composite material which act as a "pocket" which direct the selectivity, recyclability and catalytic activity. A great example chemical transformation in limited special confinement as controlled reaction pathways which seems work exactly as an enzymatic reaction in biological systems where the little "pocket" of the catalytic centre leads to well determined product in every catalytic cycles.[79]

1.6 X-Ray Photoemission Spectroscopy of Ionic Liquids

XPS (X-Ray Photoemission Spectroscopy) investigates the surface of samples and allows both chemical and elemental composition. The technique has been used to study the interaction between cation and anion and between ILs and solute dissolved in them.[81] XPS is based on the photoelectric effect and more technical details are discussed in section 2.6. The technique is surface sensitive, around 9 nm, and requires chamber pressures in the range between 10^{-8} to 10^{-10} mbar. The detection limit to the surface is due to inelastic mean free path. X-rays of the typical order of magnitude for an XPS experiment is 1 keV able to penetrate 1000 nm or more into the sample while electrons, which need to reach the detector in order to be collected, have enough energy to escape from the sample only when are ejected from the first 9 nm of matter.[82] The main reason ILs are investigated with XPS is due to their negligible vapour pressure. They are sterically hindered organic salts ILs have been studied especially for electrochemical applications. XPS is a promising technique to explore physical and chemical behaviour of ILs. They are very stable either during the initial pump-down or during exposure to the X-ray source: the samples

do not generally present evidences of either outgassing or beam damage.[83] ILs emit a good photoelectron flux, hence, short collection time is required to obtain exceptional XPS data. XPS can be used to determine the physical and chemical behaviour of bis(benzimidazolin-2-ylidene) salts determining high quality data. It is possible to show the high purity of the samples with identification of all elements (with the exception of H and He) present at concentrations >0.1 of the atomic percentage.[82] The type of information detected with XPS are the elemental composition and the electronic structure of the elements in solid and liquid samples with negligible vapour pressure suitable for the rigid condition necessary for an XPS experiments. Hence, the sample do not need to be solubilised in solvent but can be captured “naked”.[84]

Binding energy are collected with an XPS experiment to obtain both elemental and chemical information. Previous studies report reliable fitting methods for the characterisation of ILs system focussed upon the most diffuse imidazolium-based ionic liquids.[85] Further studies detailed the deconstruction peak of the C 1s photoemission peak for pyridinium-based and pyrrolidinium-based ionic liquids allowing the collection of reliable binding energies.[86] The deconstruction of the C 1s photoemission peak of the IL, which was based upon chemical knowledge and parameter constraints such as areas, FWHMs (Full width at High Maxima). Reproducible and accurate binding energies collected in complex systems are the basement for more complex structures able to understanding how molecule interact and are allocate.[87]

1.7 Aims and objective of this thesis

As outlined in this chapter nanoparticles stabilised by ionic liquids is a very hot topic especially in catalysis. The central aim of this work is to fabricate metal nanoparticles stabilised by NHCs. NHCs are a very exceptional type of ionic liquids for their traditional application in catalysis.[88] In general, ILs can be designed for many application to be environmentally friendly, with endless potential benefits for sustainable chemistry.[89] Bis(benzimidazolin-2-ylidene)pyridine skeleton can be derived from natural products and can function as a basis for ionic liquids.[59] XPS, as outlined in this chapter, generates a complete understanding of both the electronic environment of ionic liquids and the behaviour of ionic liquids as independent structures and as inserted into a supramolecular path. This information generates an understanding of ionic liquid structure and allows the developments of their applications correlated with their properties. The objective of this ongoing study is to determine interaction between the metal core of the nanoparticles and their stabiliser. This thesis evolves through the comparison of a new type of metal nanoparticles stabilised with NHCs and nanoparticles stabilised with TOP. As highlighted in this chapter, the properties of the nanoparticles depend upon the electronic environment of the metallic centre which has been supported in GNF to create a state of the art nanoreactor. The catalytic activity of the nanoreactors have been tested for the electrochemical oxidation of propargyl alcohol. To understand how the property of the capping agent are correlated to the reaction performance as selectivity and activity and how all these challenge are addressed in this thesis a logical pathways has been followed. Chapter 2 describes the synthesis used in this work. Also chapter 2 elucidated all the principles based on all the main characterisation methods used in this thesis: XPS and TEM are used to generate a complete understanding of the science behind the set of data. Chapter 3 explains the synthesis of N-Heterocyclic Carbene and how the TGA analysis is of crucial importance for the synthesis of NiNPs described later to understanding how the thermal stability is crucial to plan the experimental methods. Chapter 3 also aims to describe the XPS data in order to outline the study of the electronic distribution of the ionic compounds. A detailed understanding of the correlation between the symmetrical structures and the description of the C

1s photoemission region is described. Chapter 4 shows the utilisation of the NHCs and TOP to stabilise NPs and describes the characterisation of these unique types of NPs. The NiNPs have been supported to show the importance of confinement in GNF. In particular the catalytic application of Ni-NPs capped nanoparticles is illustrated to give an example of the great potential of these materials.

1.8 Bibliography

1 D. J. Barber and I. C. Freestone, *Archaeometry*, 1990, **1**, 33–45.

2 D. L. Schodek, P. Ferreira and M. F. Ashby, *Nanomaterials, Nanotechnologies and Design: An Introduction for Engineers and Architects*, Elsevier, Oxford, 2009.

3 M. Reibold, P. Paufler, A. A. Levin, W. Kochmann, N. Pätzke and D. C. Meyer, *Nature*, 2006, **444**, 286–286.

4 J. Pérez-Arantegui, J. Molera, A. Larrea, T. Pradell and M. Vendrell-Saz, *J. Amrican Ceram. Soc.*, 2001, **84**, 442–446.

5 V. H. Grassian, *J. Phys. Chem. C*, 2008, **112**, 18303–18313.

6 A. I. Frenkel, C. W. Hills and R. G. Nuzzo, *J. Phys. Chem. B*, 2001, **105**, 12689–12703.

7 C. Vollmer and C. Janiak, *Coord. Chem. Rev.*, 2011, **255**, 2039–2057.

8 J. A. Rodríguez-Manzo, C. Pham-Huu and F. Banhart, *ACS Nano*, 2011, **5**, 1529–1534.

9 A. La Torre, F. Ben Romdhane, W. Baaziz, I. Janowska, C. Pham-Huu, S. Begin-Colin, G. Pourroy and F. Banhart, *Carbon N. Y.*, 2014, **77**, 906–911.

10 M. del Carmen Gimenez-Lopez, A. Kurtoglu, D. A. Walsh and A. N. Khlobystov, *Adv. Mater.*, 2016, **28**, 9103–9108.

11 A. La Torre, PhD Theis, University of Nottingham, 2013.

12 J. Dupont and L. Kollár, *Ionic Liquids (ILs) in Organometallic Catalysis*, Berlin, Heidelberg, Springer, 2015.

13 M. Freemantle, *An Introduction to Ionic Liquids*, Wiley-VCH., 2010.

14 M. Deetlefs and K. R. Seddon, *Green Chem.*, 2010, **12**, 17.

15 T. Wasserscheid, Peter and Welton, *Ionic Liquids in Synthesis*, 2008.

16 J. G. Huddleston, A. E. Visser, W. M. Reichert, H. D. Willauer, G. a. Broker and R. D. Rogers, *Green Chem.*, 2001, **3**, 156–164.

17 M. J. Earle, J. M. S. S. Esperança, M. a Gilea, J. N. C. Lopes, L. P. N. Rebelo, J. W. Magee, K. R. Seddon and J. a Widegren, *Nature*, 2006, **439**, 831–834.

18 J. D. Holbrey, W. M. Reichert, R. P. Swatloski, G. a. Broker, W. R. Pitner, K. R. Seddon and R. D. Rogers, *Green Chem.*, 2002, **4**, 407–413.

19 J. D. Scholten, B. C. Leal and J. Dupont, *ACS Catal.*, 2012, **2**, 184–200.

20 F. Kohler, S. Popp, H. Klefer, I. Eckle, C. Schrage, B. Bohringer, M. Haumann and P. Wasserscheid, *Green Chem.*, 2014, **16**, 3560.

21 N. V Plechkova and K. R. Seddon, *Chem. Soc. Rev.*, 2008, **37**, 123–150.

22 R. M. Deshpande, A. A. Kelkar, A. Sharma, C. Julcour-Lebigue and H. Delmas, *Chem. Eng. Sci.*, 2011, **66**, 1631–1639.

23 P. Sledź, M. Mauduit and K. Grela, *Chem. Soc. Rev.*, 2008, **37**, 2433–2442.

24 R. Franke, D. Selent and A. Börner, *Chem. Rev.*, 2012, **112**, 5675–5732.

25 U. Christmann and R. Vilar, *Angew. Chemie - Int. Ed.*, 2005, **44**, 366–374.

26 T. E. Kunene, P. B. Webb and D. J. Cole-Hamilton, *Green Chem.*, 2011, **13**, 1476–1481.

27 T. Selvam, A. Machoke and W. Schwieger, *Appl. Catal. A Gen.*, 2012, **445**–**446**, 92–101.

28 C. C. Cassol, A. P. Umpierre, G. Machado, S. I. Wolke and J. Dupont, *J. Am. Chem. Soc.*, 2005, **127**, 3298–3299.

29 M. I. Burguete, E. García-Verdugo, I. Garcia-Villar, F. Gelat, P. Licence, S. V. Luis and V. Sans, *J. Catal.*, 2010, **269**, 150–160.

30 M. Lancaster, *Green Chemistry: An Introductory Text*, RSC Publis., 2010.

31 R. F. Frade and C. A. Afonso, *Hum. Exp. Toxicol.*, 2010, **29**, 1038–54.

32 B. Jastorff, R. Störmann, J. Ranke, K. Mölter, F. Stock, B. Oberheitmann, W. Hoffmann, J. Hoffmann, M. Nüchter, B. Ondruschka and J. Filser, *Green Chem.*, 2003, **5**, 136–142.

33 P. T. Anastas and M. M. Kirchhoff, 2002, **35**, 686–694.

34 S. Y. Tang, R. a. Bourne, R. L. Smith and M. Poliakoff, *Green Chem.*, 2008, **10**, 268.

35 C. Janiak, *Zeitschrift fur Naturforsch. - Sect. B J. Chem. Sci.*, 2013, **68**, 1059–1089.

36 J. Krämer, E. Redel, R. Thomann and C. Janiak, *Organometallics*,

2008, **27**, 1976–1978.

37 J. Dupont and M. R. Meneghetti, *Curr. Opin. Colloid Interface Sci.*, 2010, **39**, 1780–1804.

38 J. Dupont, *J. Braz. Chem. Soc.*, 2004, **15**, 341–350.

39 C. S. Consorti, P. A. Z. Suarez, R. F. De Souza, R. A. Burrow, D. H. Farrar, A. J. Lough, W. Loh, L. H. M. Da Suva and J. Dupont, *J. Phys. Chem. B*, 2005, **109**, 4341–4349.

40 D. Astruc, F. Lu and J. R. Aranzaes, *Angew. Chemie - Int. Ed.*, 2005, **44**, 7852–7872.

41 A. P. Abbott, R. C. Harris and K. S. Ryder, *J. Phys. Chem. B*, 2007, **111**, 4910–4913.

42 A. P. Abbott, *ChemPhysChem*, 2004, **5**, 1242–1246.

43 D. R. MacFarlane, M. Forsyth, E. I. Izgorodina, A. P. Abbott, G. Annat and K. Fraser, *Phys. Chem. Chem. Phys.*, 2009, **11**, 4962–4967.

44 H. Bönnemann and R. M. Richards, *Eur. J. Inorg. Chem.*, 2001, **2001**, 2455–2480.

45 C. Pan, K. Pelzer, K. Philippot, B. Chaudret, F. Dassenoy, P. Lecante and M. J. Casanove, *J. Am. Chem. Soc.*, 2001, **123**, 7584–7593.

46 H. Olivier-Bourbigou, L. Magna and D. Morvan, *Appl. Catal. A Gen.*, 2010, **373**, 1–56.

47 R. Fehrmann, A. Riisager and M. Haumann, *Supported Ionic Liquids: Fundamentals and Applications*, 2014.

48 A. Riisager, R. Fehrmann, M. Haumann and P. Wasserscheid, *Top. Catal.*, 2006, **40**, 91–102.

49 O. Kuhl, *Functionalised N-Heterocyclic Carbene Complexes*, 2010.

50 D. Pugh and A. a. Danopoulos, *Coord. Chem. Rev.*, 2007, **251**, 610–641.

51 T. Weskamp, V. P. W. Bohm and W. A. Herrmann, *J. Organomet. Chem.*, 2000, **600**, 12–22.

52 D. J. Nielsen, K. J. Cavell, B. W. Skelton and A. H. White, *Inorganica Chim. Acta*, 2002, **327**, 116–125.

53 E. Peris and R. H. Crabtree, *Coord. Chem. Rev.*, 2004, **248**, 2239–2246.

54 C. M. Crudden and D. P. Allen, *Coord. Chem. Rev.*, 2004, **248**, 2247–2273.

55 T. Vander Hoogerstraete, N. R. Brooks, B. Norberg, J. Wouters, K. Van Hecke, L. Van Meervelt and K. Binnemans, *CrystEngComm*, 2012, **14**, 4902–4911.

56 I. J. B. Lin and C. S. Vasam, *J. Organomet. Chem.*, 2005, **690**, 3498–3512.

57 L. Casal-Dujat, M. Rodrigues, A. Yagüe, A. C. Calpena, D. B. Amabilino, J. Gonzaílez-Linares, M. Borraís and L. Peírez-Garciía, *Langmuir*, 2012, **28**, 2368–2381.

58 T. Tu, W. Assenmacher, H. Peterlik, R. Weisbarth, M. Nieger and K. H. Dötz, *Angew. Chemie Int. Ed.*, 2007, **46**, 6368–6371.

59 T. Tu, W. Assenmacher, H. Peterlik, G. Schnakenburg and K. H. Dötz, *Angew. Chemie - Int. Ed.*, 2008, **47**, 7127–7131.

60 T. Tu, H. Mao, C. Herbert, M. Xu and K. H. Dötz, *Chem. Commun.*, 2010, **46**, 7796–7798.

61 T. Tu, W. Assenmacher, H. Peterlik, G. Schnakenburg and K. H. Dötz, 2008.

62 H. Ba, Y. Liu, L. Truong-Phuoc, C. Duong-Viet, X. Mu, W. H. Doh, T. Tran-Thanh, W. Baaziz, L. Nguyen-Dinh, J.-M. Nhut, I. Janowska, D. Begin, S. Zafeiratos, P. Granger, G. Tuci, G. Giambastiani, F. Banhart, M. J. Ledoux and C. Pham-Huu, *Chem. Commun.*, 2015, **51**, 14393–14396.

63 H. Ba, Y. Liu, L. Truong-Phuoc, C. Duong-Viet, J. M. Nhut, D. L. Nguyen, O. Ersen, G. Tuci, G. Giambastiani and C. Pham-Huu, *ACS Catal.*, 2016, **6**, 1408–1419.

64 V. N. Popov, *Mater. Sci. Eng. R*, 2004, **43**, 61–102.

65 A. La Torre, M. del Carmen Gimé nez-Ló pez, M. W. Fay, G. A. Rance, W. A. Solomonsz, T. W. Chamberlain, P. D. Brown and A. N. Khlobystov, *ACS Nano*, 2012, **6**, 2000–2007.

66 A. La Torre, M. W. Fay, G. A. Rance, M. Del Carmen Gimenez-Lopez, W. A. Solomonsz, P. D. Brown and A. N. Khlobystov, *Small*, 2012, **8**, 1222–1228.

67 G. Melinte, I. Florea, S. Moldovan, I. Janowska, W. Baaziz, R. Arenal, A. Wisnet, C. Scheu, S. Begin-Colin, D. Begin, C. Pham-Huu

and O. Ersen, *Nat Commun*, 2014, **5**, 1–9.

68 S. S. Datta, D. R. Strachan, E. J. Mele and C. A. T. Johnson, 2009, **9**, 7–11.

69 T. Ohta, A. Bostwick, T. Seyler, K. Horn and E. Rotenberg, *Science (80-.).*, 2006, **313**, 951–954.

70 Z. Luo, L. A. Somers, Y. Dan, T. Ly, N. J. Kybert, E. J. Mele and A. T. C. Johnson, *Nano Lett.*, 2010, **10**, 777–781.

71 G. Melinte, S. Moldovan, C. Hirlimann, X. Liu, S. Bégin-Colin, D. Bégin, F. Banhart, C. Pham-Huu and O. Ersen, *Nat. Commun.*, 2015, **6**, 1–7.

72 B. M. Trost and D. L. Van Vranken, *Chem. Rev.*, 1996, **96**, 395–422.

73 M. P. Carroll and P. J. Guiry, *Chem. Soc. Rev.*, 2014, **43**, 819–833.

74 I. Dumitrescu, J. P. Edgeworth, P. R. Unwin and J. V. Macpherson, *Adv. Mater.*, 2009, **21**, 3105–3109.

75 Y. Shao, G. Yin, J. Zhang and Y. Gao, *Electrochim. Acta*, 2006, **51**, 5853–5857.

76 M. A. Lebedeva, T. W. Chamberlain, A. Thomas, B. E. Thomas, C. T. Stoppiello, E. Volkova, M. Suyetin and A. N. Khlobystov, *Nanoscale*, 2016, **8**, 11727–11737.

77 D. A. Britz, A. N. Khlobystov, K. Porfyrakis, A. Ardavan and G. A. D. Briggs, *Chem. Commun.*, 2005, 37–39.

78 S. a Miners, G. a Rance and A. N. Khlobystov, *Chem. Commun.*, 2013, **49**, 5586–5588.

79 M. A. Lebedeva, T. W. Chamberlain, A. Thomas, B. E. Thomas, C. T. Stoppiello, E. Volkova, M. Suyetin, A. N. Khlobystov, K. Kamarás, L. De Cola, A. N. Khlobystov, D. Bonifazi and K. Kaneko, *Nanoscale*, 2016, **8**, 11727–11737.

80 R. L. McSweeney, T. W. Chamberlain, M. Baldoni, M. A. Lebedeva, E. S. Davies, E. Besley and A. N. Khlobystov, *Chem. - A Eur. J.*, 2016, **22**, 13540–13549.

81 I. J. Villar-Garcia, E. F. Smith, A. W. Taylor, F. Qiu, K. R. J. Lovelock, R. G. Jones and P. Licence, *Phys. Chem. Chem. Phys.*, 2011, **13**, 2797–2808.

82 J. C. Vickerman and I. S. Gilmore, *Surface Analysis The Principal Techniques*, John Wiley & Sons Ltd., Chichester, 2009.

83 E. F. Smith, F. J. M. Rutten, I. J. Villar-Garcia, D. Briggs and P. Licence, *Langmuir*, 2006, **22**, 9386–9392.

84 E. F. Smith, I. J. Villar Garcia, D. Briggs and P. Licence, *Chem. Commun.*, 2005, 5633.

85 I. J. Villar-Garcia, E. F. Smith, A. W. Taylor, F. Qiu, K. R. J. Lovelock, R. G. Jones and P. Licence, *Phys. Chem. Chem. Phys. Phys. Chem. Chem. Phys*, 2011, **13**, 2797–2808.

86 S. Men, D. S. Mitchell, K. R. J. Lovelock and P. Licence, *ChemPhysChem*, 2015, **16**, 2211–2218.

87 S. Men, K. R. J. Lovelock and P. Licence, *Phys. Chem. Chem. Phys.*, 2011, **13**, 15244–15255.

88 S. Lee and S. Lee, *Chem. Commun.*, 2006, 1049–1063.

89 A. R. Santos, R. K. Blundell and P. Licence, *Phys. Chem. Chem. Phys.*, 2015, **17**, 11839–11847.

Chapter 2

Experimental Methodology

2.1 Introduction

In this section, it is presented the synthesis and characterisation of the N-Heterocyclic carbene used to stabilise the new type of nickel nanoparticles prepared in this project.

The first section concern the synthesis of the N-Heterocyclic carbene compounds. The second section covers the synthesis of nickel nanoparticles. The third section introduces the encapsulation of nanoparticles into hollow carbon nanostructures. The fourth section presents the complementary surface, structural, thermal and electrochemical characterisation techniques used to appraise the functional and structural properties of the fabricated nanostructures.

2.2 Materials and Instrumentation

Reagents and solvents were obtained from commercial suppliers and used as received. Nickel acetate tetra hydrate has been previously dehydrated in vacuum ($8 \cdot 10^{-2}$ mbar) for 72 h at 50°C. Unless otherwise stated all metathesis reactions were performed using ultra-pure water (18.2 Ω Millipore) under air in an open flask. All the other reactions were carried out under an inert atmosphere of dry argon with standard Schlenk tube techniques, further details are presented below.

^{1}H, ^{13}C, ^{31}P ^{11}B ^{19}F NMR were recorded with a Bruker AV (III) 500, Bruker AV 400, DPX 400, DPX 300 spectrometer at ambient temperature. NMR samples were prepared using DMSO, D_2O, $CDCl_3$ and CD_3OD. Mass spectra were recorded using a Bruker microTOF using ESI (+ve and -ve ion) electrospray ionisation source using methanol UHPLC (Ultra high performance liquid chromatography grade for sample preparation). Elemental Microanalysis were performed using a CE-440 Elemental Analyser was used to detect C H N compositions of 2,6-bis(benzimidazolium)pyridine salts, 2,6-bis(alkylimidazolium)pyridine salts and the nickel-pincer complex.

TEM images were recorded with a JEOL 2100F FEG-TEM operated at 200 kV. The EDX analysis was performed using Oxford Instruments 80mm X-Max system for energy dispersive x-ray spectroscopy analysis on a JEOL 2100F FEG-TEM operating at 200 kV. IR (Infrared) measurements were

recorded with a Bruker FTIR Spectroscopy with ATR (attenuated total reflectance) accessory.

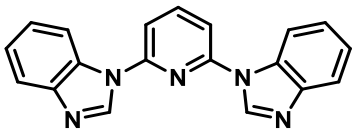
GNF materials used are PR19-GNFs supplied by Pyrograf Products Inc. The glassy carbon electrode was purchased from IJ Cambria and the reticulated vitreous carbon from Goodfellow. The water used in electrochemical experiments was ultra-pure water (18.2 Ω Millipore) and all other solvents and reagents were purchased from Sigma Aldrich. All electrochemical experiments were performed using an AUTOLAB PGSTAT302N potentiostat.

2.2.1 X-Ray photoemission spectroscopy: experimental record

All the spectra were recorded with a Kratos Axis Ultra spectrometer supplied with a focused monochromated Al Kα source (1486.6 eV), hybrid (magnetic/electrostatic) optics, concentric hemispherical analyser and a multi-channel plate and delay line detector (DLD). Wide survey scan and high resolution scan were recorded at pass energy of 80 eV and 20 eV respectively. The experimental error is set by the manufacturer and quoted as ± 0.1 eV. The samples, approximately 10 mg of solid, were placed on a double sided adhesive tape in order to prevent eventual losses. Samples were then introduced into the Ultra High Vacuum (UHV) by the aid of airlock with minimum exposure to air. The samples were pre-pumped in a preparative chamber overnight in order to eliminate volatile impurities to pressure of the order of 10^{-9} mbar before its transfer into the analytical XPS chamber. The photoemission electrons were acquired using monochromated Al Kα (1486.6 eV). The compounds investigated so far showed stability under X-Ray exposure. We investigated the ionic nature and their physical-chemical properties. Charge neutralisation was applied using a Kratos charge neutraliser consisting of a filament, coaxial with electrostatic and magnetic transfer lenses, and a balance plate which create a potential gradient between the neutraliser and the sample. Charge neutralisation was applied at 1.9 A filament current and 3.3 V balance plate voltage.

2.3 Synthesis of Pyridine-Bridged Benzimidazolium salts

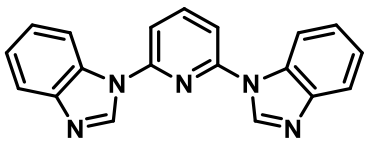
2.3.3 2,6-Bis(benzimidazole)pyridine, $(BzIm)_2Py$ from 2,6-dibromopyridine



Benzimidazole (28.9 g, 0.244 mol) was dissolved in dry DMF (100 cm^2) and sodium hydride (60% in mineral oil, 10.1 g, 0.253 mol, 3 eq.) was carefully added under an inert atmosphere.[1] After 1 h stirring, 2,6-dibromopyridine (20 g, 0.0844 mol) was added and the resulting mixture was heated to 60 °C for 16 h, then at 120 °C for 24 h and finally at 140 °C for 24 h. After cooling the solution was poured into water (300 cm^2) and left to stir for 1 h. The precipitate was filtered and recrystallized from $CHCl_3/Et_2O$ to give a white solid which was dried at 50 ºC *in vacuum ($8 \cdot 10^{-2}$ mbar)* for 24 h (16.89 g, 65 %).

^{1}H NMR (400 MHz, DMSO-d_6): δ = 9.11 (s, 2H), 8.37 (t, J = 8.1 Hz, 1H), 8.29 – 8.22 (m, 2H), 7.99 (d, J = 8.1 Hz, 2H), 7.87 – 7.79 (m, 2H), 7.43 – 7.35 (m, 4H).^{13}C NMR (101 MHz, DMSO-d_6): δ = 206.31, 149.18, 145.32, 142.95, 131.68, 124.57, 123.72, 120.50, 114.01, 112.75. $[M+H]^+$. ESI-MS (+ve) m/z 312.12 $[M^+]$. Elemental analysis (%): Anal. Calcd for $C_{19}H_{13}N_5$: C, 73.30; H, 4.21; N, 22.49; Found: C, 73.52; H, 4.08; N, 22.24.

2.3.4 2,6-Bis(benzimidazole)pyridine, $(BzIm)_2Py$ from 2,6-dichloropyridine

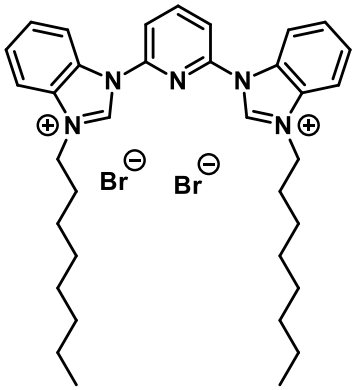


Benzimidazole (28.9 g, 0.244 mol) was dissolved in dry DMF (100 cm^2) and added dropwise to sodium hydride (60% in mineral oil, 10.1 g, 0.253 mol, 3 eq.) under an inert atmosphere. After 1 h 2,6-dichloropyridine (12.49 g, 0.844 mol) was added and the resulting mixture was heated to 60 °C for 16 h, at 120 °C for 24 h and finally at 140 °C for 24 h. After cooling the solution was poured into water (300 cm^2) and left to stir for 1 h. The precipitate was

filtered as brownish-pinkish solid of recrystallized from $CHCl_3/Et_2O$.The solid was solubilised in $CHCl_3$, the solid floating was filtered out. The precipitate was extracted with Et_2O. The addition diethyl ether allows the precipitation of a white bright solid which was dried at 50 ºC *in vacuum ($8 \cdot 10^{-2}$ mbar)* mbar for 16 h (16.34 g, 63 %).

^{1}H NMR (400 MHz, DMSO-d_6) δ 9.09 (s, 2H), 8.35 (t, *J* = 8.0 Hz, 1H), 8.27 – 8.21 (m, 2H), 7.97 (d, *J* = 8.0 Hz, 2H), 7.86 – 7.79 (m, 2H), 7.43 – 7.33 (m, 4H); ^{13}C NMR (101 MHz, DMSO-d_6) δ: 206.67, 148.97, 144.50, 142.74, 131.92, 124.38, 123.54, 120.30, 113.82, 112.53. ESI-MS (+ve) m/z 312.12 [M+]. Elemental analysis (%): Anal. Calcd for $C_{19}H_{13}N_5$: C, 73.30; H, 4.21; N, 22.49; Found: C, 73.23; H, 3.99; N, 22.20.

2.3.5 2,6-bis(octylbenzimidazolium) pyridine dibromide, $[(C_8BzIm)_2Py]Br_2$

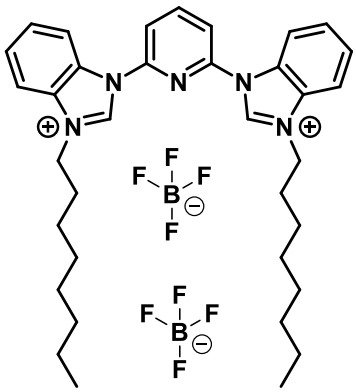


1-octane (20 eq, 0.141 mol, 27.079 g, 24.22 cm^2) was added dropwise under an inert atmosphere to 2,6-bis(benzimidazolium)pyridine (1 eq, 0.00705 mol, 2.19 g) and then heated at 130 ºC for 24, then at 160 ºC for 5 h. The mixture was left cooling down.[1] The precipitate was diluted with diethyl ether (50 cm^2) and the resulting precipitate collected and washed several times with the same solvent. The solid was recrystallised several times from methanol (≈10 cm^2) and diethyl ether (≈150 cm^2). The precipitate was finally filtered and dried at 50 ºC *in vacuum ($8 \cdot 10^{-2}$ mbar)* for 16 h (2.8 g, 94 %).

^{1}H NMR (400 MHz, DMSO-d_6): δ = 10.73 (s, 2H), 8.76 (t, *J* = 8.1 Hz, 1H), 8.46 (d, *J* = 8.5, 0.9 Hz, 2H), 8.35 (d, *J* = 8.1 Hz, 2H), 8.29 (d, J = 8.4, 0.9, 2H), 7.82 (t, *J* = 8.4, 7.3, 1.1 Hz, 2H), 7.74 (t, *J* = 8.4, 7.3, 1.1 Hz, 2H), 4.67 (t, *J* = 7.3 Hz, 4H), 2.08 – 1.97 (m, 4H), 1.53 – 1.20 (m, 20 H), 0.85 (t, 6H);

^{13}C NMR (101 MHz, DMSO-d_6): δ = 146.88,144.94,143.30, 132.09, 131.01, 128.38, 127.87, 118.40, 116.19, 114.78, 47.93, 31.67, 31.17, 28.99, 28.78, 26.29, 22.54, 14.42. ESI-MS (+ve) m/z 268.69 [M^{2+}]. Elemental analysis (%): Anal. Calcd for $C_{35}H_{47}Br_2N_5$: C, 60.26; H, 6.79; N, 10.04; Found: C, 59.96; H, 6.76; N, 9.75.

2.3.6 2,6-bis(Octylbenzimidazolium)$_2$pyridinetetrafluoroborate, [(C_8BzIm)$_2$Py][BF_4]$_2$

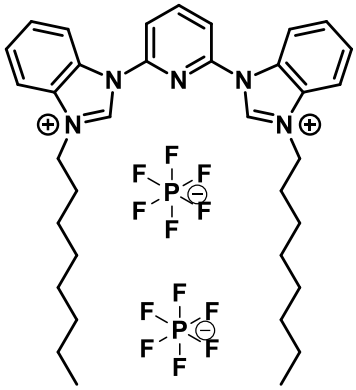


2,6-bis(octylbenzimidazolium) pyridine dibromide (1 eq, 0.0013 mol 0.7 g) was transferred to a round bottom flask and dissolved in 25 cm^2 of H_2O and 25 cm^2 of DCM. Tetrafluoroboric acid (50 % w/w, 4.8 eq, 0.0062 mol, 0.21 g, 2.03 cm^2) was then added dropwise. The formation of a precipitate was instantaneous. However, in order to assure the completion of the reaction the mixture was left stirring overnight. A white solid precipitate was obtained. The organic and the water phase were washed several times with ultrapure water. The product was separated and consequently dry *in vacuum (8·10^{-2} mbar)* overnight at 50 ºC to yield a white solid (0.68 g, 99 %).

^{1}H NMR (400 MHz, DMSO-d_6): δ = 10.62 (s, 2H), 8.76 (t, *J* = 8.1 Hz, 1H), 8.45 (d, J = 8.4 Hz, 2H), 8.30 (t, *J* = 8.4 Hz, 4H), 7.82 (t, J = 8.3, 7.3, 1.1 Hz, 2H), 7.74 (t, J = 8.4, 7.3, 1.1 Hz, 2H), 4.65 (t, *J* = 7.3 Hz, 4H), 2.15 – 1.97 (m, 4H), 1.59 – 1.14 (m, 20H), 0.86 (t, J = 7.3 Hz, 6H); ^{13}C NMR (101 MHz, DMSO-d_6): δ = 146.90, 144.95, 143.26, 132.08, 130.04, 128.39, 127.89, 118.40, 116.20, 114.77, 49.06, 47.95, 31.67, 28.99, 28.98, 26.28, 22.54, 14.42. ^{19}F NMR (376 MHz, DMSO-d_6) δ -148.30. ESI-MS (+ve) m/z

268.69 [M^{2+}]. Elemental analysis (%): Anal. Calcd for $C_{35}H_{47}B_2F_8N_5$: C, 59.09; H, 6.66; N, 9.84; Found: C, 59.39; H, 6.58; N, 9.81.

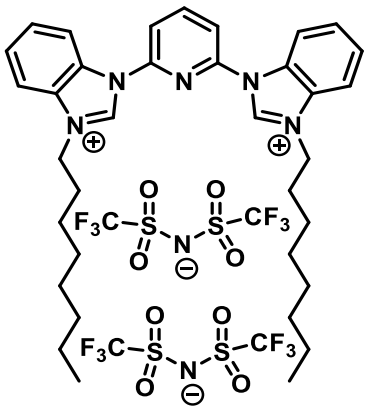
2.3.7 2,6-bis(Octylbenzimidazolium) pyridine bis(trifluoromethylsulfonyl)amide, $[(C_8BzIm)_2Py][PF_6]_2$



2,6-bis(octylbenzimidazolium) pyridine dibromide (1 eq, 0.0013 mol 0.7 g) was transferred to a round bottom flask and dissolved in 25 cm^2 of H_2O and 25 cm^2 of DCM. Hexafluorophosphoric acid solution (60 % w/w, 4.8 eq, 0.0062 mol, 0.91 cm^2) was then added dropwise (with extreme care). The formation of a precipitate was rapid. The mixture was left stirring for 12 h to assure the completion of the reaction. A white solid precipitate was obtained. The organic and the water phase were washed several times with ultrapure water. The product was separated and consequently dried *in vacuum* ($8 \cdot 10^{-2}$ mbar) overnight at 50 ºC to yield a white solid (0.69 g, 99 %).

^{1}H NMR (400 MHz, DMSO-d_6): δ = 10.62 (s, 2H), 8.76 (t, *J* = 8.1 Hz, 1H), 8.45 (d, *J* = 8.4 Hz, 2H), 8.30 (t, *J* = 8.3 Hz, 4H), 7.82 (t, J = 7.7 Hz, 2H), 7.74 (t, J 7.7 Hz, 2H), 4.66 (t, *J* = 7.4 Hz, 4H) , 2.07-1.99 (m, 4H), 2.07 – 1.99 (m, 2H), 1.56 – 1.17 (m, 20H), 0.85 (d, J = 6.3 Hz, 6H). ^{13}C NMR (101 MHz, DMSO-d_6) δ 146.42, 144.46, 142.78, 131.61, 129.56, 127.91, 127.41, 117.91, 115.73, 114.29, 47.47, 31.19, 30.69, 28.50, 28.52, 25.80, 22.06, 13.94; ^{19}F NMR (376 MHz, DMSO-d_6): δ = -60.12, -70.12, 31P NMR (162 MHz, DMSO-d_6): δ = -144.20 (m). ESI-MS (+ve) m/z 268.69 [M^{2+}]. Elemental analysis (%): Anal. Calcd for $C_{35}H_{47}F_{12}N_5\ P_2$: C, 50.79; H, 5.72; N, 8.46; Found: C, 51.00; H, 5.8; N, 8.28.

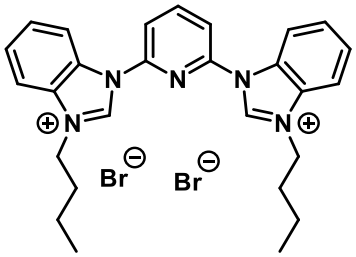
2.3.8 2,6-bis(octyllbenzimidazolium)pyridine bis(trifluoromethylsulfonyl)amide, $[(C_8BzIm)_2Py][NTf_2]_2$



2,6-bis(octylbenzimidazolium)pyridine dibromide (1 eq, 0.7 g, 0.0013 mol) was transferred to a round bottomed flask and dissolved in 20 cm^2 of ultrapure water and 10 cm^2 of DCM. Lithium bis(trifluoromethylsulfonyl)imide (4.8 eq, 79 g, 0.0062 mol) was dissolved in 20 cm^2 of ultrapure water and added to the reaction drop wise. The organic phase is pale yellow showing the formation of a product. The reaction mixture was washed with water (3 x 20 cm^2) in order to eliminate the excess of bis(trifluoromethylsulfonyl)imide . The product was recrystallised from acetonitrile and ethyl acetate. The organic phase was dry under reduced pressure with rotary evaporator. The product was dried *in vacuum ($8 \cdot 10^{-2}$ mbar)* overnight at 50 °C to yield a yellow viscous liquid (0.69 g, 98.5 %).

^{1}H NMR (400 MHz, DMSO-d_6) δ 10.62 (s, 2H), 8.76 (t, *J* = 8.1 Hz, 1H), 8.45 (d, *J* = 8.4, 0.9 Hz, 2H), 7.82 (t, *J* = 8.4, 7.3, 1.1 Hz, 2H), 7.74 (t, *J* = 8.4, 7.3, 1.1 Hz, 2H), 4.65 (t, *J* = 7.3 Hz, 4H), 2.09 – 1.98 (m, 4H), 1.51 – 1.20 (m, 19H), 0.86 (t, 6H); ^{13}C NMR (101 MHz, DMSO-d_6) δ 146.90, 144.93, 143.26, 132.08, 130.04, 128.37, 127.88, 121.53, 118.38, 116.20, 114.76, 47.95, 31.66, 31.15, 28.98, 28.97, 26.28, 22.53, 14.40. ESI-MS (+ve) m/z 268.69 [M^{2+}].

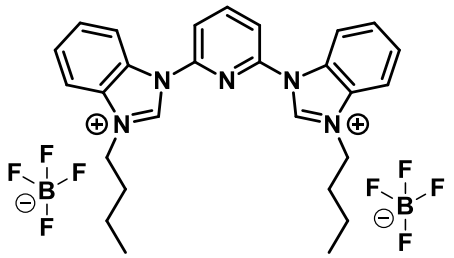
2.3.9 2,6-bis(butylbenzimidazolium)$_2$pyridine dibromide, [$(C_4BzIm)_2Py$]Br_2



1-bromobutane (20 eq) was added dropwise under an inert atmosphere to 2,6-bis(benzimidazolyl)pyridine (1eq) in DMF (10 cm^2) and then heated at 100 ºC for 48 h. The mixture was left cooling down.[1] The precipitate was diluted with diethyl ether (50 cm^2) and the resulting precipitate collected. The solid was then filtered and washed three times with diethyl ether. The product was recrystallise from DMSO and a mixture of ethyl acetate and diethyl ether (1:1) filtered and consequently dried in vacuum *(8·10^{-2} mbar)* overnight at 50 ºC to yield a white solid (2.97 g, 99 %).

^{1}H NMR (400 MHz, DMSO-d_6): δ = 10.88 (s, 2H), 8.77 (t, *J* = 8.1 Hz, 1H), 8.47 (d, 8.3 Hz, 2H), 8.39 (d, J=8.3 Hz, 2H), 8.30 (d, J = 8.3 Hz, 2H), 7.82 (t, J = 7.8 Hz, 2H), 7.74 (t, J=7.8 Hz, 2H), 4.71 (t, *J* = 7.3 Hz, 4H), 2.05 (p, *J* = 7.4 Hz, 4H), 1.48 (h, *J* = 7.4 Hz, 4H), 0.99 (t, *J* = 7.3 Hz, 6H). ^{13}C NMR (101 MHz, DMSO-d_6) δ: 146.38, 144.44, 131.63, 129.51, 127.89, 127.36, 117.92, 115.75, 114.31, 47.20, 30.50, 19.15, 13.48. ESI-MS (+ve) m/z 212.63 [M^{2+}]. Elemental analysis (%): Anal. Calcd for $C_{27}H_{31}Br_2N_5$: C, 55.40; H, 5.34; N, 11.96; Found: C, 55.10; H, 5.17; N, 11.79.

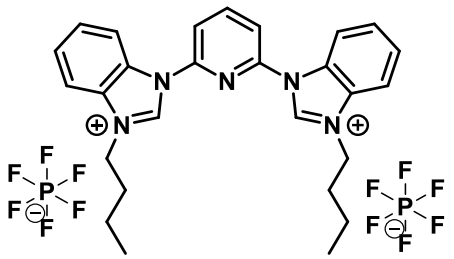
2.3.10 2,6-bis(butylbenzimidazolium)$_2$pyridine tetrafluoroborate, [(C$_4$BzIm)$_2$Py][BF$_4$]$_2$



2,6-bis(butylbenzimidazolium)$_2$pyridine dibromide (1 eq, 0.00164 mol, 0.7 g) was transferred to a round bottom flask and dissolved in 25 cm^2 of H_2O and 25 cm^2 of DCM. Tetrafluoroboric acid (50 % w/w, 4.8 eq, 0.00782 mol, 0.35 g, 0.984 cm^2) was then added dropwise. The formation of a precipitate was instantaneous. However, in order to assure the completion of the reaction the mixture was left stirring overnight. A white solid precipitate was obtained. The organic and the water phase were washed several times with ultrapure water. The product was separated and consequently dried *in vacuum (8·10^{-2} mbar)* overnight at 50 ºC to yield a white solid (0.69 g, 99 %).

^{1}H NMR (400 MHz, DMSO-*d*$_6$) δ 10.62 (s, 2H), 8.76 (t, *J* = 8.1 Hz, 1H), 8.44 (d, *J* = 8.3 Hz, 2H), 8.30 (t, *J* = 8.3 Hz, 4H), 7.82 (t, *J* = 7.7 Hz, 2H), 7.74 (t, J=7.8 Hz, 2H), 4.67 (t, *J* = 7.3 Hz, 4H), 2.12 – 1.96 (m, 4H), 1.48 – 1.34 (m, 4H), 0.99 (t, *J* = 7.3 Hz, 6H). ^{13}C NMR (101 MHz, DMSO-*d*$_6$) δ 146.90, 144.93, 143.27, 132.09, 130.06, 128.40, 127.89, 118.39, 116.23, 114.76, 47.72, 30.96, 19.63, 13.94. ^{19}F NMR (376 MHz, DMSO-*d*$_6$) δ: -148.30. ESI-MS (+ve) m/z 212.6318 [M^{2+}]. Elemental analysis (%): Anal. Calcd for $C_{27}H_{31}B_2F_8N_5$: C, 54.12; H, 5.22; N, 11.69; Found: C, 54.42; H, 5.43; N, 11.8.

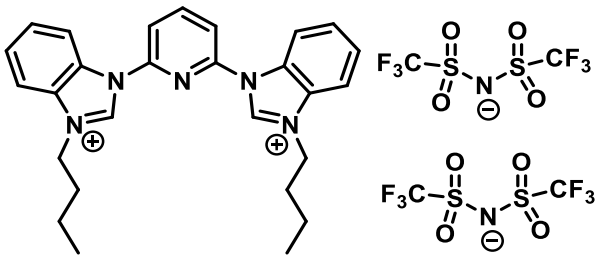
2.3.11 2,6-bis(butylbenzimidazolium)$_2$pyridine hexafluorophosphate, [(C$_4$BzIm)$_2$Py][PF$_6$]$_2$



2,6-bis(butylbenzimidazolium)$_2$pyridine dibromide (1 eq, 0.0016 mol, 0.705 g) was transferred in a round bottom flask and dissolved in 25 cm^2 of H_2O and 25 cm^2 of DCM. Hexafluorophosphoric acid solution (60 % w/w, 4.8 eq, 0.00782 mol, 1.16 cm^2) was then added dropwise (with extreme care). The formation of a precipitate was rapid. The mixture was left stirring for 12 h to assure the completion of the reaction. A white solid precipitate was obtained. The organic and the water phase were washed several times with ultrapure water. The product was separated and consequently dry *in vacuum (8·10^{-2} mbar)* overnight at 50 ºC to yield a white solid (0.67 g, 96 %).

^{1}H NMR (400 MHz, DMSO-*d*$_6$): δ = 11.64 (s, 2H), 9.59 (t, *J* = 8.1 Hz, 1H), 9.29 (d, *J* = 8.3 Hz, 2H), 9.20 (d, *J* = 8.1 Hz, 2H), 9.13 (d, *J* = 8.3 Hz, 2H), 8.65 (t, *J* = 7.7 Hz, 2H), 8.57 (t, *J* = 7.8 Hz, 2H), 5.52 (t, *J* = 7.3 Hz, 4H), 2.87 (p, *J* = 7.5 Hz, 4H), 2.31 (h, *J* = 7.4 Hz, 4H), 1.82 (t, *J* = 7.3 Hz, 6H); ^{13}C NMR (101 MHz, DMSO-*d*$_6$) δ 146.90, 144.93, 143.28, 132.09, 130.06, 128.39, 127.90, 118.38, 116.23, 114.76, 47.72, 30.96, 19.63, 13.94. ^{19}F NMR (376 MHz, *DMSO-d*$_6$) δ -69.22, -71.11. ^{31}P NMR (162 MHz, DMSO-*d*$_6$): δ = -128.23 – (-158.73) (m). ESI-MS (+ve) m/z 212.63 [M^{2+}]. Elemental analysis (%): Anal. Calcd for $C_{27}H_{31}B_2F_8N_5$: C, 45.32; H, 4.37; N, 9.79; Found: C, 45.58; H, 4.07; N, 9.76.

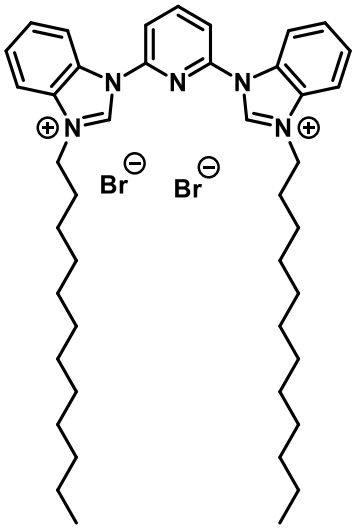
2.3.12 2,6-bis(butyllbenzimidazolium)pyridine bis(trifluoromethylsulfonyl) amide, $[(C_4BzIm)_2Py][NTf_2]_2$



2,6-bis(butylbenzimidazolium)pyridine dibromide (1 eq, 0.7 g, 0.0013 mol) was transferred to a round bottomed flask and dissolved in 20 cm^2 of ultrapure water and 10 cm^2 of DCM. Lithium bis(trifluoromethylsulfonyl)imide (4.8n eq, 79 g, 0.0062 mol) was dissolved in 20 cm^2 of ultrapure water and added to the reaction drop wise. The organic phase is yellowish showing the formation of a product. The reaction mixture was washed with water 20 cm^2 for three times in order to eliminate the excess of bis(trifluoromethylsulfonyl)imide. The product was recrystallised from acetonitrile and ethyl acetate. The organic phase was dry under reduced pressure with rotary evaporator. The product was dried *in vacuum ($8 \cdot 10^{-2}$ mbar)* overnight at 50 °C to yield a yellow viscous liquid (0.65 g, 92.8 %).

^{1}H NMR (400 MHz, DMSO-d_6) δ 10.63 (s, 2H), 8.75 (t, *J* = 8.1, 2.3 Hz, 1H), 8.45 (d, *J* = 8.4, 0.9 Hz, 2H), 8.29 (t, 4H), 7.81 (t, *J* = 8.3, 7.2, 1.1 Hz, 2H), 7.73 (t, *J* = 8.4, 7.3, 1.1 Hz, 2H), 4.66 (t, *J* = 7.3 Hz, 4H), 2.08 – 1.98 (m, 4H), 1.53 – 1.40 (m, 4H), 0.99 (t, *J* = 7.4 Hz, 6H); ^{13}C NMR (101 MHz, DMSO-d_6) δ 146.01, 144.03, 142.38, 131.20, 129.17, 127.50, 127.00, 120.64, 117.48, 115.33, 113.87, 46.84, 30.07, 18.74, 13.03; ^{19}F NMR (376 MHz, DMSO-d_6) δ -78.72. ESI-MS (+ve) m/z 212.79 [M^{2+}]. Elemental analysis (%): Anal. Calcd for $C_{31}H_{31}F_{12}N_7O_8S_4$: C, 37.77; H, 3.17; N, 9.95; Found: C, 37.67; H, 2.95; N, 9.82.

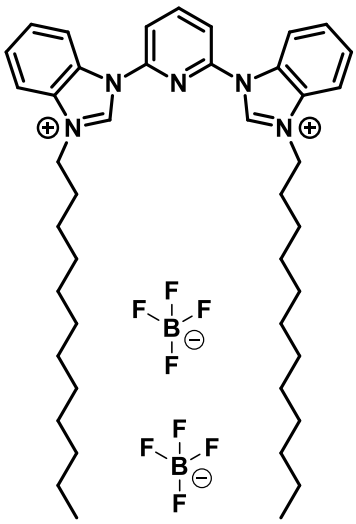
2.3.13 2,6-bis(dodecylbenzimidazolium)$_2$pyridine dibromide, [(C_{12}BzIm)$_2$Py]Br_2



2,6-bis(benzimidazolyl)pyridine (1 eq) and 1-bromododecale (30 eq) in DMF(≈5 cm^2) heated to 120 ºC for 24 h and then at 140 ºC for 48 h.[1] Once the reaction mixture cooled down the precipitate is filtrated and washed with Et_2O 2x20 cm^2 to afford a colourless powder. The mixture looked cloudy at RT. The temperature was raised to 120 ºC looking yellow and clear. After 24 h the reaction mixture looked brownish clear. Then the reaction moisture was heated to 140 ºC for 24 h. After cooling the solvent was reduced considerably under vacuum leaving a solid precipitate. (The volume was reduced of 1/3). The solid with the DMF remained was then filtered and washed several times with diethyl ether. The solid was finally recrystallise from chloroform/diethyl ether several times.

^{1}H NMR (400 MHz, DMSO-d_6) δ 10.81 (s, 2H), 8.76 (t, *J* = 8.1 Hz, 1H), 8.46 (d, 2H), 8.37 (d, *J* = 8.1 Hz, 2H), 8.28 (d, 2H), 7.81 (t, *J* = 8.4, 7.3, 1.1 Hz, 2H), 7.74 (t, *J* = 8.4, 7.3, 1.1 Hz, 2H), 4.68 (t, *J* = 7.3 Hz, 4H), 2.11 – 1.96 (m, 4H), 1.57 – 1.11 (m, 36H), 0.84 (t, 6H);^{13}C NMR (101 MHz, DMSO-d_6): δ = 146.85, 144.96, 143.32, 132.10, 129.98, 128.37, 127.84, 118.42, 116.19, 114.79, 47.92, 34.78, 31.75, 29.50, 29.44, 29.34, 29.17, 29.02, 28.97, 26.27, 22.55, 14.43. ESI-MS (+ve) m/z 324.75 [M^{2+}]. Elemental analysis (%): Anal. Calcd for $C_{43}H_{63}Br_2N_5$: C, 63.78; H, 7.84; N, 8.65; Found: C, 64.08; H, 7.94; N, 8.5

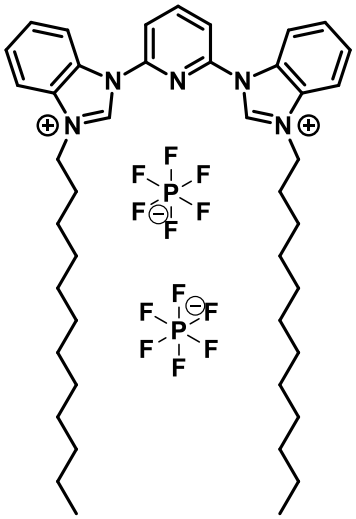
2.3.14 2,6-bis(dodecylbenzimidazolium)$_2$pyridine tetrafluoroborate, [(C_{12}BzIm)$_2$Py][BF_4]$_2$



2,6-bis(dodecylbenzimidazolium)$_2$pyridine dibromide (1 eq, 0.00089 mol, 0.7 g) was transferred to a round bottom flask and dissolved in 20 cm^2 of H_2O and 20 cm^2 of DCM. Tetrafluoroboric acid (50 % w/w, 9.6 eq, 0.00858 mol, 0.753 g, 1.04 cm^2) was then added dropwise. The formation of a precipitate was instantaneous. However, in order to assure the completion of the reaction the mixture was left stirring overnight. A white solid precipitate was obtained. The solid product was filtered and recrystallised from acetonitrile and diethyl ether. The product consequently dry *in vacuum* ($8 \cdot 10^{-2}$ mbar) overnight at 50 ºC to yield a white solid (0.64 g, 91.4 %).

^{1}H NMR (400 MHz, *DMSO-d_6*) δ 10.63 (s, 2H), 8.77 (t, *J* = 8.1 Hz, 1H), 8.46 (d, *J* = 8.4, 0.9 Hz, 2H), 8.30 (t, 4H), 7.83 (t, *J* = 8.4, 7.3, 1.1 Hz, 2H), 7.75 (t, *J* = 8.4, 7.3, 1.1 Hz, 2H), 4.66 (t, *J* = 7.3 Hz, 4H), 2.11 – 1.98 (m, 4H), 1.53 – 1.16 (m, 40H), 0.85 (t, 6H). ^{13}C NMR (101 MHz, *DMSO-d_6*): δ = 146.88, 144.96, 143.26, 132.08, 130.03, 128.39, 127.88, 118.40, 116.19, 114.77, 47.94, 31.76, 29.50, 29.47, 29.44, 29.33, 29.17, 29.01, 28.96, 26.27, 22.56, 14.43. ESI-MS (+ve) m/z 325.01 [M^{2+}]. Elemental analysis (%): Anal. Calcd for $C_{43}H_{63}Br_2N_5$: C, 62.71; H, 7.71; N, 8.50; Found: C, 63.01; H, 7.92; N, 8.50.

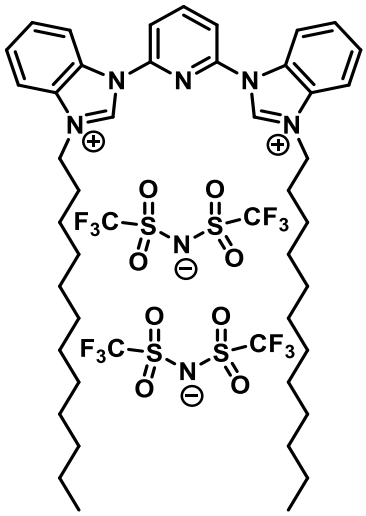
2.3.15 2,6-bis(dodecylbenzimidazolium)$_2$pyridine hexafluorophosphate, [(C_{12}BzIm)$_2$Py][PF_6]$_2$



2,6-bis(dodecylbenzimidazolium)$_2$pyridine dibromide (1 eq, 0.00089 mol, 0.7 g) was transferred to a round bottom flask and dissolved in 20 cm2 of H_2O and 20 cm2 of DCM. Hexafluorophosphoric acid (60 % w/w, 9.6 eq, 0.00858 mol, 1.24 g, 1.24 cm^2) was then added dropwise. The formation of a precipitate was instantaneous. However, in order to assure the completion of the reaction the mixture was left stirring overnight. A white solid precipitate was obtained. The solid product was filtered and recrystallised from acetonitrile and diethyl ether. The product consequently dry *in vacuum* ($8 \cdot 10^{-2}$ mbar) overnight at 50 ºC to yield a white solid (0.63 g, 90 %).

^{1}H NMR (400 MHz, *DMSO-d$_6$*) δ 10.62 (s, 2H), 8.76 (t, *J* = 8.1 Hz, 1H), 8.45 (d, *J* = 8.4 Hz, 2H), 8.30 (t, *J* = 8.5 Hz, 4H), 7.82 (t, *J* = 7.8 Hz, 2H), 7.74 (t, *J* = 7.8 Hz, 2H), 4.65 (t, *J* = 7.3 Hz, 4H), 2.04 (p, *J* = 7.3 Hz, 5H), 1.52 – 1.17 (m, 44H), 0.85 (t, *J* = 6.5 Hz, 6H). ^{13}C NMR (101 MHz, *DMSO-d$_6$*) δ 146.90, 143.27, 132.10, 130.04, 128.40, 127.90, 118.41, 116.20, 47.95, 31.76, 29.50, 29.47, 29.44, 29.33, 29.17, 29.01, 28.95, 26.27, 22.55, 14.42. ^{19}F NMR (376 MHz, *DMSO-d$_6$*) δ -69.22, -71.11. ^{31}P NMR (162 MHz, DMSO-*d$_6$*) δ -129.37 – -158.94 (m). ESI-MS (+ve) m/z 325.01 [M^{2+}]. Anal. Calcd for $C_{43}H_{63}F_{12}N_5P_2$: C, 54.95; H, 6.76; N, 7.45; Found: C, 54.97; H, 6.84; N, 7.34.

2.3.16 2,6-bis(dodecylbenzimidazolium)pyridine bis(trifluoromethylsulfonyl) amide, $[(C_{12}BzIm)_2Py][NTf_2]_2$



2,6-bis(dodecylbenzimidazolium)pyridine dibromide (0.7 g, 0.0013 mol) was transferred to a round bottomed flask and dissolved in 20 cm^2 of ultrapure water and 10 cm^2 of DCM. Lithium bis(trifluoromethylsulfonyl)imide (1.29 g, 0.0043 mol) was dissolved in 20 cm^2 of ultrapure water and added to the reaction drop wise. The organic phase is yellowish showing the formation of a product. The reaction mixture was washed with water (3 x 20 cm^2) in order to eliminate the excess of bis(trifluoromethylsulfonyl)imide. The product was recrystallised from acetonitrile and ethyl acetate. The organic phase was dry under reduced pressure with rotary evaporator. The product was dried *in vacuum ($8 \cdot 10^{-2}$ mbar)* overnight at 50 °C to yield a yellow viscous liquid (0.67 g, 95.7 %).

^{1}H NMR (400 MHz, DMSO-d_6) δ 10.61 (s, 2H), 8.75 (t, *J* = 8.1 Hz, 1H), 8.44 (d, *J* = 8.4, 1.0 Hz, 2H), 8.28 (t, 4H), 7.81 (t, *J* = 8.4, 7.3, 1.1 Hz, 2H), 7.73 (t, *J* = 8.4, 7.4, 1.1 Hz, 2H), 4.64 (t, *J* = 7.3 Hz, 4H), 2.10 – 1.97 (m, 4H), 1.49 – 1.18 (m, 26H), 0.84 (t, 6H); ^{13}C NMR (101 MHz, DMSO-d_6) δ 146.89, 143.26, 132.08, 130.04, 128.38, 127.89, 118.39, 116.19, 114.77, 47.94, 31.75, 29.50, 29.46, 29.43, 29.33, 29.16, 29.00, 28.95, 26.27, 22.55, 14.42; ^{19}F NMR (376 MHz, *DMSO-d_6*): δ = -78.72. ESI-MS (+ve) m/z 325.01 [M^{2+}]. Anal. Calcd for $C_{43}H_{63}F_{12}N_5P_2$: C, 46.64; H, 5.25; N, 8.45; Found: C, 46.97; H, 5.54; N, 8.50.

2.4 Synthesis of nickel nanoparticles

The synthesis of nickel nanoparticles was performed using a modified literature protocol of T. Hyeon *et al.* using different organic capping layer to stabilise the nanoparticles.[2]

2.4.1 Nickel phosphorus stabilised nanoparticles

Ni-oleylamine complex was prepared by reacting nickel(acetylacetonate)$_2$ [Ni(acac)$_2$], (0.52 g) with 2 cm^2 of oleylamine (Aldrich Chemical Co., technical grade, 80%) in a schlenk flask sealed under Argon atmosphere at 100 °C. The blue resulting metal complex mixture was transferred into a thee neck round bottom flask with trioctylphosphine (TOP, 5g of Aldrich Chemical Co., 90%) under argon. The temperature was kept constant and raised up to 215 °C. The colour of the solution changed from green to black, indicating that colloidal nanoparticles were generated.[2] The black solution was aged at 200 °C for 30 min. The precipitated nanoparticles were cooled to room temperature and 20 cm^2 of ethanol were added. The mixture was centrifuged at 8040 g/min for half an hour. The procedure was repeated three times and the yield of the overall synthesis was 60%$_{(w/w)}$ based on the amount of Ni(acac)$_2$."[2]

2.4.2 Nickel N-Heterocyclic Carbene stabilised nanoparticles

Ni-oleylamine complex was prepared by reacting nickel(acetylacetonate)$_2$ [Ni(acac)$_2$], (0.52 g) with 2 cm^2 of oleylamine (Aldrich Chemical Co., technical grade, 80%) in a schlenk flask sealed under Argon atmosphere at 100 °C. The blue resulting metal complex mixture was transferred under argon into a three neck round bottom flask with 2,6-bis(octylbenzimidazolium) pyridine dibromide (5 g of Aldrich Chemical Co., 90%) previously dried under vacuum. The temperature was kept constant and raised up to 220 °C. The colour of the solution changed from green to black, indicating that colloidal nanoparticles were generated. The black solution was aged at 200 °C for 30 min. The precipitated nanoparticles were cooled to room temperature and 25 cm^2 of ethanol were added. The mixture was centrifuged at 8040 g/min for half hr. The procedure was

repeated three times and the yield of the overall synthesis was 53%$_{(w/w)}$ based on the amount of Ni(acac)$_2$."

2.5 The encapsulation of nanoparticles into hollow carbon nanostructures

The carbon nanostructures used in this study are graphitised nanofibres. Carbon graphitised nanofibres (GNF), they were pre-treated at 500 °C for one hour to remove residual moisture.

2.5.1 Insertion of nickel nanoparticles into multiwalled carbon nanofibers

GNF (0.005 g) pre-heated at 500 °C were added to TOP or NHCs-stabilised nickel nanoparticles (0.001 g) in a schlenk tube. A solution of acetone (5 cm^2) was added and the resulting black suspension was vigorously stirred for 20 minutes at room temperature. Acetone was added and then the solvent was slowly evaporated under vacuum. The procedure was repeated for three times. The mixture was then filtered using a 0.45 µm pore size PTFE membrane filter and washed with acetone (50 cm^2) before final drying under vacuum to yield a black solid (0.008 g).

2.6 Material characterisation techniques

X-Ray Photoemission Spectroscopy (XPS), Energy-dispersive X-ray spectroscopy (EDX) and Thermogravimetric Analysis (TGA) were used for qualitative and quantitative analysis. To appraise the synthesis and encapsulation of nanoparticle into graphitised hollow nanofiber the Transmission Electron Microscopy (TEM) is the only technique which allows to determine the location of the particles on and in cylindrical nanostructures. Finally, a brief overview of Cyclic Voltammetry (CV) is presented that was used to test the electrochemical reactions on Ni nanoparticles.

2.6.1 Sample handling

The samples for the purpose of surface characterisation using XPS were prepared with a solution of acetonitrile on silica plates supported onto XPS a sample bar. Data analysis was performed using CASA XPS software.

The samples for TEM analysis were prepared by casting several drops of alcohol suspensions of particles into copper-grid mounted ‘‘holey’’ carbon films, and particles anchored to GNF onto copper-grid mounted “lacey” carbon film, Figure 2.1.

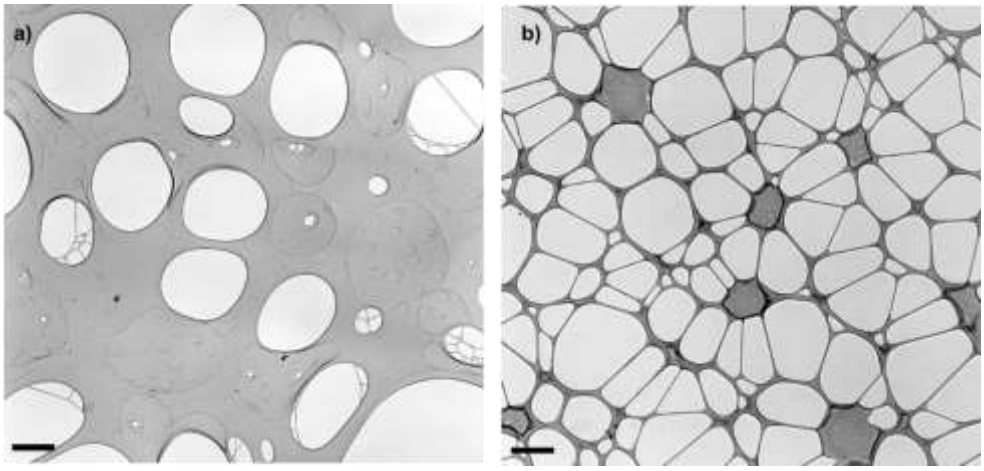


Figure 2.1 a) Holey Carbon Films on 200 Mesh Copper Grids; b) Lacey Carbon Films on 200 Mesh Copper Grids. Scale bars 1 μm (a), 1 μm (b).

Image analysis was performed using Gatan Digital Micrograph software. The size, the average diameter of nanoparticles and length of carbon graphitised nanofibres were determined by taking bright field micrographs from multiple fields of view and averaging across the entire sample.

2.6.2 Chemical analysis

XPS was utilised to determine the chemical composition and the electronic distribution of the ionic compounds. EDX was mainly used to determine the chemical composition of the new nanoparticles and the functionalised graphitised nanofibres. In this section the techniques are briefly introduced.

2.6.2.1 XPS

Surface studies demonstrate that the type of ligand influences the position of the catalytic active species at the interface of the ionic liquids.[3] This field still in its infancy is promising for future application of functionalised ionic liquids. In this direction a key solution is the application of the study of ionic liquids with surface technique such as XPS (X-Ray Photoemission

Spectroscopy) that guide toward a better understanding of interaction between ILs and substrates.[4, 3]

The XPS is an experimental technique that allows analysing the surface of the samples. The surface sensitivity depends upon the inelastic mean free path of the electrons, which limits the detection of the electrons below 10 nm. The XPS is based on the photoelectric principle, Figure 2.2.[5]

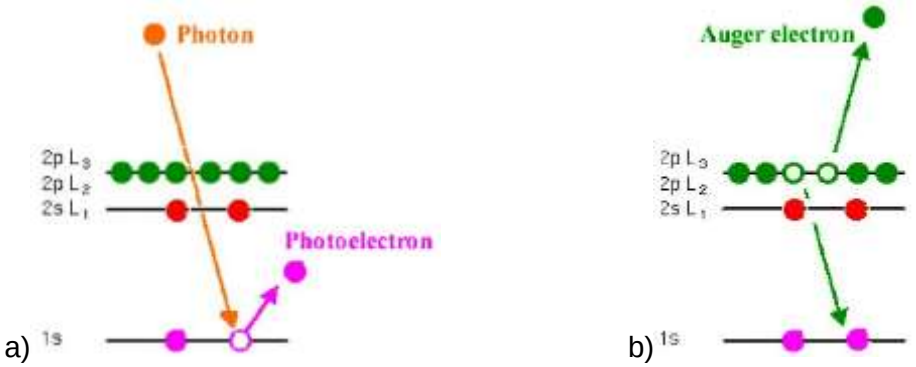


Figure 2.2 Representation of a) The photoelectric effect; b) The auger electron emission.

The X-Ray photon accesses the core shells electron of an atom and a photoelectron is consecutively ejected. Sometime, the photoelectric effect is followed by a relaxation phenomenon of the system. In this case an electron from the external electron levels fills the gap created at the core levels and consequently and another electron is ejected from the same outer level. The B.E. (Binding Energy) of the core electron is associated with the K.E. (Kinetic Energy) though the Einstein's equation:

$$B.E. = h\nu - K.E. - \varphi$$

Where $h\nu$ is the energy of the photon and φ the working function of the instrument. The equipment is constituted by a monochromatic X-ray source Al Kα emission at 1486.6 eV, a crystal quartz monochromator, a hemi-spherical Analyser and a detector, Figure 2.3.

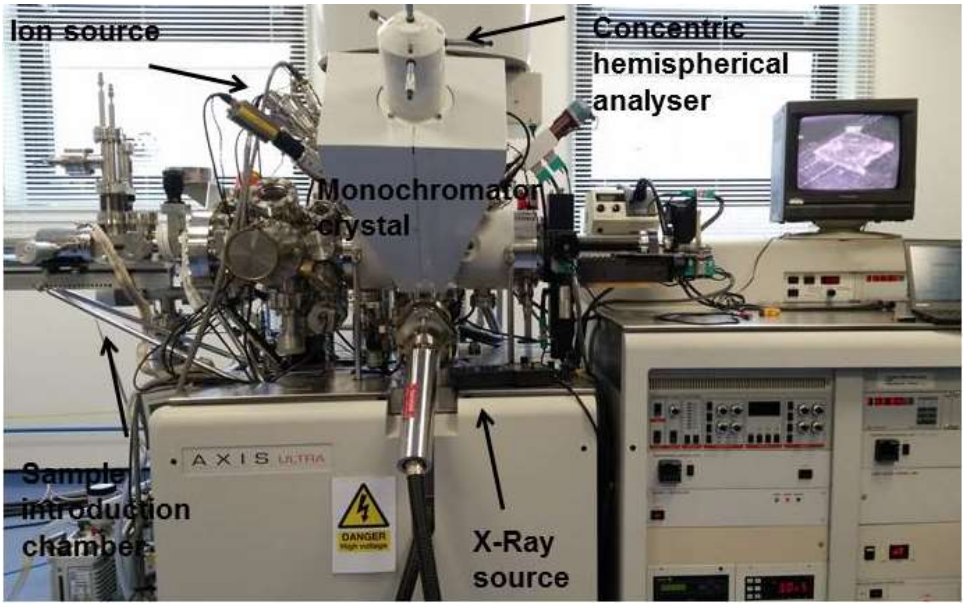


Figure 2.3 Image of XPS Analyser.

The X-Rays are produced by hitting the aluminium anode with high energy source. Then, the electrons are diffracted within a crystal lattice to produce a narrow X-Ray line by diffraction allowing better-resolved peaks in the survey. Moreover, the monochromator separates the X-Ray source from the sample preventing its overheating and damaging. The photoelectrons emitted from the sample are headed to a system of electromagnetic lenses which focus them into the hemi-spherical analyser. The analyser consist of two concentric plates (hemispherical electrodes) connected with a systems of different voltages lens where the photoelectrons received are slowed to achieve better detection that reflect in higher resolution and better sensitivity.

The XPS spectra are plots of electron counts per second versus B.E. The acquisition contains two types of spectra:

- Survey Scan: wide energy range between 0 - 1400 eV to detect all possible transitions and elements (apart from hydrogen and helium) present in the sample
- High Resolution Scan: focused energy range to achieve better resolution compared to the wide scan and to allow accurate determination of peak binding energy for each element analysed. The binding energy depend upon the electronic environment of the atom. An

electron deficient environment of an element is reflected in higher B.E. whereas electron rich environment in lower B.E.

The survey of an experiment present two types of peaks:

- Auger peaks: arise from electrons emitted from relaxation of the photo-excited state, Figure 2.2 b).
- Photoemission peaks: arise from photoelectron emissions, (Figure 2.2 a).

The technique allows qualitative and quantitative analysis measuring the K.E. of the inelastic and not-scattered photoelectrons. The quantification of each element is determined by the photoemission peak areas scaled with the Relative Sensitivity Factors (RSF) in order to obtain representative values of the element in the specimen surface. The relative sensitivity factors are taken from reference values, e.g. the Kratos library.

XPS experiments must be carried out under ultra-high vacuum (UHV) (10^{-8}-10^{-10} mbar) to avoid energy losses via gas phase collisions and adsorption of gas molecules onto the sample surface. Ionic liquids possess low vapour pressures (≤ 10^{-8} mbar) consequently they are ideal analytic subjects of UHV techniques.[6,7]

Every photoelectron of given energy state is characterised by four quantum numbers, n (principal quantum number), l (orbital), s (spin) and j (spin-orbit coupling with j = l + s). The latter can only have values with J always positive. The nomenclature used to indicate the electrons comes from both the spectroscopic and X-Ray notation which are summarised in Table 1.1.

Table 1.1 The relationship between quantum numbers, spectroscopists' notation and X-Ray notation.[8]

Quantum numbers					Spectroscopists' notation	X-Ray notation
n	l	s		j		
1	0	+1/2	-1/2	1/2	$1s_{1/2}$	K
2	0	+1/2	-1/2	1/2	$2s_{1/2}$	L_1
2	1	+1/2		1/2	$2p_{1/2}$	L_2
2	1		-1/2	3/2	$2p_{3/2}$	L_3
3	0	+1/2	-1/2	1/2	$3s_{1/2}$	M_1
3	1		-1/2	3/2	$3p_{1/2}$	M_2
3	1	+1/2		3/2	$3p_{3/2}$	M_3
3	2	+1/2			$2d_{3/2}$	M_4
3	2		-1/2		$2d_{5/2}$	M_5
						etc.

K, L and M in the X-Ray notation are the principal quantum numbers are given letters. The photoelectrons are indicated as "Spectroscopists notation" and the Auger electrons are indicated by the X-Ray notation.

2.6.2.2 Energy Dispersive X-Ray Spectroscopy

Energy Dispersive X-Ray Spectroscopy (EDX) allows the chemical analysis of a selected area of a samples in a scanning electron microscope (SEM) or TEM.[9] The technique allows chemical characterisation and elemental analysis.

As previously explained, paragraph 2.6.2.1, the interaction of a high energy electron beam with the inner electron shell of an atom generates the ejection of a photoelectron. An electron from the outer electron shell jump where is left the lack and energy is consequently emitted in the form of an X-Ray photon. As the difference of energy between the core and the outer level depends upon the atomic number it can be used to determine the composition of a specimen. The atomic number and the energy of a given X-Ray are connected with the Mosely's law:

$$\sqrt{E} = C_1(Z - C_2)$$

Where E is the energy of the radiation for a given X-ray series (e.g. Kα, Kβ, Lα, Mα, etc.), Z is the atomic number and C_1 and C_2 are the constants.

The EDX analysis was performed using Oxford Instruments 80mm X-Max system for energy dispersive x-ray spectroscopy analysis on a JEOL 2100F FEG-TEM operated at 200 kV.

2.6.3. Material characterisation techniques

The diffraction gives information on the crystallographic structure of samples. In this thesis TEM is the technique mainly used to study the structure of materials and especially attesting in situ filling of the graphitised nano-fibres. The following paragraphs describes the principle of the technique and the operating system.

2.6.3.1 Interaction of waves with crystal structures

A wave is a perturbation though a medium with a transfer of energy. A wave is described by an amplitude, a wavelength and a direction, Figure 2.4.

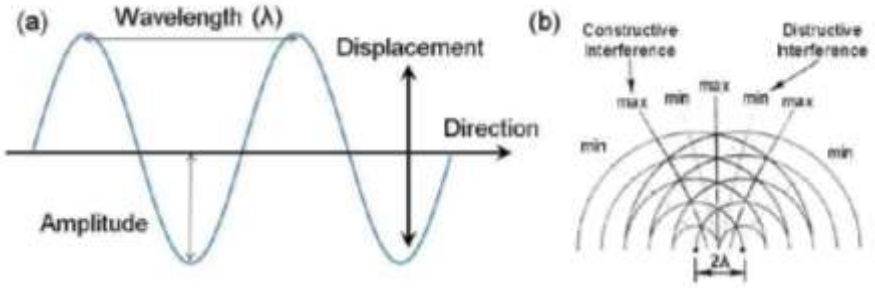


Figure 2.4 Schematic diagram of a) a transverse wave and b) interaction of waves with an obstacle, resulting in constructive and destructive interference.[10]

According to Huygens' Principle, a wave can be imagined as a spherical spreading movement of every point along its wave front. When waves meet an obstacle, they spread spherically from the obstruction point. Two kinds interference between waves are possible: constructive interference or destructive interference (Figure 2.4 b).

For example X-Rays when interact with matter can be scattered by atoms in the crystal lattice. The interference of different waves scattered from different atoms generates a pattern of constructive and destructive interferences. The result of these interactions provides information on the atomic structure of the material, which is described by the structure factor for an *hkl* reflection, F:

$$F_{hkl} = \sum_{1}^{N} f_n e^{2\pi i(hu_n + hv_n + lw_n)}$$

Which represent the scattered wave by atoms of a crystal unit cell as a summation function of a unit cell with 1,2,3,.. N atoms and fractional coordinates, $u_1 + v_1 + w_1$, $u_2 + v_2 + w_2$, $u_3 + v_3 + w_3$,…; the amplitude of each scattered waves is given by f the atomic scattering factor, f, which depends upon the incident radiation. There are different types of radiation used to study the atomic structure, X-Rays or Electrons.

2.6.3.2 A brief introduction to Diffraction

The best technique to study the structure of material measuring the unit cell of a crystal and three-dimensional arrangement of atoms is based on diffraction experiments. There are several techniques which use diffraction, X-Ray Diffraction (XRD), electron diffraction and neutron diffraction. A diffraction experiment involves a wave which hit a specimen with wavelength comparable to spacing between atoms.[10] Bragg's law describes an interference of a wave scattered from two atomic planes, as illustrated in Figure 2.5.

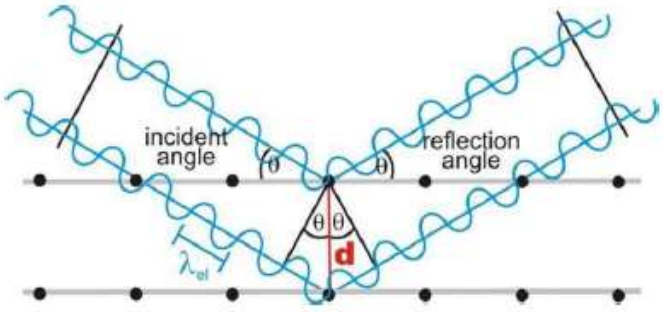


Figure 2.5 Illustration of the interference of a wave scattered from two atomic planes separated by a spacing d.[10]

Two parallel X-Rays are incident onto two parallel atomic planes and diffraction occurs when the Bragg's law is fulfilled:

$$2d \sin\theta = n\lambda$$

θ is the incident angle is and d is the interplanar spacing, λ is the wavelength of incident wave and n is the order of diffraction. The difference in the length of the radiation path according to Figure 2.5 corresponds to $2d \sin\theta$. In a sample is expected to find several diffraction planes. For

instance for a (100) of a simple cubic structure diffracting plane, the Bragg law can be re-write as:

$$2d_{100}\ \sin\theta = 2\lambda$$

For a cubic crystal the interplanar spacing d_{hkl} with planes labelled by Miller indices hkl is:

$$d_{hkl} = \frac{a_0}{\sqrt{h^2 + k^2 + l^2}}$$

Where a_0 is the crystal lattice parameter. The TEM consists of an X-Ray spectrometer as integral part of the microscope.

2.6.3.3 Electron microscopy

Electron microscopy is the technique used in this project to obtain information on structure, morphology and elemental composition of materials. A sample is hit by an energetic electron beam to extract information on a nanoscale structure. The following paragraphs illustrate the theory, which is based upon the interaction of high-energy electrons with matter.

2.6.3.4. Interaction of high energy electrons with matter

The electron beam can be described as a series of waves or a series of particles. It presents a wave-particle duality described by the de Broglie's theory in which the wavelength of a high energy electron is given by:

$$\lambda = \frac{h}{2m_0 eV(1 + \frac{eV}{2m_0 c^2})}$$

Where h is the Planck constant, m_0 is the rest mass of an electron, e is the electron charge, V is the potential difference through which the electron is accelerated and c is the speed of light. All the process taken place in TEM are of summarised in Figure 2.6.

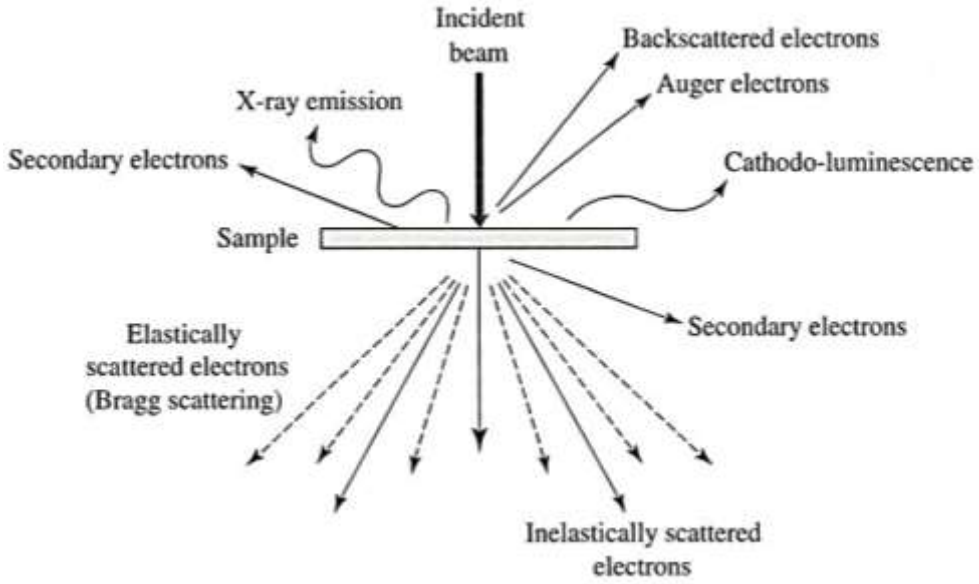


Figure 2.6. Interaction of a beam of high-energy electrons with a sample: electron scattering and secondary signal generation.[10]

Incident electrons are scattered by either electrons or nuclei in an atom. The interaction of the electron beam with the specimen allows the ejection of inner-shell electrons which produces a wide range of signals described in Figure 2.6. The signal generated from elastically scattered electrons in the TEM generate a diffraction pattern and EDX analysis allows chemical analysis.

i

2.6.3.5. Transmission electron microscopy

The TEM consists of a number of electron and optical components, which are illustrated, in Figure 2.7.

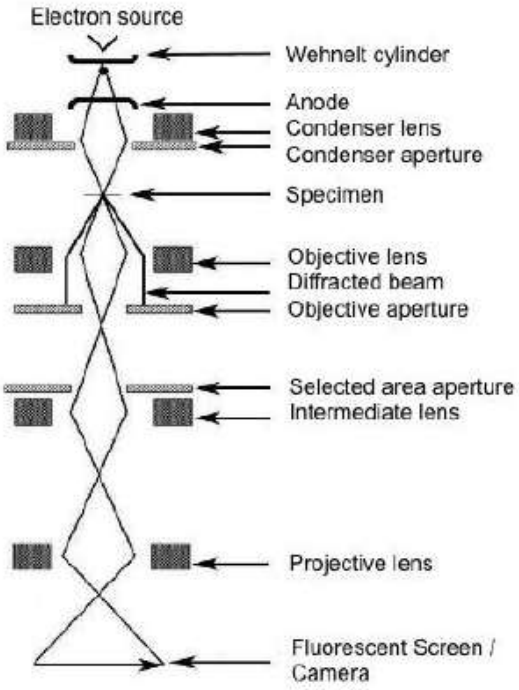


Figure 2.7 Schematic diagram of the basic electron-optical components of a TEM.[10]

The electrons are produced by thermionic emission of a W or LaB_6 or a W by field emission of a single crystal W filament gun. Then, they are accelerated though an anode at high energy (100-400 kV). A series of condensers lenses focus the electrons onto a probe, which allows controlling the number of electrons incident on the sample varying the spot size and beam current density. The sample is generally inserted in a plane normal to the optic axis. The sample has to be less than 100 nm thick and the electron beam is transmitted through it. The resolution of the TEM approaches the atomic scale and depends in theory upon the wavelength λ of the incident electron beam. Due to practical reason the resolution is influenced also by the aberration associated with the electron optics. The objective aperture is located at the back of the plane of the objective lens and allows to filter only transmitted electrons with small scattering angle which give high contrast image. The image is projected onto an electron sensitive fluorescent screen or a charge couple device and saved in digital

format. The image can be formed by either transmitted or scattered electrons.

There are thee modes of contrast formation in TEM images:

- Mass thickness contrast. Thick region in amorphous samples appear dark;
- Z-contrast, samples made of elements with high atomic number appear dark;
- Diffraction contrast. Low index crystallographic orientations of crystalline samples which satisfy the Bragg's Law appear dark;
- Phase contrast. HRTEM images derived from constructive and destructive interferences of the electron waves show atomic resolution of crystalline lattice.

There are two possible imaging conditions:

- Bright Field (BF). Images obtained with the transmitted beam, Figure 2.8 (a).
- Dark Field (DF). Images obtained with the beam aligned to the optic axis of the microscope, Figure 2.8 (b).

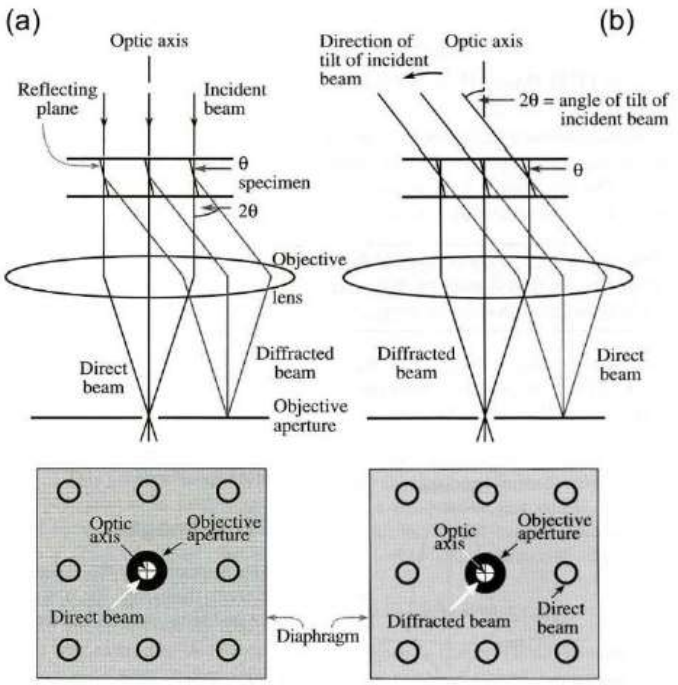


Figure 2.8 Schematic representation of the formation of a BF image a) and a DF image b).[10]

The instrument used in this work is the JEOL 2100F FEG-TEM which possesses a field emission electron gun (FEG) which provides high brightness and high stability electron source for the use at 100 and 200 kV, Figure 2.9. The point resolution of this microscope is 0.19 nm. The microscope is equipped with detectors for BF STEM and High Angle Annular DF (HAADF) STEM imaging.



Figure 2.9 JEOL 2100F FEG-TEM in the Nanoscale and Microscale Research Centre (nmRC) at the University of Nottingham.

The variant technique of STEM within the TEM is a valid tool for the characterisation of nanostructures, providing a range of different imaging modes with the ability to provide information on elemental composition and electronic structure. The usual detectors include a BF detector that intercepts the transmitted beam and annular dark field (ADF) detector that surrounds the transmitted beam to collect scattered electrons. The inner angle of this detector can be changed with post-specimen lenses from just outside the incident beam cone, which gives maximum efficiency for collecting scattered electrons, to several times the angle, that enhances the

atomic number (Z) dependence on the image contrast. This latter configuration is often referred to as Z-contrast or HAADF imaging.

2.6.4. Thermogravimetric analysis

The molecules prepared in this project have been thermally investigated. A detailed understanding of the long-term thermal decomposition behaviour of ionic samples, including knowledge of the upper operational temperature limit, is crucial for their application as substrates for catalysts. Therefore, degradation of the ionic liquid will reduce the efficacy of the processes and the build-up of volatile or corrosive decomposition products.[11] The Thermogravimetric Analysis (TGA) determines the variation of the weight of a sample as a function of the temperature. All the measurements were carried out using the Instrument TGA Q500 V20 with a dynamic TGA program in the department of inorganic chemistry. The measured temperature is plotted against the variation of percentage weight of the sample with constant heating rate. The TGA of bis(ylidene) pyridine compounds were recorded within a range of temperatures between 20 ºC and 500 ºC whereas the complexes were analysed in a bigger interval between 20 ºC and 1000 ºC.

The physical-chemical variations associated with weight loss depend upon increment of the temperature and are reflected in the total mass variation. There are some physical-chemical changes that depend upon changes in temperature, e.g. desorption, absorption, vaporisation and decomposition. There are two important parameters in TGA analysis:

- T_i procedural decomposition temperature: lowest temperature which correspond at the first mass change of the sample (peak onset),
- T_f final temperature: lowest temperature at which the variation in weight is completed.

As the interval (T_f-T_i) depends upon the program set-up in each experiment and the nature of the compound under analysis as they do not have a fixed value. The Thermograms present specific shape and characteristic parameters such as the first derivative which indicates the greatest rate of change of the slope in the weight loss profile which correspond a temperature, the T_p. The shape of a TGA analysis is typically represented by a decomposition profile single or multi-stage which starts with a plateau

and ends with a plateau. The decomposition temperature is represented by a drastic change in the TGA curve.

2.6.5 Gas Chromatography Mass Spectrometer

Gas Chromatography Mass Spectrometer (GC-MS) is an analytical tool which combines a Gas Chromatography with a Mass Spectrometer which allow the identification of the molecular weight of molecules. A GC-MS consists of a sample injector, an ion source, a mass analyser and a detector. The ion source, the mass analyser and the detector are under vacuum. The ion sources can be of three types:

- EI: Electron Ionisation
- CI: Chemical Ionisation
- MALDI: Matrix Assisted Laser Desorption/Ionisation
- ESI: Electrospray Ionisation.

The instrument used in this project is equipped with an ESI source. The sample is injected into the sheath gas flow where a potential is applied (2-5 kV) positively charged for positive ion formation and negative for negative ion formation. The ions once formed are accelerated from the source to the analyser with a Time of Flight (ToF) analyser. The ToF uses an electric field to accelerate ions from the region with an applied potential to a field-free region and measures the time of this pathway. The ToF is function of its m/z: the ion with lowest m/z arrive to the detector first. The detector is an electron multiplier also called multi-channel plates.

2.6.6 Nuclear magnetic resonance

The nuclear magnetic resonance (NMR) is used to determine the structure of organic compounds. Some of the nuclei that can be analysed are: ^{1}H, ^{13}C, ^{15}N, ^{19}F, ^{31}P, ^{11}B. In an NMR experiment a sample is placed in a magnetic field B_0, the spin of the atoms are aligned into two states (α and β) and the energy difference of energy between these states is ΔE. When a sample is subjected to a pulse of radiation (radio frequency) whose energy corresponds to ΔE, the nuclei in the α-state are promoted to the β state by flipping the spin. When the nuclei undergo relaxation (return to the original state) they emit electromagnetic signal whose frequency depends upon the difference in energy between α and β, according to the following equation:

$$\Delta E = h\nu = h\frac{\gamma}{2\pi}B_0$$

Where γ is the gyromagnetic ratio and depends on the magnetic moment of the nucleus, h is the Planck constant. As the nuclei relax they produce a signal named Free Induction Decay (FID) a signal of intensity as function of time. All the NMR spectra are reported with the Fourier transform (FT) as a signal of intensity plotted as function of frequency. NMR spectra are annotated in chemical shift δ (ppm) where:

$$\delta = \frac{Distance\ downfield\ from\ TMS\ (Ttetramethylsilane) in\ Hz}{Operating\ Frequency\ of\ the\ spectrometer\ in\ MHz}$$

A nucleus is surrounded by electrons which partly shield it from the applied magnetic field. Protons in a molecule experience different effective magnetic field. Protons in electron-dense environments sense a smaller effective magnetic field. Hence, they require lower frequency of the operating frequency to come to resonance and they are present at high frequency and large δ, vice versa for proton in electron-poor environment.

2.6.7 Elemental Analysis

The elemental analyser determines the percentage of C, H and N in a sample. When a sample is injected into a CHN analyser it is burned at high temperature. The first chamber is constituted by a combustion tube under O_2 at 975 ºC followed by a reduction tube under helium flow at 625 ºC to remove undesirable product and finally a thermal conductivity detector which separate the amount of water and CO_2 to get the H content and the O content. Finally N_2 remains mixed with helium, the N content is obtained by comparison with the helium reference.

2.6.8 Electrochemistry

Nickel capped nanoparticles in GNF have been proved electrocatalytically active for the oxidation reaction of propargyl alcohol to propiolic acid. The first section will explore the background of the reaction. The second part of this section explores the technical details of the samples preparation and the electrochemical measurements.

2.6.8.1 Cyclic Voltammetry

Cyclic voltammetry (CV) provides qualitative information on the thermodynamics and kinetics of redox processes. Particularly CV can be applied to study the kinetics of heterogeneous electron-transfer reactions[12]. An experiment of cyclic voltammetry is obtained by applying a potential that increases or decreases linearly with time to the working electrode. As the applied potential reached the formal potential, E°, of an analyte, a current flows through the electrode that either oxidizes or reduces the analyte. The two most relevant parameters in a voltammogram are the peak potential E_p, the potential recorded for the anodic and cathodic processes respectively and the peak currents i_p which can be individuated in correspondence of E_p into both the half side of a CV as anodic peak potential (E_{pa}) and cathodic peak potential (E_{pc}), Figure 2.9.

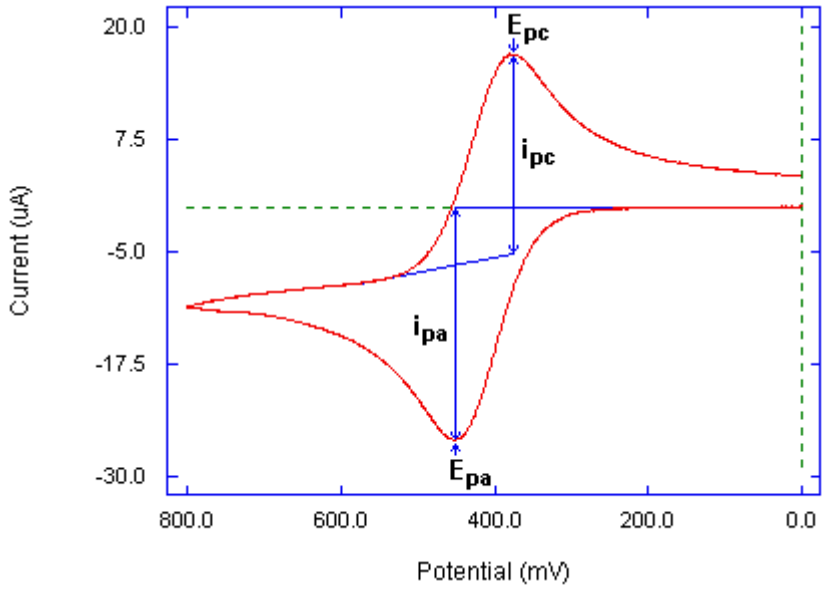


Figure 2.9 Cyclic voltammogram showing the peak currents i_p which can be individuated in correspondence of E_p into both the half side of a CV as anodic peak potential (E_{pa}) and cathodic peak potential (E_{pc}).

The current is proportional to the concentration of the analyte in solution which allows to use the technique for analytical determination of concentration. The equipment used to perform cyclic voltammetry is a conventional three-electrode potentiostat connected to three electrodes (working, reference and auxiliary) immersed in the analyte in a closed

glassware systems connected to a Schlenk line apparatus. The potentiostat applies a potential between reference electrode and the working electrode and at the same time measuring the current at the working electrode. A redox process is termed electrochemically reversible when the distance between peaks at low scan rate is close to the value theoretically expected for a reversible process of $\Delta E_p = 2.218 \cdot RT/F = 57$ mV at 298 K and the peak current increases with the square root of the scan rate, where R is the universal gas constant, T is the absolute temperature (K), F the Faraday constant.[12]

The shape of an electrochemically reversible voltammogram is based on the Flick's law and the Nernst's Law. The Fick's law of diffusion for a planar electrode is

$$\frac{d[A]}{dt} = D\frac{d^2[A]}{dx^2}$$

which describes the mass transport process towards the electrode where A is the concentration of the oxidised species, D is the diffusion coefficient, x is a parameter which denotes the distance of the species from the electrode surface.

The Nernst's law is:

$$\frac{[A]_{x=0}}{[B]_{x=0}} = e^{\frac{nF(E(t)-E_c)}{RT}}$$

where [A] and [B] are the concentration of the oxidised, $[A]_{x=0}$ and the reduced, $[B]_{x=0}$ redox species for a generic reaction A + ne^- ↔ B as function of $E_{(t)}$ and E_c, the applied potential and the formal reversible potential respectively, t is the time and n the number of electrons transferred per molecule of A reacting at the electrode surface, *F*, the Faraday constant, *R*, the constant for an ideal gas, and *T*, the absolute temperature.

The dependence of the peak current, I_p, on scan rate, ν, are related by the following equation which considers the diffusion-controlled process written negative as a reductive process:

$$I_p = -0.446\, nFA\, [A]_{bulk}\sqrt{\frac{nF\nu D}{RT}}$$

Where *F*, the Faraday constant, A the concentration of the oxidised specie, D the diffusion constant, *R*, the constant for an ideal gas, and *T*, the absolute temperature.

2.6.8.2 Technical details of the electrochemical experiments

All electrochemical experiments were performed using an AUTOLAB PGSTAT302N potentiostat. Cyclic voltammetry (CV) measurements were performed in a three-electrode configuration with the electro catalyst working electrode, platinum wire counter electrode and Ag/AgCl reference electrode, Figure 2.10. The electrode is a reticulated vitreous carbon (RVC).

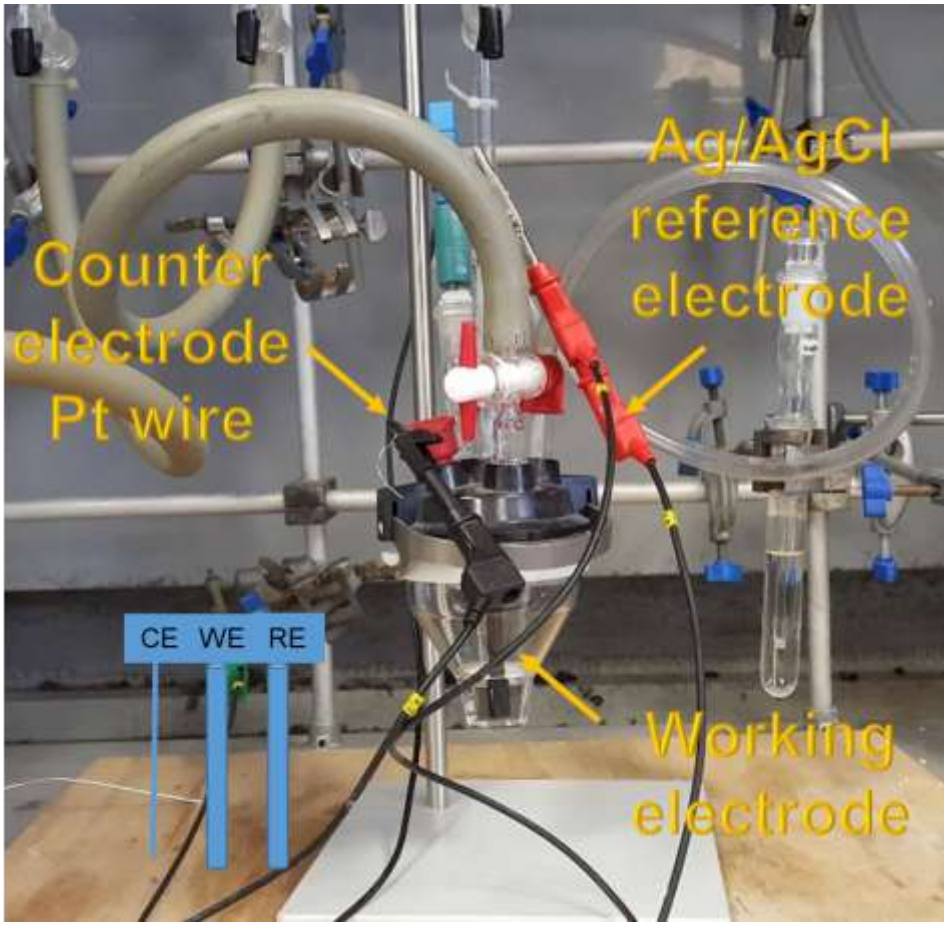


Figure 2.10 Cyclic voltammetric cell. The system studied in this thesis was analysed by varying the potential in the electrochemical window of the electrolyte (NaOH 0.1 M): between +1 and -1 eV.

The preparative electrocatalytic reactions were performed in a three-electrode configuration with the electrocatalyst working electrode, platinum

wire counter electrode and Ag/AgCl reference electrode. A 1M sodium hydroxide aqueous solution (30 cm^2) containing propargyl alcohol (2.25 mmol) was stirred whilst electrolysed at a constant potential of 0.570 V, determined by cyclic voltammetry, for the required duration of 6 hours. The solution was then acidified to a pH of 3 with 2M phosphoric acid. The product was extracted from the aqueous mixture with ethyl acetate (3 x 10 cm^2). The organic layer was then dried using anhydrous magnesium sulphate and concentrated under reduced pressure with the rotary evaporator. The conversion was determined by ^1H NMR spectroscopy of the extracted product.

2.6.8.1 Sample preparation

Tailored nickel loadings were manufactured by using two type of nanoparticle TOP stabilised and NHCs stabilised. The nickel loading was determined by TGA and corresponds to 10 %. The electro catalyst material (0.001 g) was suspended in toluene (1 cm^2) and carefully dispersed by sonication. This suspension was then slowly drop-cast onto a piece of reticulated vitreous carbon (RVC) and dried under a flow of argon. The nanoreactor/RVC composite was then attached to a glassy carbon rod.

2.6.9 Data handling

The analytical data obtained from each characterisation methods are processed to obtain the graphical representation reported and outlined in the discussion of each chapter. XPS spectra were analysed with CASAXPS™ software and handled with Igor Pro, further details are reported in section 2.6.9.1. EDX spectra were collected with the TEM using an Oxford Link Isis package and exported in .txt format to be elaborated with Excel. TEM images were recorded using a CCD camera and processed using Gatan Digital Micrograph software. All images were edited using the Microsoft Office Suite.

2.6.9.1 Data processing of XPS spectra

All the samples are analysed using CASAXPS™ software. Relative sensitive factors (RSF) were taken from the Kratos Library to correlate the experimental with the reported value. Peak areas were measured after

performing spline linear background subtraction appropriate for the shape of the spectrum. The estimated error in the relative atomic concentration of each element was taken to be between 10-20 % depending upon the signal to noise ratio.[13] Peak fitting areas for each element take into account spin orbit coupling and/or stoichiometry ratios. The full width at half maximum (FWHM) for all components in the C1s region are constrained to be between 0.8 and 1.2 eV. For compounds with a long alkyl chain ($n \geq 8$) charge reference was achieved by setting the experimentally determined aliphatic carbon component ($C_{alipahtic}$) to be equal to 285.0 eV which exhibits consistency in literature.[14,15] For compounds with short alkyl chain indirect charge reference is employed by setting the measured B.E. of the nitrogen photoemission peak equal to that for its long chain analogue. Hence, a reliable binding energy reference is obtained. The error in these binding energies is showed to be ±0.1 eV across a range of different ionic liquid standards.[13,15] Licence *et al.* in 10 years of experience in the field established a reliable C1s fitting model for imidazolium-based ILs[6] and pyridinium-based ILs.[15] A representative example is reported in Figure 2.11. The deconstructed envelope of C1s shows the presence of different electronic environment for the alkyl chain represented by C_4 at 285.10 eV which is collocated at lower binding energy, followed by C_3 the atom connected to the nitrogen, more electronegative atom, C_2 on the internal imidazolium ring connected also with the nitrogen and finally C_1 at 287.64 eV connected with two nitrogen atoms and left with an electron poor environment.

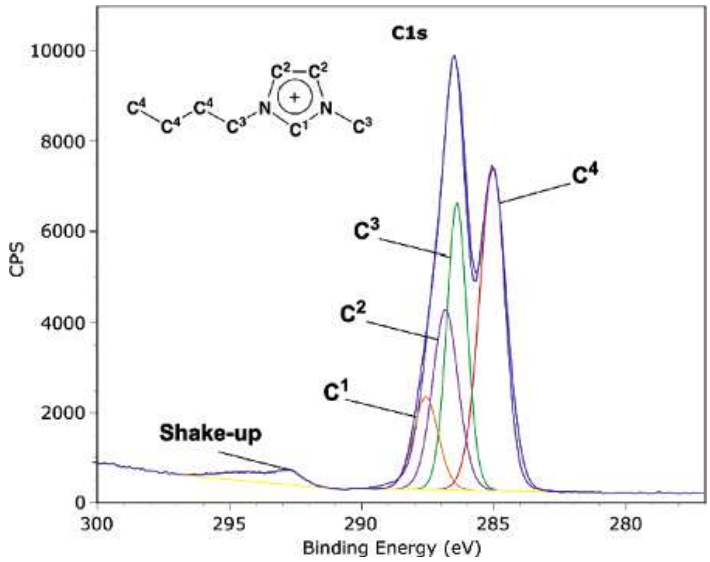


Figure 2.11 C1s XP spectrum of [C_4C_1Im][BF_4], detailing the C 1s photoemission. For all components a Gaussian-Lorentzian product function with 30% Lorentzian was applied with fwhm constrained to 0.9-1.1 eV.[7]

By contrast, the C1s fitting model for a pyridinium-based IL looks simplified. The deconstruction of the peak is represented by three peaks for three different electronic environments which correspond to the C_{hetero} bonded to the nitrogen atom, C_{inter} on the pyridinium ring and $C_{aliphatic}$ which might vary depends on the length of the chain. The Binding energy for these peaks are at around 287 eV, 286 eV and 285 eV for the C_{hetero}, C_{inter} and $C_{aliphatic}$, respectively.[15] The second attempt to study pyridinium ILs is reported more recently both in a single pyridinium and symmetric systems such as 4,4'-Bipyridinium.[16] It is very interesting to notice that again in this case a simple model has been proposed for the deconstruction of the C 1s envelope where three peaks are fitted for the $C_{2,6,7}$ $C_{3,5}$ and $C_{aliphatic}$ at ≈287 eV, ≈286 eV and 285 eV respectively. In order to examine the compounds presented in this report another important consideration, due to the presence of the benzene ring attached to the imidazolium ring is necessary. The literature reported a value which correspond to 284.00 eV for the curve which represents the aromatic carbons which is reported at lower B.E. compared to the aliphatic carbon.[17] Hence, several contributes held to the C1s fitting model that is presented in this report. A valid deconstructed envelopes is describes in order to describe the [$(C_8BzIm)_2Py$]Br_2 and [$(C_4BzIm)_2Py$]Br_2. electronic environments.

2.7 Summary

The experimental procedures used for the synthesis and characterisation of the NHCs compounds are presented in this chapter. The experimental procedures used for the synthesis and characterisation of the nanostructures of this project are also presented. XPS measurements allowed characterisation of the electronic structure of the NHCs compounds, we focused on the interactions between cation and anion and the characterisation of the new nanoparticle stabilised by NHCs. EDX was used to determine the chemical composition of the outer layer of NiNP stabilised by TOP or NHCs and to confirm the composition inside hollow graphitised nanofibres. TEM allowed the material characterisation of all of the samples prepared in this project. TGA allowed to determine the thermal stability of NHCs compounds and the oxidation temperature of NiNP. TGA was also used to determine the percentage of metal present in the organic layered nanoparticles and the amount of catalyst present in the graphitised nanofibres. NMR, GS-MS and CHN analysis have been used as routine analysis to characterise the purity and composition of all of the molecules synthesises in this thesis. Finally, electrochemical measurements determined the catalytic activity of the NiNP in GNF for the oxidation of propargyl alcohol.

2.8 Bibliography

1 T. Tu, W. Assenmacher, H. Peterlik, G. Schnakenburg and K. H. Dötz, *Angew. Chemie - Int. Ed.*, 2008, **47**, 7127–7131.

2 J. Park, E. Kang, S. U. Son, H. M. Park, M. K. Lee, J. Kim, K. W. Kim, H. J. Noh, J. H. Park, C. J. Bae, J. G. Park and T. Hyeon, *Adv. Mater.*, 2005, **17**, 429–434.

3 C. Kolbeck, N. Paape, T. Cremer, P. S. Schulz, F. Maier, H. P. Steinrück and P. Wasserscheid, *Chem. - A Eur. J. A Eur. J.*, 2010, **16**, 12083–12087.

4 H.-P. Steinrück, *Phys. Chem. Chem. Phys.*, 2012, **14**, 5010–29.

5 J. C. Vickerman and I. S. Gilmore, *Surface Analysis The Principal Techniques*, John Wiley & Sons Ltd., Chichester, 2009.

6 E. F. Smith, I. J. V. Garcia, D. Briggs and P. Licence, *Chem. Commun. (Camb).*, 2005, 5633–5635.

7 E. F. Smith, F. J. M. Rutten, I. J. Villar-garcia, D. Briggs and P. Licence, *Langmuir*, 2006, **22**, 9386–9392.

8 J. F. Watts and J. Wolstenholme, *An Introduction To Surface Analysis By XPS And AES*, John Wiley & Sons Ltd., Chichester, 2003.

9 Garratt-Reed and A. J, *Energy-Dispersive X-Ray Analysis in the Electron Microscope*, Oxford, BIOS scien., 2003.

10 B. Fultz and J. Howe, *Transmission Electron Microscopy and Diffractometry of Materials*, Berlin, Heidelberg, Springer., 2008.

11 M. T. Clough, K. Geyer, P. A. Hunt, J. Marters and T. Welton, *Phys. Chem. Chem. Phys.*, 2013, **15**, 20480–20495.

12 A. M. Bond, R. G. Compton, D. A. Fiedler, Š. K.-L. G. Inzelt, H. Kahlert and Z. S. c, H. Lohse, M. Lovri´ c, F. Marken, A. Neudeck, U. Retter, F. Scholz, *Electroanalytical Methods*, Greifswald, Germany, Fritx Scho., 2010.

13 I. J. Villar-garcia, E. F. Smith, A. W. Taylor, F. Qiu, K. R. J. Lovelock, R. G. Jones and P. Licence, *Phys. Chem. Chem. Phys.*, 2011, **13**, 2797–2808.

14 J. F. Moulder, W. F. Stickle, P. E. Sobol and K. D. Bomben, *Handbook of X-ray Photoelectron Spectroscopy*, 1992.

15 S. Men, D. S. Mitchell, K. R. J. Lovelock and P. Licence,

ChemPhysChem, 2015, **16**, 2211–2218.

16 C. Clarke, PhD Thesis, University of nottingham, 2015.

17 M. F. Delcroix, E. M. Zuyderhoff, M. J. Genet and C. C. Dupont-Gillain, *Surf. Interface Anal.*, 2012, **44**, 175–184.

Chapter 3

Synthesis and structural characterization of bis(benzimidazolin-2-ylidene) ionic structures

3.1 Introduction

Ionic liquids (ILs) possess negligible vapour pressure which make them the perfect candidates for Ultra High Vacuum (UVH) technique at room temperature.[1] The vast majority of the research on ILs has been devoted to the study of imidazolium-based ionic liquids. In 2005 It has been established the first fitting model for the C 1s region for $[C_2C_1Im][EtSO_4]$.[1] Since 2006 the literature has grown considerably and XPS has been used for the characterisation of ILs neat and mixed with solvents for catalytic applications.[2-4] ILs due to their properties find applications in sustainable chemistry and lately are designed to be environmental friendly.[5,6] Bis(benzimidazolin-2-ylidene) compounds, named later as pincer structures, represent a platform for synthesising ionic liquids derived from natural product.[7-9] The bis(benzimidazolin-2-ylidene) is a di-cationic symmetric molecule made of a pyridine ring connected in position 2 and 6 with two imidazolium alkylated rings. Despite of the examples of the papers which study geminal dicationic ionic liquids as lubricant or solvent for organic reaction.[10,11] Nothing has been done yet to develop dicationic ionic liquids with benign nature. Moreover, Bis(benzimidazolin-2-ylidene) compounds present a plane of symmetry which lays on the pyridine ring. Hence, the variation of the structure with long and short alkyl chain does not affect the centre of symmetry, which does not change. This chapter introduces the XPS spectra of di-cationic bis(benzimidazolin-2-ylidene) salts with Br^- $[BF_4]^-$ $[PF_6]^-$ $[NTf_2]^-$ counter ions. The C1s and N 1s spectra of structurally related cationic structures are compared in order to determine the effect of the anion on the cation and understand how it affects the electronic distribution. The charge transfer from anion to cation has been proved for both mono cation series ILs and dicationic ILs which have been found depending upon the basicity of the anion.[12,13] Moreover, It has been proved that the charge transfer of anion to cation in the case of dication ILs is consistent with the behaviour of monocation ILs. Hence the behaviour of Gemini ILs can be based upon previously studied monocations.[13]

3.2 Aim and objectives

The first aim of this section is to illustrate the reaction mechanisms of 2,6-bis(benzimidazolium)pyridine synthesis and the metathesis. The second

aim is to investigate the thermal stability and the decomposition temperature of the bis(benzimidazolin-2-ylidene) salts. It is crucial to investigate the thermal stability and the decomposition temperature of the bis(benzimidazolin-2-ylidene) as they are used as a stabiliser for the synthesis of nickel nanoparticles through thermal decomposition of nickel acetylacetonate-oleylamine complex.[14] The final aim of this chapter is to conduct a qualitative analysis of ionic systems based upon pincer structure using XPS. The study of gemini dications based upon the pyridine structure is still in its infancy. To achieve a complete understanding of these molecules further studies extended to a wider range of samples to give a more accurate and effective description are required. XPS is a reliable and powerful technique widely used to determine intermolecular interaction, the purity of ionic liquid substrate and the interaction between anion and cations. It is investigated the quantitative analysis of the elements present and shown the fitting model for the C_{1s} and N_{1s} photoemission peaks. The deconstruction of the carbon photoemission peak is the most important in this work and is based on fitting model previously investigated for the imidazolium ring and the pyridinium ring.[15,16] The pyridinium C1s fitting model is represented by the deconstruction in three component, C_{Hetero}, the carbons bound to the nitrogen atoms, C_{Inter}, the remaining carbon atoms in the ring and $C_{Aliphatic}$ which contains the carbon of the alkyl chain, Figure 3.1.[16] The Imidazolium-based ILs fitting model present four components, C_2, the carbon bonded with two atoms of nitrogen, C_{4+5}, the remaining carbon atoms in the ring and $C_{Aliphatic}$ which contain, as for the pyridinium ring, the carbon of the alkyl chain, Figure 3.1.[15]

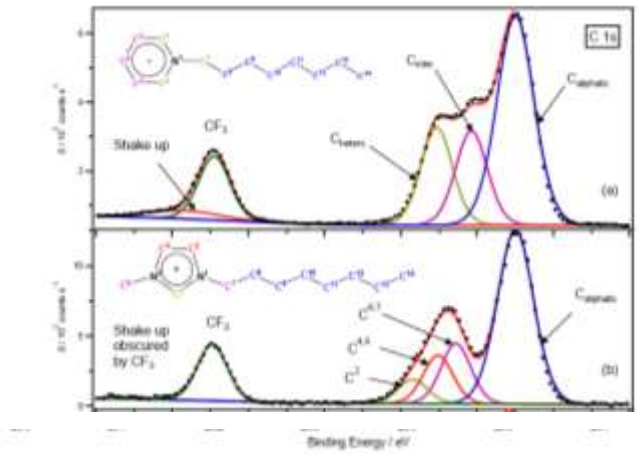


Figure 3.1 Fitting model of C1s for [C_8Py][Nf_2] and [C_8C_1Im][NTf_2]; [C_8Py][NTf_2] with labelled structure: C_{hetero} (yellow), C_{inter} (mauve) and $C_{aliphatic}$ (blue). *[C_8C_1Im][NTf_2] with labelled structure:* C_2 (yellow), C_{4+5} (red), C_{6+7} (mauve) and $C_{aliphatic}$ (blue). The XP spectrum is charge corrected by referencing the $C_{aliphatic}$ 1s component to 285.0 eV.[12]

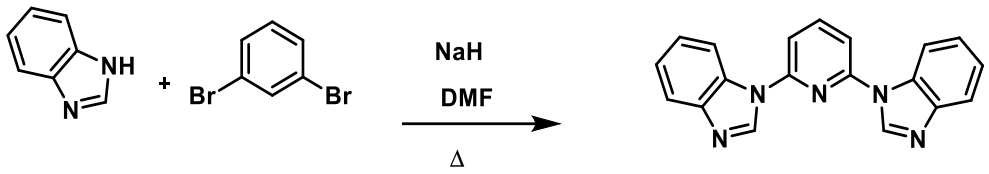
Also they have been lately studied in Gemini ILs made of two rings connected by an alkyl chain in structures such as 4,4'-bipyridinium ILs.[13,17] The aim of this study is to analyse 2,6-bis(benzimidazolium)pyridine compounds to define a reliable fitting model and address several questions, the most important is *"Do the Pyridinium-based ILs and Imidazolium-based ILs fitting model represent the C 1s fitting model for 2,6-bis(benzimidazolium)pyridine dicationic molecules?" An XPS analysis of 2,6-bis(benzimidazolium)pyridine salts provides a reliable model for any future XPS experiments involving similar cations and, based upon the known use of NHCs in catalysis, on metal-ILs interactions.*[18]

3.3 Ligand synthesis

3.3.1 2,6-Bis(benzimidazole)pyridine, [2,6-bis(BzIm)$_2$Py]

The reaction conditions for the synthesis of 2,6-bis(benzimidazole)pyridine are adapted from existing literature procedure.[8] The reaction yields an air stable white powder in a 65 % yield (Scheme 3.1). The modest yield is

associated to a moderate reactivity of the substrate to the nucleophile (the benzimidazolium).



Scheme 3.1 Synthesis of 2,6-Bis(benzimidazole)pyridine.

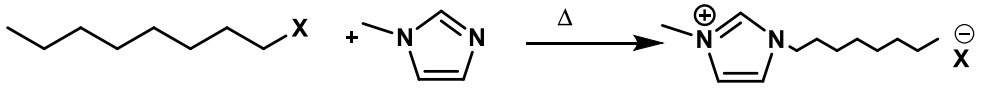
The strong base, NaH, removes the acidic proton of the benzimidazole which is left stirring for about one hour. Then, the 2,6-bisbromopyridine is added to generate an aromatic substitution. The sodium hydride was a good base for the deprotonation, Scheme 3.1. However, it was crucial to avoid the presence of water as even tiny amount of it could generate an extremely exothermic reaction. The activation of the nitrogen allowed the formation of a nucleophilic species, which could attack the aromatic ring in positions 2 and 6 to give aromatic substitution.

The same reaction is reported with 2,6-bisdichloropyridine achieving an extremely bright precipitate with 63 % of yield. The reaction conditions are strongly influenced by the alkyl halide used. Indeed, chloro halide requires longer reaction time and higher temperature than the bromide halide. The behaviour of the different halides is influenced by the correspondent position of the halogens in the group of the periodic table (chlorine is above bromine in group 7). The S_N2 reaction rate changes in combination with the strength of the carbon-halogen bond stability. The reason for this is that when the halogen electronegativity is lower, the size of the halogen is bigger and the strength of the bond drops.

The lower yield can be associated to an enhancement of this different behaviour of the halides. An important aspect is the solvent used for this reaction, in this case DMF, which due to its high boiling point is very difficult to eliminate. However, the addition of water allows to remove the solvent residual followed by recrystallization which is described further in the section 2.3.

3.3.2 Alkylation reaction of ligand structures

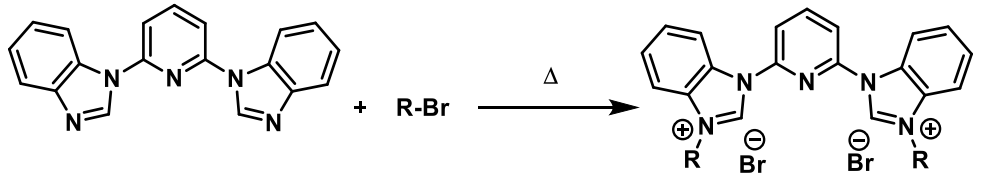
The alkylation of 1-methylimidazole to obtain a 1-alkyl-3-methylimidazolium salt [C_nC_1Im] [X^-] is presented in Scheme 3.2. Some of the alkylating agents are chloro, bromo or iodo alkane.



X = Cl, Br, I

Scheme 3.2 Alkylation of 1-methylimidazole with different halogenoalkanes.

In this work the imidazolium is inserted in a more complex structure. Three types of structures have been synthesised with different length chain and similar experimental procedure, Scheme 3.3.



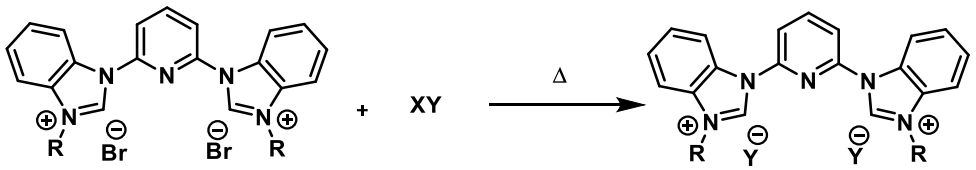
R=$CH_3(CH_2)_2CH_2$
R=$CH_3(CH_2)_6CH_2$
R=$CH_3(CH_2)_{10}CH_2$

Scheme 3.3 alkylation of bis(benzimidazolin-2-ylidene) structures.

The reactions are completed with dry DMSO under an inert atmosphere for 48-72 hours. The product of alkylation requires extreme care into the purification step. In fact, the products are wisely recrystallised three times to ensure the elimination of the starting material. The reactions yielded 97-98 % in every case, further details are reported in Chapter 2.

3.3.3 Anionic exchange reactions

The ionic compounds are further reacted with tetrafluoroboric acid, hexafluorophosphoric acid and bis(trifluoromethylsulfonyl)imide to exchange the halide anion with a polyatomic anion in a metathesis reaction. A metathesis reactions generally uses water as solvent and it is kept stirring for 24 hours. However, in this case the starting material is dissolved in both water and DCM, Scheme 3.4.



Scheme 3.4 metathesis reaction.

The solvent is a mixture 1:2=DCM:H_2O. The hydrophobic ILs are dissolved in DCM medium and partially in water. On the contrary, the salts used for the metathesis are dissolved in water. After metathesis, the reaction mixture contains hydrophobic ILs, which are not miscible in water. By contrast, they can be extracted with an organic solvent, XPS analysis ensure that the purity of the anion with regards to residual bromide contamination.

3.4 Thermogravimetric studies

The thermogravimetric study determines the decomposition temperature of the samples. The first two TGA profiles discussed are of $[(C_8BzIm)_2Py]$ Br_2 and $[(C_4BzIm)_2Py]Br_2$ respectively, Table 3.1. The samples with an alkyl chain attached to the benzimidazolium show a decomposition profile with multiple decomposition steps which is consistent with the literature of benzimidazole based compounds.[19] Conversely, the samples containing the other anions show a single step decomposition. The value of T_i,T_f and T_p are reported in Table 3.1. The results are consistent with the literature in which the thermal stability is closely related to the alkyl chain length.[20] In addition, the decomposition temperature could change from 300 ºC to 400 ºC by varying anion type, which indicates that anions plays a crucial role in determining thermal stability.

The weight percentages losses show a consistent drop associated with the increasing temperature in both cases. The onset peaks are at 227 °C and 249 °C with weight loss around 2 % for $[(C_8BzIm)_2Py]Br_2$ and $[(C_4BzIm)_2Py]Br_2$ respectively, associated to moisture loss as was previously reported.[21] The (T_p) temperature associated with the first

derivative for the long alkyl chain compound is at 375 °C with a weight loss of ≈ 27.4 %. Conversely, the temperature associated with the first derivative for the short alkyl chain compound is at 381 °C with a weight loss of ≈ 80 %, Table 3.1. [19] Again, the chain length of molecules with similar cation affects the thermal stability of the compounds. There are two effects which contributes to the lower thermal stability of $[(C_8BzIm)_2Py]Br_2$ compared to $[(C_4BzIm)_2Py]Br_2$. Firstly, a longer chain results in greater van der Waals forces. Moreover, the intermolecular electrostatic interaction decreases leading to lower thermal stability. Secondly, longer alkyl chain is associated to the formation of carbocation and carbon radicals more stable therefore the thermal decomposition takes place more easily.[20]

The percentages calculated show that the chain represents the weakest part of the molecule, which is presumably the first to be decomposed. The remaining 20 % left is ascribed to the remaining part of the skeleton of $[(C_8BzIm)_2Py]Br_2$ and $[(C_4BzIm)_2Py]Br_2$ shown in Table 3.1.

The second set of data compare all the $[(C_8BzIm)_2Py][BF_4]_2$ $[(C_8BzIm)_2Py][PF_6]_2$ samples, Figure 3.2.

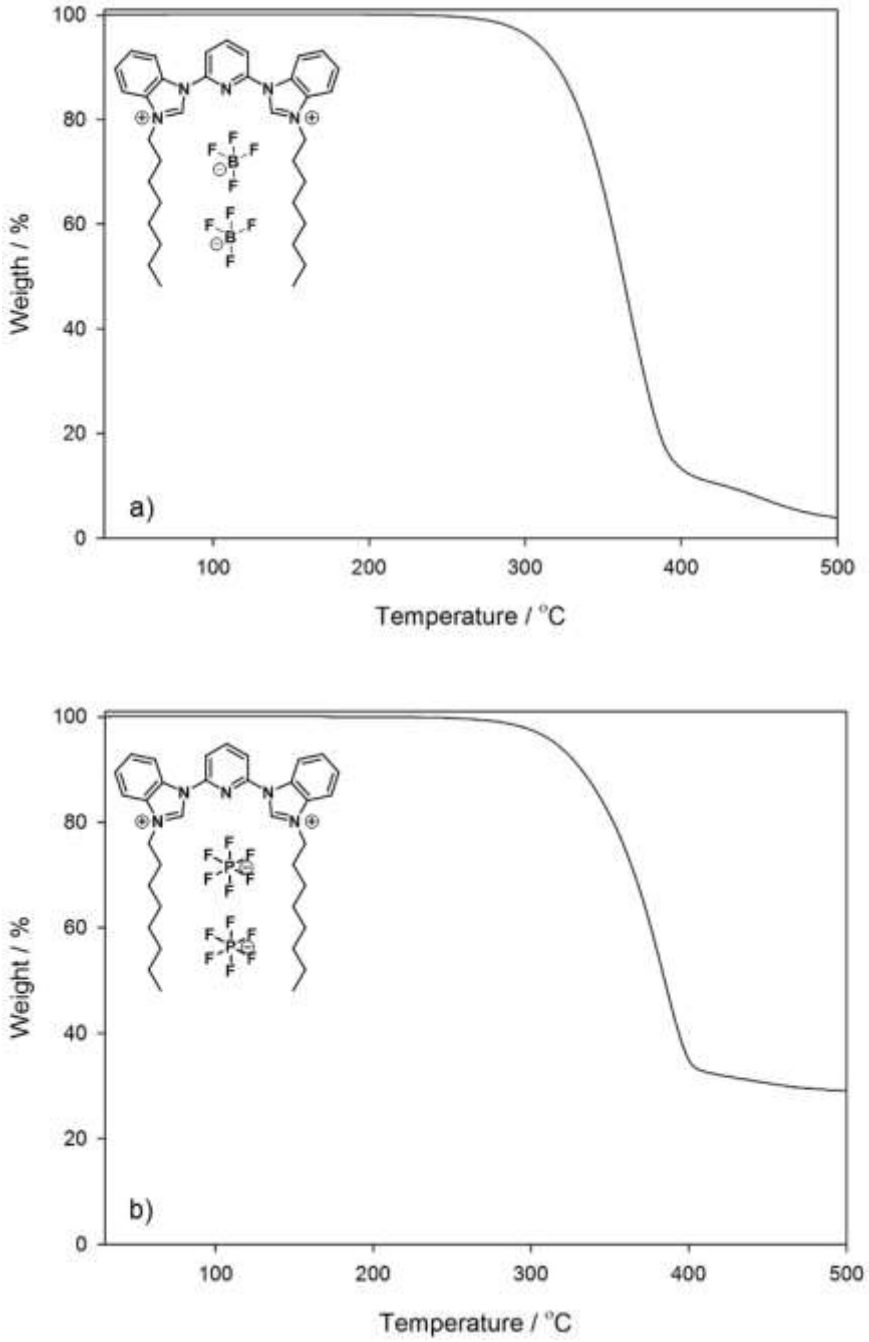


Figure 3.2 TGA of a) [(C_8BzIm)$_2$Py][BF_4]$_2$ and b) [(C_8BzIm)$_2$Py][PF_6]$_2$ of y in weight percentage and x in Celsius degree carried out under nitrogen atmosphere.

The presence of different anions considerably changes the shape of the curve. The weight losses are consistent for different samples with the same

cation but different anions, Figure 3.3, suggesting a correlation with the anion type.

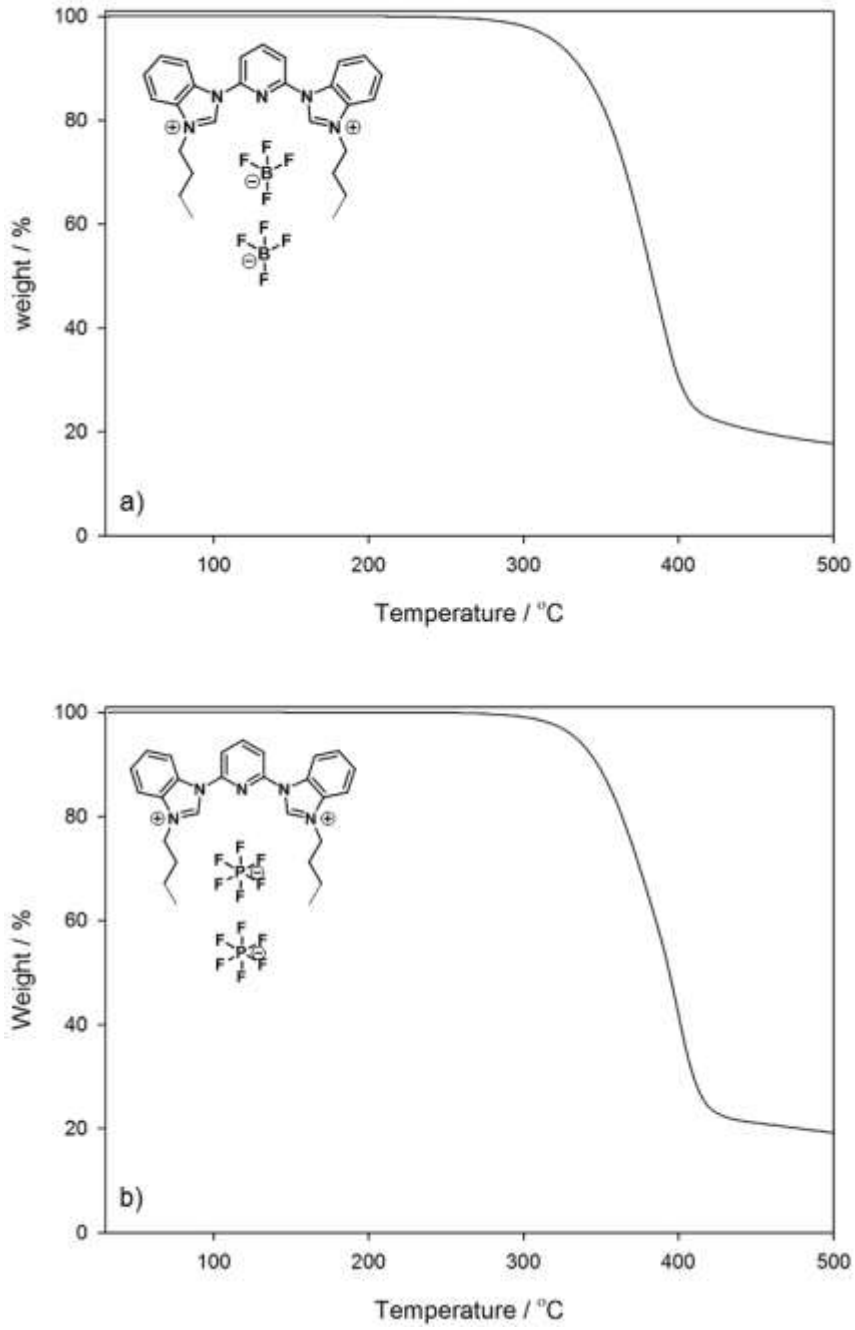


Figure 3.3 TGA of a) [(C₄BzIm)₂Py][BF₄]₂ and b) [(C₄BzIm)₂Py][PF₆]₂ of y in weight percentage and x in Celsius degree carried out under nitrogen atmosphere.

As previously shown, the chain length influences the thermal stability with different cations and different anions. The percentages calculated show that the chain represents the weakest part of the molecule, which is presumably the first to be decomposed. The onset peaks are at 245 °C and 284 °C with weight loss around 2 % for $[(C_8BzIm)_2Py][BF_4]_2$ and $[(C_8BzIm)_2Py][PF_6]_2$ respectively, at 301 °C and 326 °C with weight loss around 2 % for $[(C_4BzIm)_2Py][BF_4]_2$ and $[(C_4BzIm)_2Py][PF_6]_2$ respectively, which are associated to moisture loss.[21]

The (T_p) temperature associated with the first derivative for the long chain compound with $[BF_4]$ is at 367 °C with a weight loss of the 56 %, Table 3.1. Conversely, temperature associated with the first derivative for the short chain with $[PF_6]$ is at 384 °C with loss weight of 49 %, Table 3.1. The anions plays an relevant effect in the thermal stability ionic compounds. The anion can be ordered from the lowest stability as follow:

$$Br^- < [BF_4]^- < [PF_6]^-$$

Hence, the results are consistent with the literature taking into account the different length chain and the different anion.[20] The results confirm that the decomposition temperature is proportional to the nucleophilicity of the anion.

Table 3.1 Measured values of T_i (procedural decomposition temperature, peak onset), T_f (final temperature), T_p (temperature associated with the first derivative) in which the greatest rate of change of the slope in the weight loss profile which correspond and the Weight at T_p (%).

Sample	$T_{i,1}$ (ºC)	$T_{f,2}$ (ºC)	$T_{f,3}$ (ºC)	Weight (%)	T_p (ºC)	Weight at T_p (%)
$[(C_8BzIm)_2Py][Br]_2$	227			99	375	73
		246		96		
			391	71		
$[(C_8BzIm)_2Py][BF_4]_2$	245			96	367	44
		390		17		
$[(C_8BzIm)_2Py][PF_6]_2$	284			99	384	51

		411		33		
$[(C_4BzIm)_2Py][Br]_2$	249			98	381	12
		281		74		
			398	2		
$[(C_4BzIm)_2Py][BF_4]_2$	301			98	383	50
			419	23		
$[(C_4BzIm)_2Py][PF_6]_2$	326			97	400	41
			440	21		

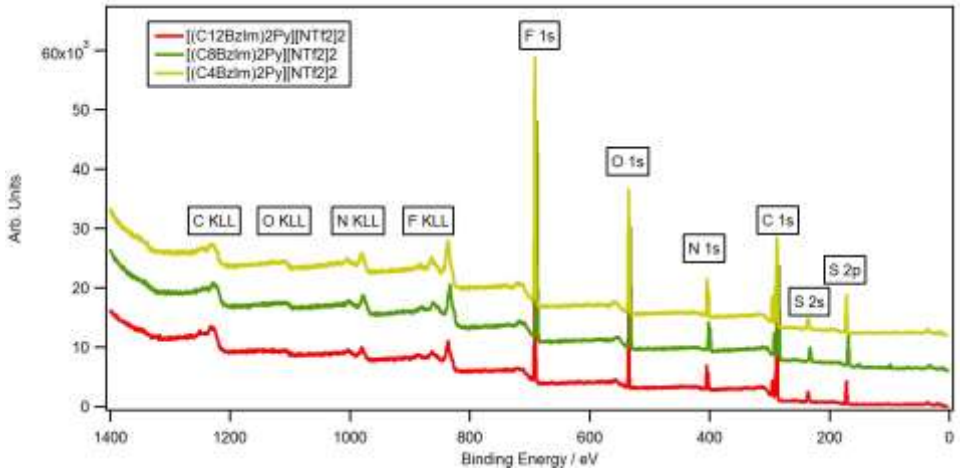
3.5 X-ray Photoemission Spectroscopy of bis(benzimidazolin-2-ylidene) salts

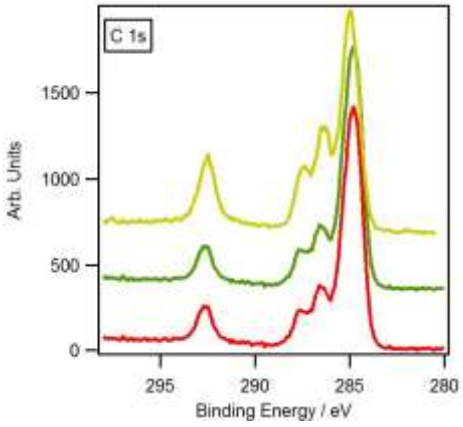
The structural complexity of bis(benzimadazolin-2-ylidene) salt is yet to be fully described in the literature, hence there is an urgent need to investigate the structural composition of the salt at molecular level using XPS. As all the ionic liquids, these salts, because are made of ions, possess negligible vapour pressure and do not evaporate, even under high vacuum.[22,23] XPS which requires high vacuum to operate as previously described in chapter 2, provides chemical information such as chemical state identification, surface composition, and valence band structure.[24,25] These chemical information contribute to the understanding of the molecules especially for catalytic applications and for the interfacial area surrounding ionic liquids.[26] The symmetric structure of bis(benzimidazolin-2-ylidene) molecules can be compared to the simplest structures which constitute the skeleton, a pyridine connected to two alkylated imidazolium rings.[16] In this section is detailed the C1s fitting model and the N1s fitting model. Moreover, it is studied the effect of the anion on the cation in comparison with other molecules reported in the literature.[12]

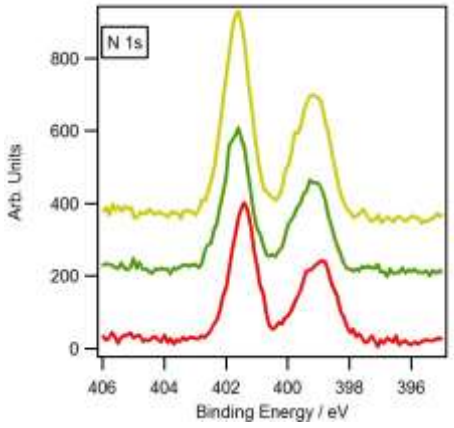
3.5.1 Wide and high resolution scan

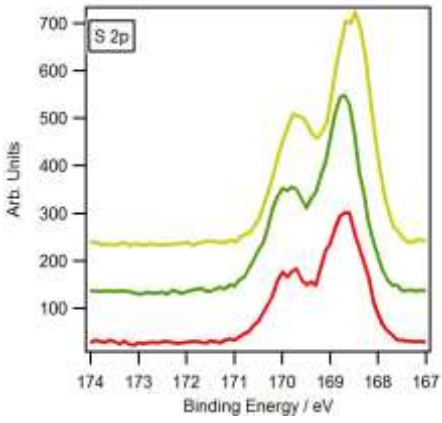
A wide scan or survey is an analysis of all the possible emission energies in XPS. In this work has been used the Al monochromatic X-Ray source (Al Kα X-rays, E=1486.7 eV) with a correspondent a large energy range between 1400 to 0 eV. The scan limit is set up to 1400 eV which correspond to the maximum energy at which are found photoelectron transitions. The survey of a sample is recorded with a pass energy of 80 eV and allows the detection of all the elements present in the sample with detection limit of 0.1 atomic %, making the technique a veritable quantitative analytical tool. Also, the survey allows a first qualitative analysis to check the purity of the samples in the case some traces of contaminants are not detectable with other analytical techniques.[6]

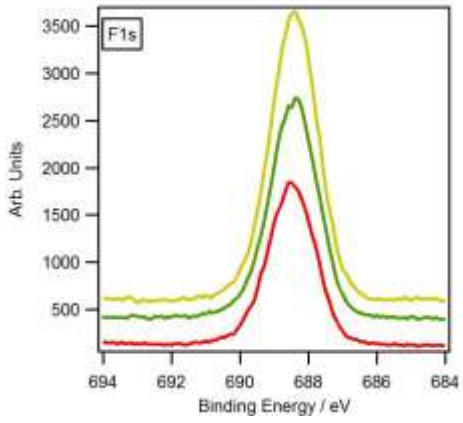
Herein, a representative example of wide scan for each alkyl chain analogue of $[(C_nBzIm)_2Py][NTf_2]_2$ is given in Figure 3.4, as the case of all the samples analysed in this work. The scans are offset for presentation purpose. All the samples reported in this chapter present high purity and no cross-contaminants affected the XPS measurements. Only expected photoemission peaks are observed for $[(C_nBzIm)_2Py][NTf_2]_2$ and labelled as follow: F1s 688.4 eV, O 1s 532.3 eV, N 1s 401.4 eV, C 1s 285.0 eV, S 2p 257.0 eV, Figure 3.4. The data show a good agreement with the values obtained in the literature for the elements.[27, 16]


[(C12BzIm)2Py][NTf2]2
[(C8BzIm)2Py][NTf2]2
[(C4BzIm)2Py][NTf2]2
60x10³
Arb. Units
C KLL
O KLL
N KLL
F KLL
F 1s
O 1s
N 1s
C 1s
S 2p
S 2s
Binding Energy / eV


C 1s
Arb. Units
Binding Energy / eV


N 1s
Arb. Units
Binding Energy / eV


S 2p
Arb. Units
Binding Energy / eV


F1s
Arb. Units
Binding Energy / eV

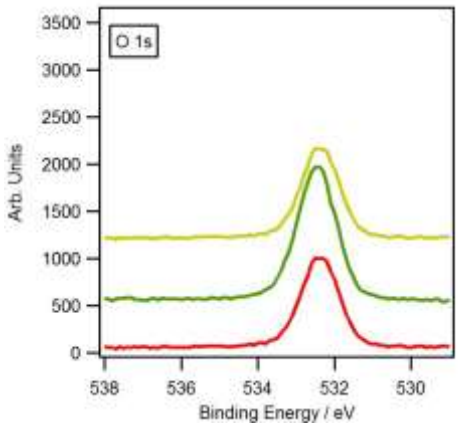


Figure 3.4 Survey scan and high resolution scans for $[(CnBzIm)_2Py][NTf_2]_2$ where n=12 (red), n=8 (green) and n=4 (yellow). The spectra are charge corrected to the C1s C_{ali} component for n ≥ 8, set to 285.0 eV. The corresponding value for the N1s signal is then used to reference n=4 as indirect charge reference.

The high-resolution scan is zoomed on a small region of the spectra and typically is focused on a photoelectron transition, Figure 3.4. The high resolution scan is run with a pass energy of 20 eV. The acquisition time depends upon the concentration and sensitivity of the element measured. High resolution spectra are used for chemical state identification and semi-quantitative analysis. The quantitative analysis is based on the area below the peak signal of the most representative photoelectrons for each element. For data interpretation, Spline linear background subtraction is used depending on the shape of the spectra. Relative Sensitive Factors (RSF) are taken from the Kratos Library and are used to determine relative atomic percentages of the most intense photoelectron peak for each element from high resolution spectra.[28] Peaks are fitted consistently using GL (30) line shapes a combination of Gaussian (70%) and Lorentzian (30%). The full width at half maximum (FWHM) and peak area are constrained during the peak fitting. The shake-up/off is taken into account when constraining the area of the fitted peak, discussed in more details later. The Full Width at Half Maximum (FWHM) of each component is constrained to 0.9 ≤ FWHM ≤ 1.3 eV. Peak area of each elements take into account stoichiometry ratio and spin coupling.

The percentage elemental compositions for each element are reported in Table 3.2. The deviation % of the experimental value from the nominal value deviation is reported in bracket in Table 3.2, as |Experimental value - Nominal value| / (Experimental value + Nominal value) ·100.

Table 3.2 Percentage elemental composition of the samples investigated with XPS and deviation % in bracket as |Experimental value-Nominal value| / (Experimental value+Nominal value) ·100. In brackets are reported the estimated error in the relative atomic concentrations of each element.

Compound	C %	N %	Br %	F %	B %	P %	S%	O%
$[(C_{12}BzIm)_2Py]Br_2$								
Nominal	91.5	4.2	4.2	-	-	-	-	-
Experimental	86.5 (2.8)	6.3 (11.2)	5.2 (9.9)	-	-	-	-	-
$[(C_{12}BzIm)_2Py][Ntf_2]_2$								
Nominal	60.3	8.9	-	15.4	-	-	5.1	10.3
Experimental	62.4 (1.7)	8.5 (2.4)	-	15.0 (1.2)	-	-	5.3 (1.8)	8.7 (7.9)
$[(C_8BzIm)_2Py]Br_2$								
Nominal	83.3	11.9	4.8	-	-	-		
Experimental	84.5 (0.7)	9.0 (13.8)	5.4 (6.3)	-	-	-		
$[(C_8BzIm)_2Py][BF_4]_2$								
Nominal	70	10	-	16	4	-		
Experimental	76.2 (4.2)	10.1 (0.5)	-	12.3 (10.6)	3.2 (10.6)	-		
$[(C_8BzIm)_2Py][PF_6]_2$								
Nominal	64.8	9.2	-	22.2	-	3.7		
Experimental	73.2 (6.1)	7.1 (13.0)	-	15.2 (18.8)	-	4.9 (14.1)		
$[(C_8BzIm)_2Py][Ntf_2]_2$								
Nominal	55.7	10	-	17.1	-	-	6.4	12.9
Experimental	56.9 (1.0)	8.9 (5.6)	-	18.2 (3.0)	-	-	6.2 (2.0)	10.2 (11.7)
$[(C_4BzIm)_2Py]Br_2$								
Nominal	79.4	5.9	5.5	-	-	-	-	-
Experimental	82.9 (2.2)	6.2 (2.9)	5.8 (2.5)	-	-	-	-	-
$[(C_4BzIm)_2Py][BF_4]_2$								
Nominal	64.3	11.9	-	19.1	4.8	-		
Experimental	64.3 (0)	10.4 (6.6)	-	19.5 (1.1)	5.8 (10.1)	-		
$[(C_4BzIm)_2Py][PF_6]_2$								
Nominal	58.7	10.9	-	26.1	-	4.3		
Experimental	56.3 (2.1)	10.2 (3.2)	-	26.3 (0.4)	-	4.2 (1.2)		
$[(C_4BzIm)_2Py][Ntf_2]_2$								
Nominal	50	11.3	-	19.3	-	-	6.4	12.9
Experimental	50.8 (0.8)	10.0 (5.9)	-	20.2 (2.2)	-	-	7.2 (5.3)	11.8 (4.5)

The values for elemental compositions are in good agreement with the expected values. Most values do not deviate more than 5 % of the

expected values. The estimated error in the relative atomic concentrations of each element is considered between 10 and 20 % depending on signal to noise ratio.[2]

Finally, Table 3.3 shows binding energy values for all regions and components for all ionic liquids investigated in this study. The values of the correspondent B.E. for each component fitted for each photoemission peaks envelope related to each elements present in the samples are consistent with the literature.[29, 16]

The N 1s signal shows two resolved peaks that represent the nitrogen from the imidazolium ring (at higher B.E.) and the nitrogen from the pyridine ring which is overlapped with the nitrogen from the anion (at lower B.E.). These two signals integrate to give a ratio area 4:3, as expected. All scans show consistency in their photoemission peak positions which supports the charge correction applied explained in more details in section 3.5.2.

Table 3.3 Binding energy / eV of the components fitted for each photoemission peak envelope related to each element present in the samples.

Binding energy / eV

The experimental error associated with the measurement of binding energy is ± 0.1 eV

Compounds		Cation							Anion					
Cation	**Anion**	**$C_{aromatic}$ 1s**	**C_{ali} / C_{alkyl} 1s**	**C_{C-N} 1s**	**C_{N-C-N} 1s**	**C_{CF3} 1s**	**N_{py} 1s**	**N_{Im} 1s**	**F 1s**	**P $2p_{3/2}$**	**B 1s**	**Br $3d_{5/2}$**	**O 1s**	**S $2p_{3/2}$**
$[(C_{12}BzIm)_2Py]^{2+}$	$2[Br]^-$	284.4	285.0	285.8	286.7	-	399.2	401.2	-	-	-	66.8	-	-
$[(C_{12}BzIm)_2Py]^{2+}$	$2[Ntf_2]^-$	284.6	285.0	286.6	287.7	292.7	399.3	401.2	688.5	-	-	-	532.4	168.7
$[(C_8BzIm)_2Py]^{2+}$	$2[Br]^-$	284.6	285.0	286.3	287.4	-	399.5	401.2	-	-	-	67.3	-	-
$[(C_8BzIm)_2Py]^{2+}$	$2[BF_4]^-$	284.7	285.0	286.5	287.6	-	399.7	401.3	685.6	-	193.9	-	-	-
$[(C_8BzIm)_2Py]^{2+}$	$2[PF_6]^-$	284.1	285.0	286.2	287.3	-	399.4	401.4	686.1	136.3	-	-	-	-
$[(C_8BzIm)_2Py]^{2+}$	$2[Ntf_2]^-$	284.4	285.0	286.5	287.6	292.5	399.2	401.6	688.4	-	-	-	532.3	168.5
$[(C_4BzIm)_2Py]^{2+}$	$2[Br]^-$	285.3	285.6	286.7	287.8	-	400.0	401.9	-	-	-	67.6	-	-
$[(C_4BzIm)_2Py]^{2+}$	$2[BF_4]^-$	284.8	285.4	286.5	287.5		399.7	401.7	685.8	-	193.8	-	-	-
$[(C_4BzIm)_2Py]^{2+}$	$2[PF_6]^-$	284.7	284.9	286.3	287.4	-	399.5	401.5	686.1	136.2	-	-	-	-
$[(C_4BzIm)_2Py]^{2+}$	$2[Ntf_2]^-$	284.9	285.1	286.5	287.6	292.5	399.2	401.6	688.4	-	-	-	532.2	168.5

3.5.2 Peak fitting the $[(C_8BzIm)_2Py]X_2$ C 1s region

The first compound under study is a dicationic species, which presents a symmetric structure with a central pyridine ring functionalised in position 2 and 6 with two benzimidazolium rings with two alkyl chains of 8 carbons, Figure 3.5. This is a unique opportunity with XPS to investigate this particular type of symmetric structure particularly considering the C1s photoemission peaks, where the symmetric plane lays on the pyridine ring, Figure 3.5.

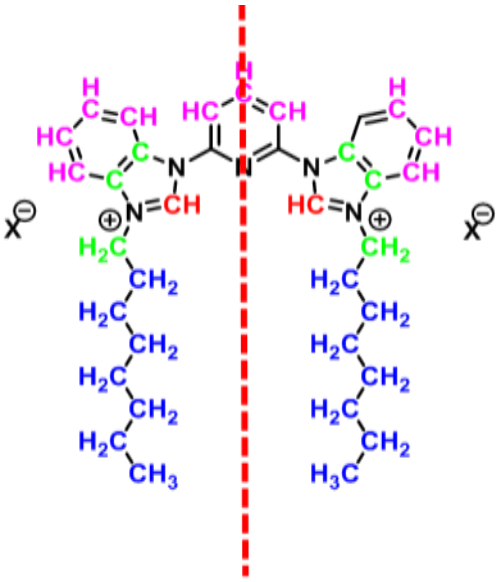


Figure 3.5 Representation of the symmetric structure for $[(C_8BzIm)_2Py]X_2$. The colours represent carbon environments C_{Ar} (pink), C_{ali} (blue) $C_{C\text{-}N}$ (green), $C_{N\text{-}C\text{-}N}$ (red).

The fitting is based upon data collected for all families of ionic liquids whether long alkyl chains are present or not. The deconstruction of the measured C1s photoemission envelope is achieved by applying a suitable multi-component model to describe the different carbon environment.[16] In the deconstructed photo electronic peak of $[(C_8BzIm)_2Py]Br_2$ given in Figure 3.6 a), C_{Ar} is fitted to the shoulder in the envelope with the lowest binding energy and corresponds to 284.6 eV. C_{Ali} represents the peak at 285.0 eV that is assigned according to the literature.[27] Hence, it represents a reliable binding energy reference for charge calibration. $C_{N\text{-}C\text{-}N}$ indicates the carbon bonded to two electronegative atoms on the imidazolium ring where the positive charge is delocalized among three carbon atoms. $C_{C\text{-}N}$ represents carbon atoms directly bonded to the nitrogen, which are the most electronegative atoms in the imidazolium ring and pyridine ring respectively.

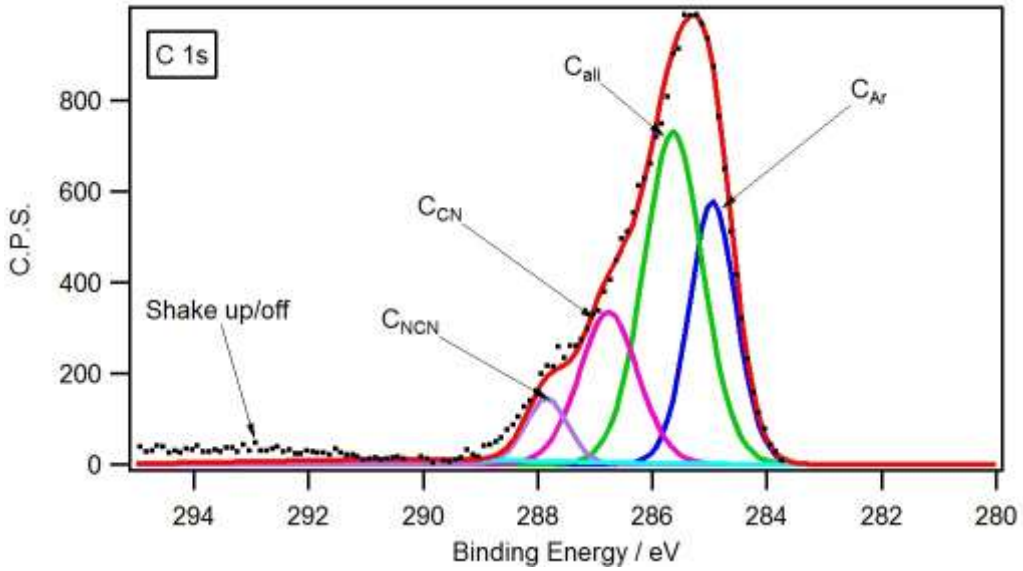


Figure 3.6 Fitting model of C1s for [$(C_8BzIm)_2Py$]Br_2 fitted with the component assignments shown on the appended structure which corresponds to different chemical environments.

The relative peak areas for the three cationic components in the [$(C_8BzIm)_2Py$][$Br]_2$ would be expected to be of the order 1 : 4 : 7 : 5.5 for $C_{N\text{-}C\text{-}N}$: $C_{C\text{-}N}$: C_{Ali} : C_{Ar}. The samples show the presence of shake-up/off phenomenon. However, to compensate for the shake-up/off phenomenon, which affects 5-20% of all photoemissions originating from resonance structure either in the case of imidazolium or pyridine rings. It results in the loss of kinetic energy for some photoelectrons with a resultant shift to a higher binding energy.[30] The observation of a shake-up satellite is due to the π-π* excitation of a valence electron after the photoemission involved in multiple bonding and aromatic compounds. By contrast the shake-off effect involves the ionisation of the valence electrons and the loss of kinetic electron of the photoelectron and contributes to the baseline.[31] The total component area for the three carbon atoms affected, $C_{N\text{-}C\text{-}N}$ and $C_{C\text{-}N}$ is reduced by 20%. However, the peak for the C_{Ali} which is outside the ring is not affected and is assigned complete values. The relative peak area for the cationic carbon can now be set as 1 : 3.2 : 7 : 4.4 for $C_{N\text{-}C\text{-}N}$: $C_{C\text{-}N}$: C_{Ali} : C_{Ar}.

The fitting process is applicable for the analogues samples of [$(C_8BzIm)_2Py$][$Br]_2$, [$(C_8BzIm)_2Py$][$BF_4]_2$, [$(C_8BzIm)_2Py$][$PF_6]_2$ and [$(C_8BzIm)_2Py$][$Ntf_2]_2$ with the corrected value for C_{Ali}, which present similar deconstructed envelope, Figure 3.7, Figure 3.8 and Figure 3.9.

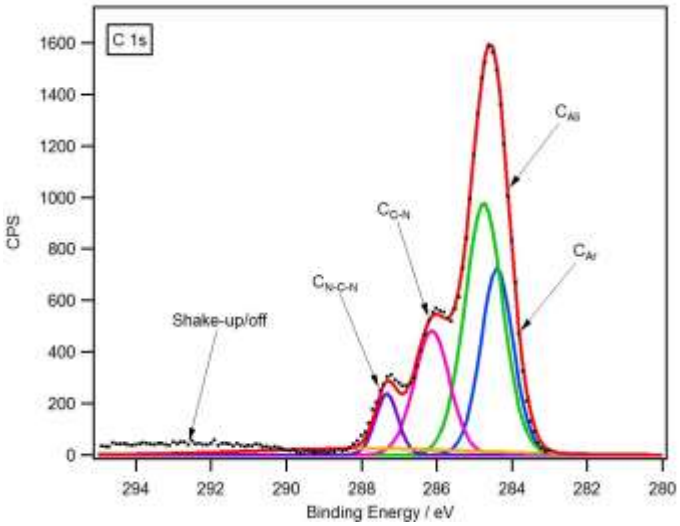


Figure 3.7 Fitting model of C1s for $[(C_8BzIm)_2Py][BF_4]_2$ fitted with the component assignments shown on the appended structure which corresponds to different chemical environments.

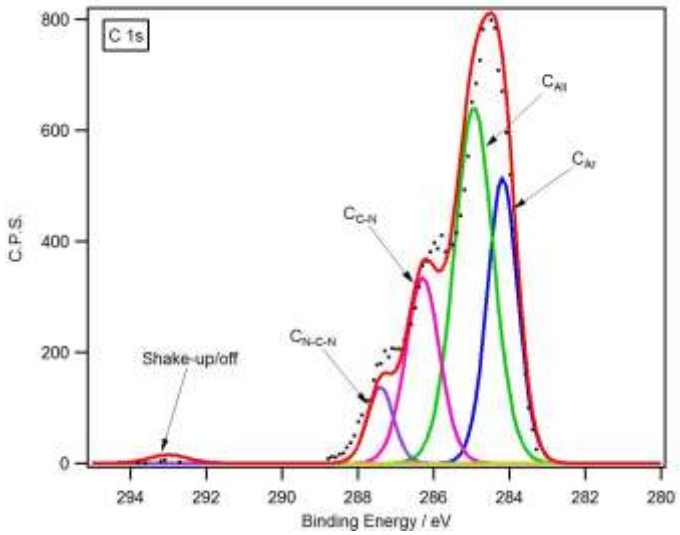


Figure 3.8 Fitting model of C1s for $[(C_8BzIm)_2Py][PF_6]_2$ fitted with the component assignments shown on the appended structure which corresponds to different chemical environments.

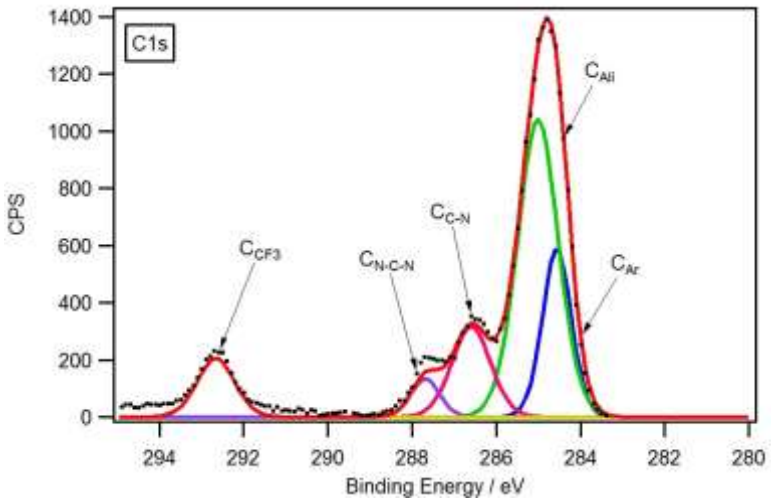


Figure 3.9 Fitting model of C1s for $[(C_8BzIm)_2Py][Ntf_2]_2$ fitted with the component assignments shown on the appended structure which corresponds to different chemical environments.

3.5.3 Peak fitting the $[(C_nBzIm)_2Py][NTf_2]_2$ C 1s region

The peak fitting model of the $[(C_8BzIm)_2Py][NTf_2]_2$ C 1s is shown in Figure 3.9. The component under the photoemission peaks observed for $[(C_8BzIm)_2Py][NTf_2]_2$ are labelled as follow: C_{CF3} 292.5 eV, C_{N-C-N} 287.6 eV, C_{C-N} 286.5 eV, C_{Ali} 285 eV and C_{Ar} 284.4 eV, Table 3.3. By varying the alkyl chain of the cation is possible to confirm the position of the components assigned shown on the appended structure which corresponds to different chemical environments. The resulting carbon environment groups for the $[(C_nBzIm)_2Py][NTf_2]_2$ is represented in Figure 3.10.

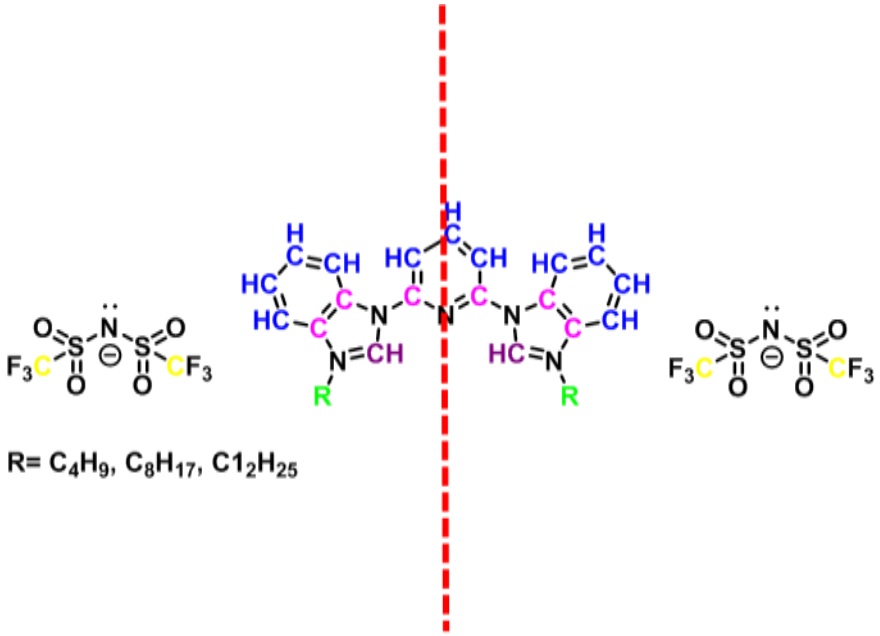


Figure 3.10 The structure of the $[(C_nBzIm)_2Py][NTf_2]_2$ dication with colour coded carbon environments: C_{CF3} (yellow), C_{N-C-N} (violet), C_{C-N} (pink), C_{Ali} (green) and C_{Ar} (blue).

The B.E. values acquired from the peak fitting of the $[(C_nBzIm)_2Py][NTf_2]_2$ C 1s regions are shown in Figure 3.11. The only significant changes in the overlapped graphs are the component associated to the aliphatic carbon chains.

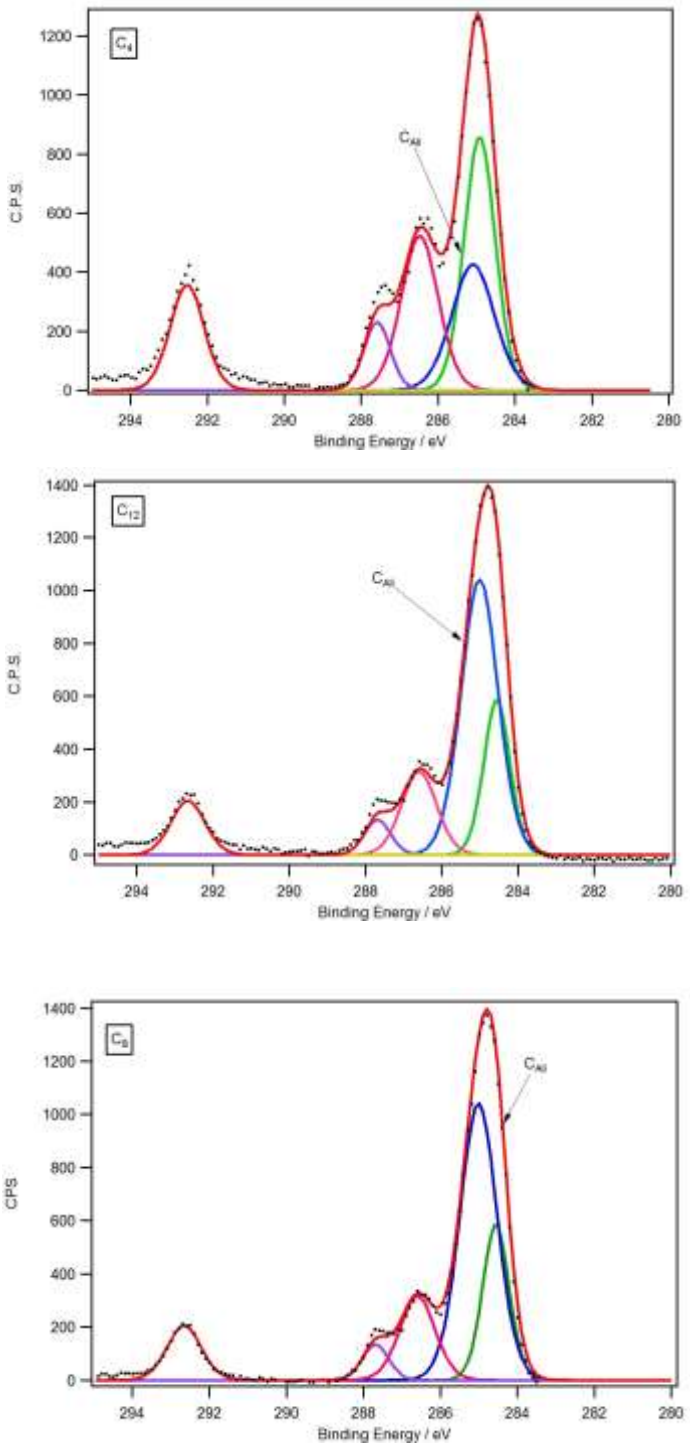


Figure 3.11 The peak fitted C 1s region of the [(C_nBzIm)$_2$Py][NTf_2]$_2$ salts. The aliphatic component is highlighted for the C_4, C_8 and C_{12}.

3.5.4 Effect of the anion on the cation

The samples reported in this section have the same cation but different anions. The cation-anion interaction investigated so far by XPS shows the influence of the basicity of the anion on the event of charge transfer from the anion to the cation.[32]

The trend of the anions of the compounds analysed so far according to their basicity is:

$$Br^- > [BF_4]^- > [PF_6]^- > [NTf_2]^-$$

The charge transfer is higher in the case of halide which results in shift at lower binding energy of the N 1s and $C_{N\text{-}C\text{-}N}$ a binding energy shifted to the lower of the photoelectron peaks. The value for the N $1s_{Im}$ region for $[(C_8BzIm)_2Py]Br_2$, $[(C_8BzIm)_2Py][BF_4]_2$ $[(C_8BzIm)_2Py][PF_6]_2$ and $[(C_8BzIm)_2Py][Ntf_2]_2$ are: 401.2 eV, 401.3 eV, 401.4 eV and 401.6 eV, Figure 3.12 which are consistent with the literature.[16]

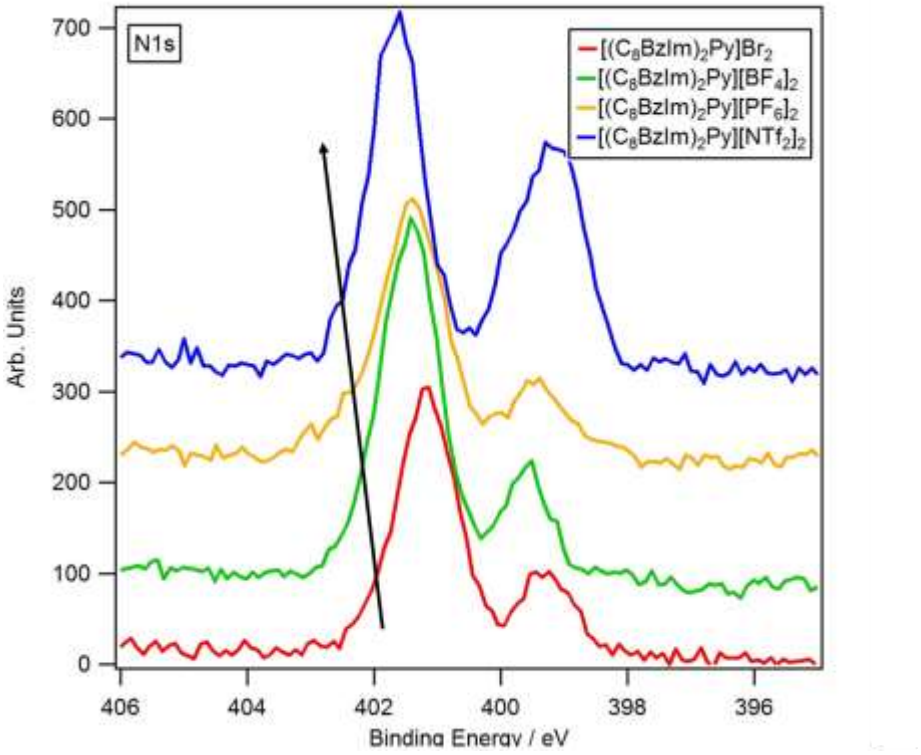


Figure 3.12 Binding energies for N1s for a)$[(C_8BzIm)_2Py]Br_2$, b)$[(C_8BzIm)_2Py][BF_4]_2$ c)$[(C_8BzIm)_2Py][PF_6]_2$ and d) $[(C_8BzIm)_2Py][Ntf_2]_2$. The photoelectron emission intensity is normalised to the intensity of the N_{Im} 1s region for $[(C_8BzIm)_2Py]Br_2$. All XPS spectra are charge corrected by referencing the C_{Ali} component to 285.0 eV.

Looking at the literature present where N 1s values are reported shows a dependence on anion-cation interaction on the N 1s peak.

3.6 Conclusion and future studies

The synthesis and characterisation of dicationic pincer ligands $[(C_nBzIm)_2Py][X]_2$ are reported. ***The synthesis has been optimised from the previous literature with a crucial modification of the compounds recrystallization step to achieve high level of purity of all the product chapter section 2.3***.[7, 33] Thermogravimetric analysis allows insight into the long-term thermal decomposition behaviours of the ionic samples reflected by high decomposition temperature. Also, the effect of different anions to the electronic composition of the cation substituted with varying chain length are considered. The assignment of the fragmentation of the compounds using TGA analysis was discussed comparing the result reported in literature for similar compounds.[20] Finally, yet importantly, it is crucial to investigate the thermic stability of the NHCs as they are used as a stabiliser in the synthesis of nickel nanoparticles through decomposition of the acetylacetonate-oleylamine complex.

The first attempt of the C1s fitting models for $[(C_8BzIm)_2Py][X]_2$ and $[(C_nBzIm)_2Py][Ntf_2]_2$ are discussed. A reliable fitting model for the C1s envelope is proposed by taking into account the shake-up/off phenomena. The charge correction is performed using the C_{Ali} 1s for n ≥ 8. Once, ensured that a reliable binding energy is obtained for the various components in the system studied; the assignment of the components C_{Ar}, C_{CN} and C_{NCN} is discussed. Moreover, the design of different ligands based on benzimidazolium ring is also considered to achieve better understanding of the C1s fitting model. The data reported in this thesis show a very different deconstructed photoemission peaks compared to the previous literature. The C1s fitting model is deconstructed behind a single broad photoemission peaks where all the different components are contained. The resonance structure of the bis(benzimidazolin-2-ylidene) have an effect on the electron emitted analogously for polyaromatic system.[34] The N1s fitting model of $[(C_8BzIm)_2Py][X]_2$ show that the dicationic species presents similar behaviours detected before for single ring imidazolium ionic liquids.[12] In the future, different anions will be tested to allow a full comprehension of the influence of the anions in charge distribution within the pincer structure.

3.7 Bibliography

1 E. F. Smith, F. J. M. Rutten, I. J. Villar-garcia, D. Briggs and P. Licence, *Langmuir*, 2006, **22**, 9386–9392.

2 I. J. Villar-Garcia, E. F. Smith, A. W. Taylor, F. Qiu, K. R. J. Lovelock, R. G. Jones and P. Licence, *Phys. Chem. Chem. Phys. Phys. Chem. Chem. Phys*, 2011, **13**, 2797–2808.

3 A. W. Taylor, S. Men, C. J. Clarke and P. Licence, *RSC Adv.*, 2013, **3**, 9436–9445.

4 H.-P. Steinrück and P. Wasserscheid, *Catal. Letters*, 2015, **145**, 380–397.

5 N. V. Plechkova and K. R. Seddon, *Methods Reagents Green Chem. An Introd.*, 2007, **2000**, 103–130.

6 A. R. Santos, R. K. Blundell and P. Licence, *Phys. Chem. Chem. Phys.*, 2015, **17**, 11839–11847.

7 T. Tu, W. Assenmacher, H. Peterlik, G. Schnakenburg and K. H. Dötz, *Angew. Chemie - Int. Ed.*, 2008, **47**, 7127–7131.

8 T. Tu, W. Assenmacher, H. Peterlik, R. Weisbarth, M. Nieger and K. H. Dötz, *Angew. Chemie Int. Ed.*, 2007, **46**, 6368–6371.

9 R. A. Sheldon, *Green Chem.*, 2005, **7**, 267–278.

10 J. L. Anderson, R. Ding, A. Ellern and D. W. Armstrong, *J. Am. Chem. Soc.*, 2005, **127**, 593–604.

11 C.-M. Jin, C. Ye, B. S. Phillips, J. S. Zabinski, X. Liu, W. Liu and J. M. Shreeve, *J. Mater. Chem.*, 2006, **16**, 1529–1535.

12 S. Men, PhD Thesis, University of Nottingham, 2011.

13 D. S. Mitchell, PhD Thesis, University of Nottingham, 2014.

14 J. Park, E. Kang, S. U. Son, H. M. Park, M. K. Lee, J. Kim, K. W. Kim, H. J. Noh, J. H. Park, C. J. Bae, J. G. Park and T. Hyeon, *Adv. Mater.*, 2005, **17**, 429–434.

15 I. J. Villar-Garcia, E. F. Smith, A. W. Taylor, F. Qiu, K. R. J. Lovelock, R. G. Jones and P. Licence, *Phys. Chem. Chem. Phys.*, 2011, **13**, 2797–808.

16 S. Men, D. S. Mitchell, K. R. J. Lovelock and P. Licence, *ChemPhysChem*, 2015, **16**, 2211–2218.

17 C. Clarke, PhD Thesis, University of nottingham, 2015.

18 A. W. Taylor, S. Men, C. J. Clarke and P. Licence, *RSC Adv.*, 2013, **3**, 9436.

19 W. Wang, Y. Ling, L. J. Yang, Q. L. Liu, Y. H. Luo and B. W. Sun, *Res. Chem. Intermed.*, 2016, **42**, 3157–3168.

20 Y. Cao and T. Mu, *Ind. Eng. Chem. Res.*, 2014, **53**, 8651–8664.

21 H. Toiserkani, H. Sheibani and K. Saidi, *Eur. Polym. J.*, 2010, **46**, 185–194.

22 A. Deyko, K. R. J. Lovelock, J.-A. Corfield, A. W. Taylor, P. N. Gooden, I. J. Villar-Garcia, P. Licence, R. G. Jones, V. G. Krasovskiy, E. a Chernikova and L. M. Kustov, *Phys. Chem. Chem. Phys.*, 2009, **11**, 8544–8555.

23 A. Deyko, S. G. Hessey, P. Licence, E. A. Chernikova, V. G. Krasovskiy, L. M. Kustov and R. G. Jones, *Phys. Chem. Chem. Phys.*, 2012, **14**, 3181–3193.

24 E. F. Smith, F. J. M. Rutten, I. J. Villar-Garcia, D. Briggs and P. Licence, *Langmuir*, 2006, **22**, 9386–9392.

25 K. R. J. Lovelock, I. J. Villar-garcia, F. Maier, H. Steinru and P. Licence, *Chem. Rev.*, 2010, **110**, 5158–5190.

26 E. F. Smith, I. J. Villar Garcia, D. Briggs and P. Licence, *Chem. Commun.*, 2005, 5633.

27 J. F. Moulder, W. F. Stickle, P. E. Sobol and K. D. Bomben, *Handbook of X-ray Photoelectron Spectroscopy*, 1992.

28 C. D. Wagner, L. E. Davis, M. V Zeller, J. A. Taylor, R. H. Raymond and L. H. Gale, *Surf. Interface Anal.*, 1981, **3**, 211–225.

29 M. F. Delcroix, E. M. Zuyderhoff, M. J. Genet and C. C. Dupont-Gillain, *Surf. Interface Anal.*, 2012, **44**, 175–184.

30 J. C. Vickerman and I. S. Gilmore, *Surface Analysis The Principal Techniques*, John Wiley & Sons Ltd., Chichester, 2009.

31 B. Sjögren, S. Svensson, A. N. de Brito, N. Correia, M. P. Keane, C. Enkvist and S. Lunell, *J. Chem. Phys.*, 1992, **96**, 6389–6398.

32 S. Men, K. R. J. Lovelock and P. Licence, *Phys. Chem. Chem. Phys.*, 2011, **13**, 15244–15255.

33 K. D. M. MaGee, G. Travers, B. W. Skelton, M. Massi, A. D. Payne and D. H. Brown, *Aust. J. Chem.*, 2012, **65**, 823–833.

34 M.-C. Tremblay and R. W. Paynter, *Surf. Interface Anal.*, 2003, **35**, 502–514.

Chapter 4

Nickel nanoparticles into multi-walled nanofibers

4.1 Introduction

The most common stabilisers for capped nanoparticles are organic ligands, surfactant, polymers and dendrimers. In this study the possibility to use NHCs as a stabiliser is explored.[1] Whilst, NHCs are well-known as ligands in ruthenium complexes for olefin metathesis in ILs media.[2] The use of NHCs as stabiliser for nanoparticles is still in its infancy.[3-5]

NHCs are compounds derivatives of natural product with an ionic moiety which make them precursors for ionic liquids with peculiar chemical and physical properties.[6,7] The NiNP-NHCs represent the first example of synthesis from this specific type of heterocyclic compounds.[6] Nickel is very interesting element to be investigated due to its relatively low cost compared to precious metals and might represent a real sustainable alternative. In addition, capped nanoparticles are surrounded by the organic layer which makes them eco-friendly as the metal part is not in contact with the environment.[8]

To solve the outstanding problem of selectivity, stability and recyclability of metal catalyst and its support in catalysis, the NiNPs are confined in GNF to create a nanoreactor. When nanoparticles are inserted in GNF, there are two types of interactions between NiNPs and GNF. The first one is the attractive or repulsive interaction between the nanoparticles residing at the step edges. The second one is the host-guest interactions between the nanoparticles and the corrugated interiors of the GNF (described in more details in chapter 1). The first variable depends upon the preparation process, discussed in paragraph 4.3. The second type of interaction is determined by both size of the nanoparticles and the GNF sizes discussed in paragraph 4.4.

The structure of a tubular carbon nanofiber is constituted by two coaxial highly graphitic cylinders: the outer cylinders are a continuous and atomically smooth layers of graphite Figure 4.1 (a) and the inner cylinder consisting of long herringbone stacks of graphitic cones (b).[9-11]

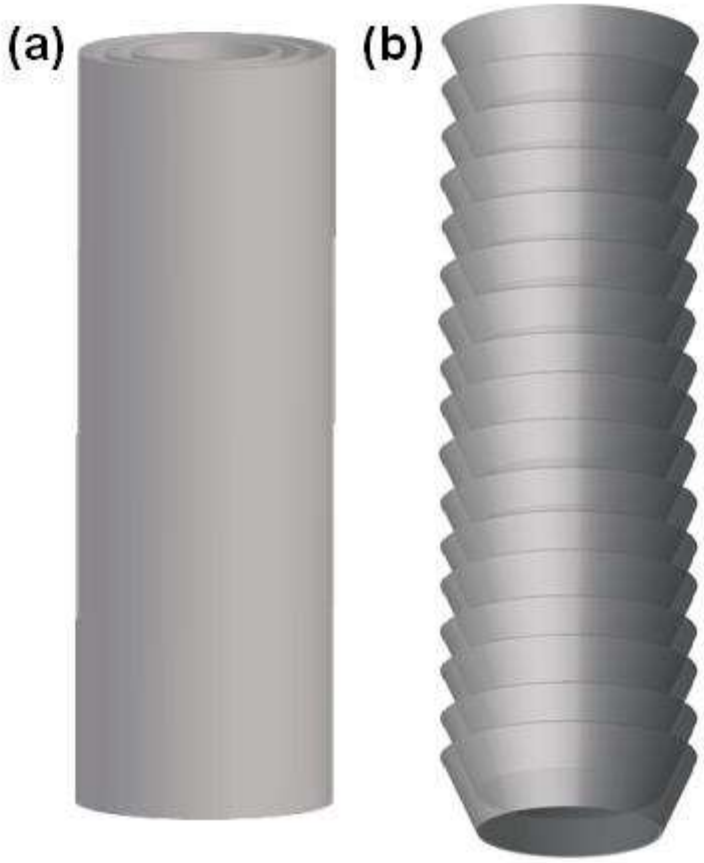


Figure 4.1 Representation of the two main layers of a hollow graphitised nanofibers (GNF): (a) external smooth surface (b) internal stacked shortened cones.[11]

The TEM image reveals the morphological differences between the internal and external surface of a GNF, (Figure 4.2, a). The inside walls of the GNF are planes orientated at an angle closed to 30° from the main axes highlighted by a black arrow, (Figure 4.2, b). The stacked cones create step edges as anchoring points spaced at 8-15 nm.

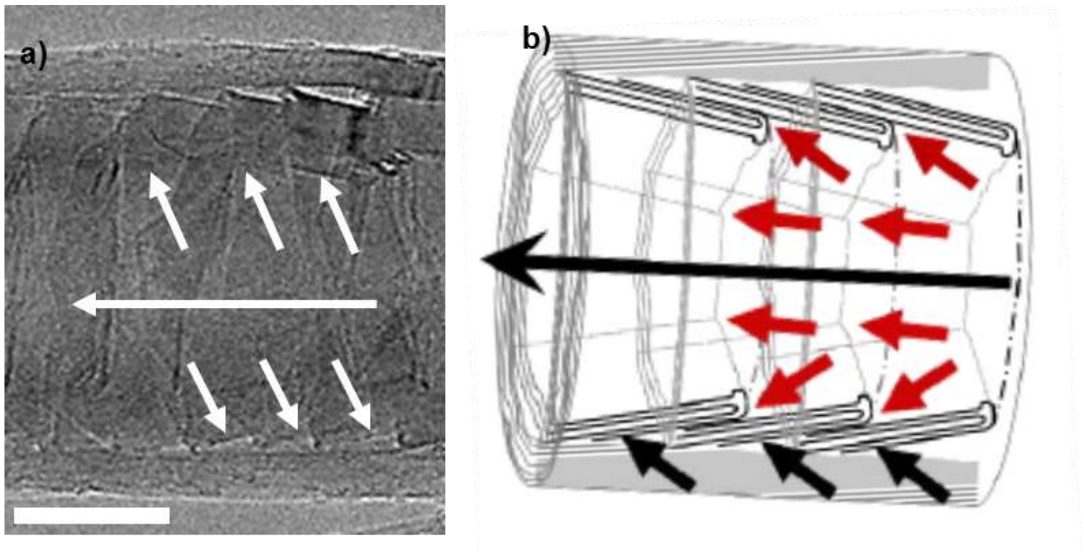


Figure 4.2 a) Bright field TEM (BF-TEM) Image of GNF which illustrates the coaxial structure formed of several layers of graphene, a core structure with few half cone graphene layers and an external smooth structure acquired using an accelerating voltage of 200 kV. Scale bar is 20 nm; b) Schematic representation of the GNF external surface made of coaxial continuous cylindrical layers of graphene. The black arrows show the internal conic wall structures in which the step edges are highlighted with the red arrows.[12]

To give an idea of the morphology of GNF, and the role of the host-guest interaction between the step edges and the nanoparticles, here are reported the technical details.[13] The GNF length ranges from 5 to 100 μm; the internal diameter between 50 to 80 nm. The surface areas are between 80 – 200 m^2/g. The individual cones are spaced by 8-15 nm from each other to form the step edges with height of 3.3 nm, pointed by the short red arrows, Figure 4.2 (b).

Metallic nanoparticles possess a high surface area versus volume and their size is not always homogenous because nanoparticles are intrinsically metastable. Hence, small nanoparticles are less thermodynamically stable than the bigger nanoparticles.[14] By contrast, the aggregation of nanoparticles to form bigger nanoparticles with lower surface area to volume is thermodynamically favourable.[1] In order to get a homogenous size distribution of particles it is necessary to add to the reaction a stabiliser that allows the nanoparticles to stay small and with regular size dispersion (5-10 %).[15] There are many types of synthetic strategies which use stabilising agents added in order to limit the nanoparticle sizes distributions.[16] Ionic liquids, organic molecules or other surfactants are used to achieve a colloidal dispersion with a well-defined texture and size distribution.[1, 17, 18] The size of the nanoparticles is very important especially in terms of catalytic activity high surface

area means higher availability of catalytic active sites and higher reactivity. The application of nanoparticles ranges from catalysis,[8] magneto-chemistry,[19] optically device and health care.[20-24] The catalytic activity and the functional properties of nanoparticles are correlated to their size.[25, 26] The nanoparticle size change in function of the increment of their surface with a contemporaneous decrement of the number of NPs for a delimited area. GNF present large channels which does not allow a snug fit scenario as in the case of the multi-walled nanotube filled with gold nanoparticles.[27, 28] Conversely, the anchoring of the NPs to the step edges and corrugated interiors are crucial factors which allow the insertion of NP in GNF.[12]
The change in particle size can occur during their synthetic procedure due to Ostwald ripening when small atoms or cluster of atoms diffuse from smaller to larger NPs, Figure 4.3 a); and particle migration followed by coalescence: several particles move to consolidate in a bigger particle, Figure 4.3 b).[11,29-31]

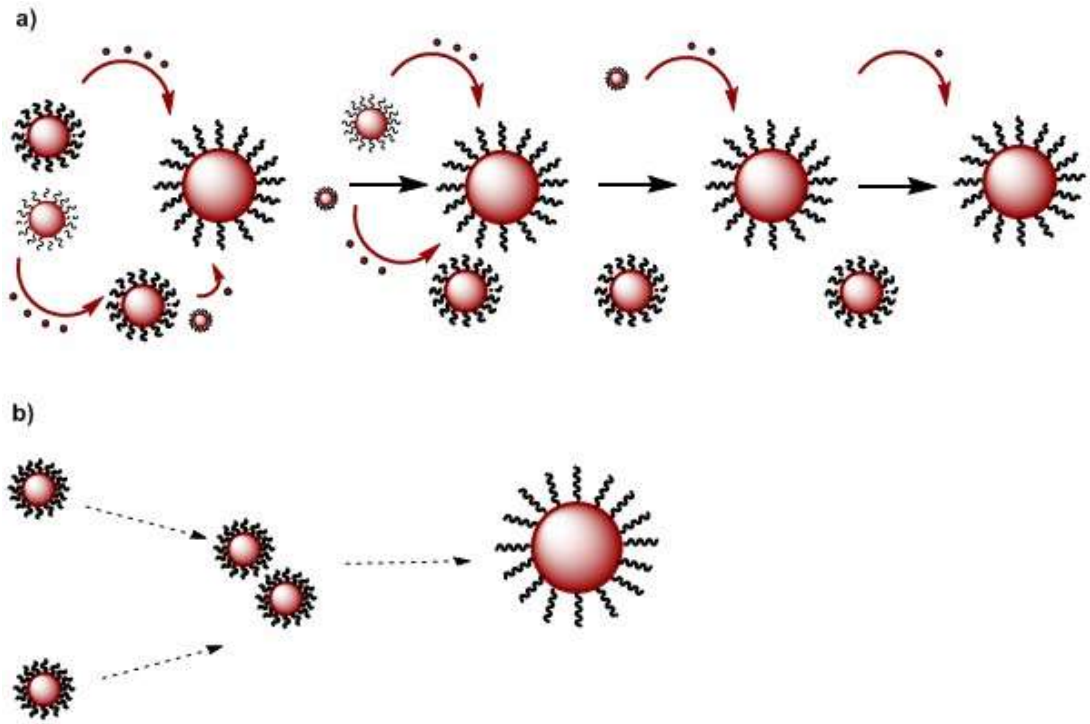


Figure 4.3 Illustration of the two processes responsible for the growth of NPs: a) Ostwald ripening and b) nanoparticle migrations followed by coalescence. The effect of both a) and b) causes a decrease of the number of NPs, by contrast the diameter of NPs grows.

The presence of different molecules influences the stability and consequently the size of the nanoparticles. The chapter investigates the nature of the stabilising agent and its influence on the catalytic activity tested in the electrochemical reaction.[32, 33]

By determining the d-spacing is possible to assign the crystal structures of the NPs.[34-36] The typical spatial distribution for nickel atoms in nanoparticles depends upon the synthetic methodology and are usually the face-centred cubic structure (fcc), the hexagonal close-packed (hcp) and cubic structures.[37] The precise determination of the distribution of atoms in nanoparticles is extremely important in the catalytic applications.[38] In addition, another important parameter is the nanoparticle size which has direct effect on their applications.[8,39]

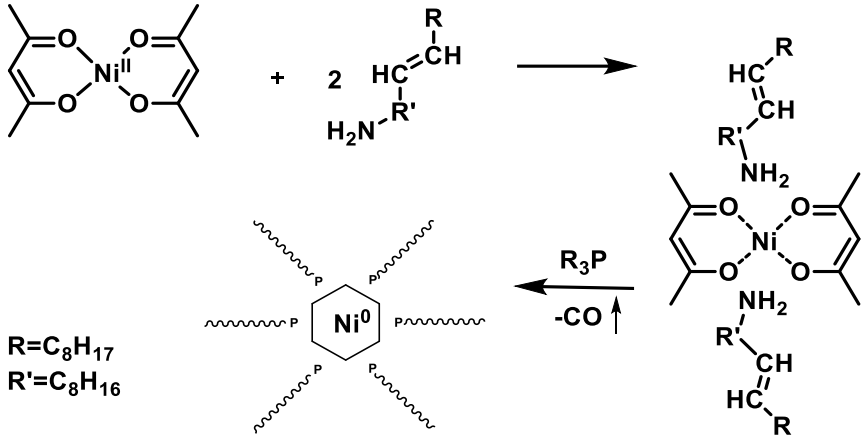
4.2 Aims and objective of this chapter

The first aim of this chapter is to illustrate the synthesis of NiNPs by investigating the effect of the use of two different stabilising agents on the nanoparticles size. The approach to the syntheses is discussed in order to obtain direct information between stabilisers and nanoparticles formation. The second aim is to explain the encapsulation of NiNPs in GNF and the synergetic effects between NiNPs and GNF. This chapter gives a short overview of the application of NiNPs@GNF nanoreactor in the electrochemical oxidation of propargyl alcohol using two types of nanoreactors the NiNP-TOPs@GNF and the NiNP-NHCs@GNF.

4.3 Result and discussion

4.3.1 Size distribution of nanoparticles

The method described in this paragraph allows synthesising colloidal nanoparticles with a homogeneous size distribution. The methodology is based on a modified literature procedure achieved the yield of 45% $_{w/w}$ of monodisperse NiNPs.[8] A nickel acetylacetonate-oleylamine complex is formed first followed. The thermal decomposition of the complex forms NiNPs stabilised by TOP, scheme 4.1.

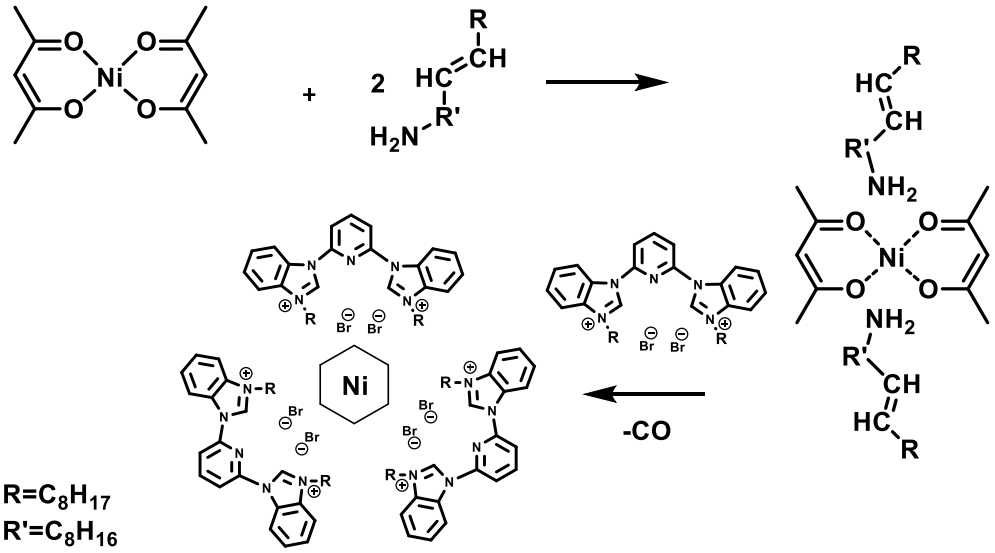


Scheme 4.1 Synthesis of the nickel nanoparticles by the thermal decomposition of acetylacetonate-oleylamine complex stabilised by TOP, the nickel is reduced from Ni^{II} to Ni^{0} whereas (acac) is oxidised to CO; graphic representation of a NiNP-TOPs.

The nickel acetylacetonate-oleylamine complex is formed when the mixture becomes a blue-green liquid. In the second part of the reaction trioctylphosphine (TOP) is added in an argon flow and heated up to 215 °C under stirring. The formation of colloidal nanoparticles is represented by the colour change from blue-green to black.[8, 37] The mechanism of metallic NiNPs formation involves two contemporaneous processes: the reduction of Ni(II) which is favoured by the presence of oleylamine, mild reducing reagent, and the decomposition of the ligand (acac) which is shown by the formation of gas, Scheme 4.1.[40]

4.3.2 Nickel nanoparticles stabilised by NHCs

The method described in this section allows the synthesis of a new type of free-standing nickel nanoparticles stabilised by N-heterocyclic carbene compounds. The synthetic procedure for the new NiNPs involves the formation of a nickel complex with oleylamine followed by the addition of the stabiliser, Scheme 4.2.



Scheme 4.2 Synthesis of the nickel nanoparticles by thermic decomposition of acetylacetonate-oleylamine Ni complex stabilised by NHCs, graphic representation of NiNP-NHCs.

The reaction is carried out neat under argon, and the acetylacetonate-oleylamine Ni complex forms as a blue-green compound. The 2,6-bis(octylbenzimidazolium)pyridine dibromide is kept under an argon flow and then mixed with the nickel complex. The reaction mixture is stirred and heated up to 215 °C until the colour of the solution changes from blue-green to black, indicating the formation of colloidal nanoparticles.[8, 16] The mechanism tentatively assigned to the thermal decomposition of the acetylacetonate shown by the formation of gas and Ni(II) is exposed to a reducing atmosphere. The NiNP are formed and stabilised by the benzimidazolyl ligand.

4.3.3 Characterisation of the nickel nanoparticles stabilised by trioctylphosphine

The synthesis of NiNP capped with TOP as a surfactant is based on a modified literature procedure, described in section 4.3.1.[8] TEM images of these NiNP-TOPs reveal a homogeneous size distribution of nanoparticles with an average size diameter of 3.4 nm ± 0.7 nm (N=100), (Figure 4.5). The super lattice structure for the NiNP-TOPs represented in Figure 4.5 shows a characteristic hexagonal arrangement of the nickel particles.[8] A hexagonal arrangement (super lattice) of the system is characterised by four axes, three of which has the same length and intersect the main axis at 90 ° and crossed it at 120 °.

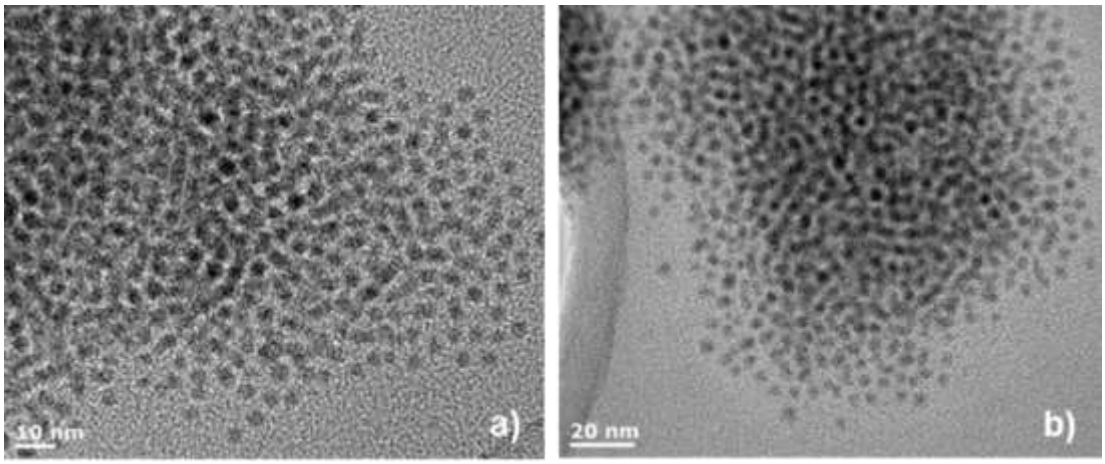


Figure 4.5 BF-TEM images of NiNP-TOPs. High magnification images of the NiNP-TOPs on holey carbon copper grid. Scale bars 10 nm (a) and 20 nm (b).

The EDX analysis of a limited area on NiNPs clusters confirms the presence of phosphorus in the capping layer surrounding the particle, Figure 4.6.

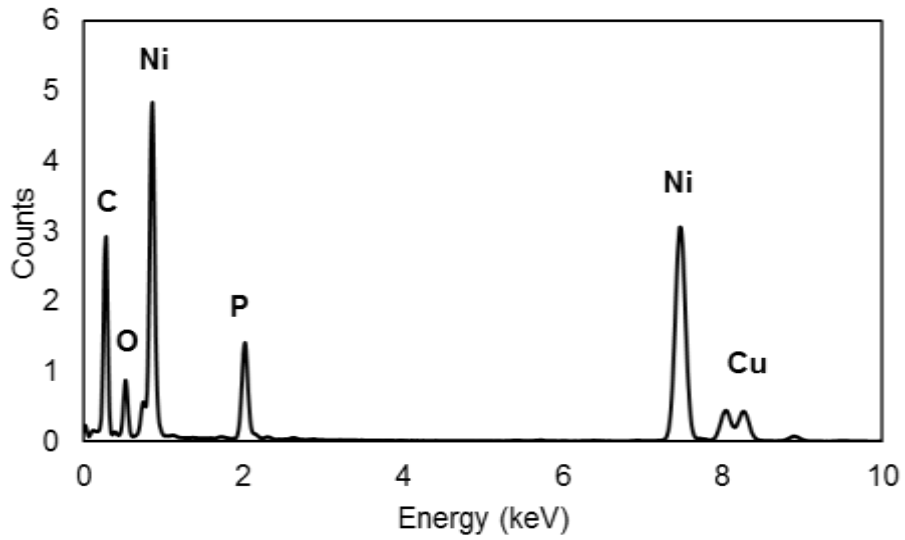


Figure 4.6 EDX spectrums of nickel nanoparticles stabilised by TOP shows Ni, P and O and Cu.

The tabulated results provide a semi-quantitative view of the elemental composition in units of both weight percent and atomic percent. (Table 4.1). *The stoichiometric excess of P might be due to the free TOP residing within the TOP molecule attached to the* NiNP.[11,12]

Table 4.1 Tabulated results of the elemental composition in units of both weight percent and atomic percent.

Element	Weight %	Atomic %
C	17.36±0.10	39.08
O	14.77±0.07	24.95
Ni	44.51±0.09	20.49
P	11.04±0.05	9.64
Cu	10.43±0.06	4.44

The atomic percentage determined by EDX of Ni and O is nearly 1:1 as expected for the molecular formula of nickel monoxide. The formation of oxide might be occurred when the NiNP-TOPs (not bulky stabilisers) were exposed to air post synthesis. A second possibility in regards of oxide formation might be attributed to the CO formed during the NINPs synthetic procedure.[14] Conversely, the content of oxygen might be related to the oxygen functional groups contained on the surface of the amorphous carbon TEM support and a tiny amount from the organic capping layer as TOP easily oxidises to produce TOPO.[41] The P present is contained in the capping layer of the NiNPs. The vast majority of carbon comes from the TEM grid and some contribution might also be attributed to the organic layer attached to the particle. Also the presence of copper can be attributed to the metal contained in the TEM grid.[42]

4.3.4 Characterisation of the NiNPs stabilised by N-Heterocyclic Carbene

The synthesis of Ni-NHCs nanoparticles is a new methodology to synthesise nanoparticles, already reported in paragraph 4.3.2. The nanoparticles form big aggregates, Figure 4.8. In this instance, it was used an excess of surfactant, NHCs to stabilise the NiNPs, around 10% according to the TGA. The excess of stabiliser promotes a well-defined self-assembly of nanoparticles, Figure 4.8.

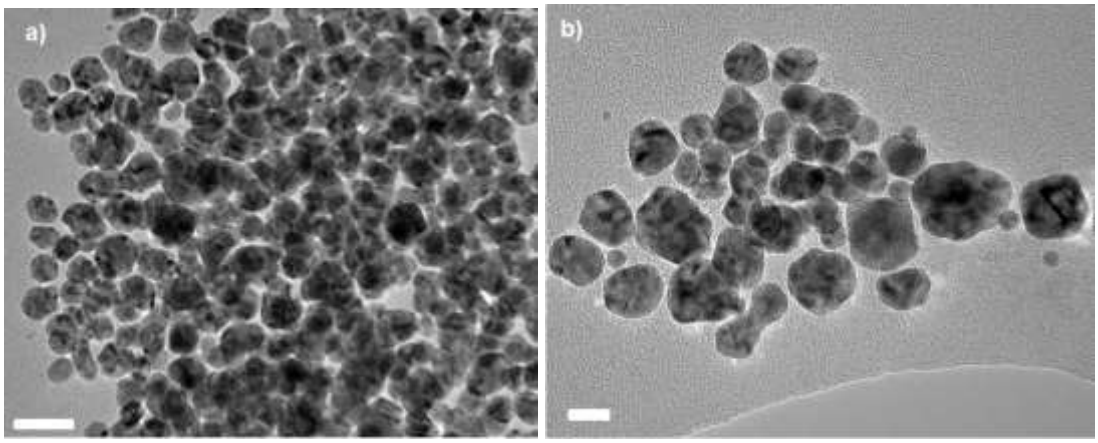


Figure 4.8 a) BF-TEM images of NHCs NiNPs; b) High magnification images of the NHCs NiNPs on holey carbon copper grid. Scale bars 50 nm (a) and 20 nm (b).

NiNPs present a distribution size which as shown in the diagram, Figure 4.9. The average diameter of the nanoparticles is 15.31±4.39 nm, Figure 4.8-4.9. The shape of the particle is faceted and the aspect ratio is 1.41. The aggregation of the nanoparticles is mainly due to the higher thermodynamic stability of bigger agglomerates compared to smaller one as explained in section 4.1. Additionally, the intrinsic magnetic properties of nickel nanocrystal enhance the formation of aggregates.[19, 43]

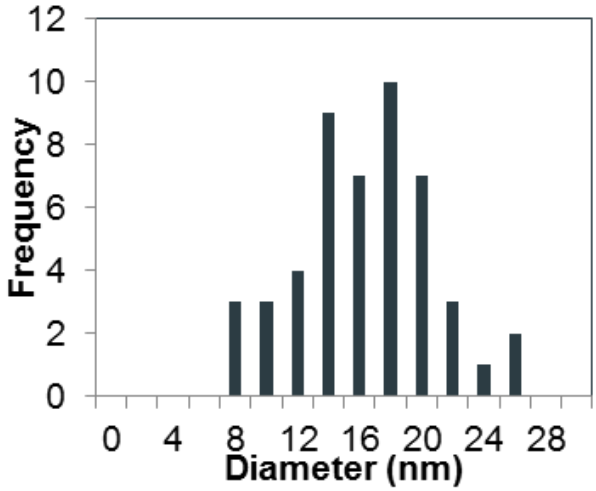


Figure 4.9 Size distribution of NiNPs stabilised by NHCs determined from TEM images.

The EDX analysis of a limited area of NiNPs cluster shows a small content of oxygen. Presumably, in this case the capping layer has been able to prevent the oxidation of the particle, Figure 4.10. Perhaps, the bulky capping layer isolates the

nickel from the contact with atmospheric oxygen so that the formation of oxide layer on the surface of the nanoparticles is hindered.

It is worth noticing the formation of faceted nanoparticles with an average diameter size of 15.4 nm which seems to be associated to the use of a different capping agent as the reaction conditions used are the identical for the two NiNPs.[34] It has been proven that the different capping agents influence the formation of two nanoparticles possessing different morphologies. The result suggests that the hindrance of NHCs which contains two long chains has affected the size and the shape of the particles. The temperature not completely constant while the reaction takes place may suggest the formation of particles with not homogenous size distribution, according to previously observed patterns, Figure 4.11 a).[44]

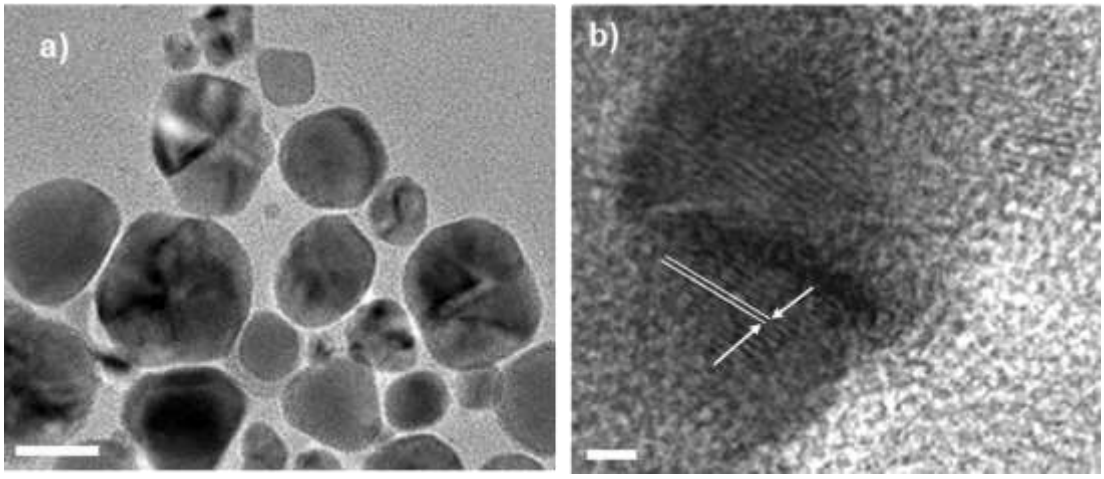


Figure 4.11 a) Low-magnification of the NiNP-NHCs showing the size distribution not homogeneous; b) BF-TEM images of NiNP-NHCs with d space highlighted by arrows (0.203 nm). Scale bars 20 nm (a), 5 nm (b).

To define the structure of the NiNP the distance between crystallographic lattices also called interlayer d spacing measured in HRTEM image is found to be 0.203 nm and 0.170 nm, Figure 4.11 b). The NiNP-NHCs present faceted structures which partly hindered the determination of the d spacing, Figure 4.12. The corresponding FFT electron diffraction pattern, Figure 4.12 b) shows sharp spots with plane distances between 0.203 nm and 0.170 nm which designate the d-spacing for pure cubic metallic nickel. Conversely, in some particles the FFT gives the opportunity to determine a d spacing of 0.219 nm very close to the typical d-values for metallic nickel possessing a fcc structure.[45]

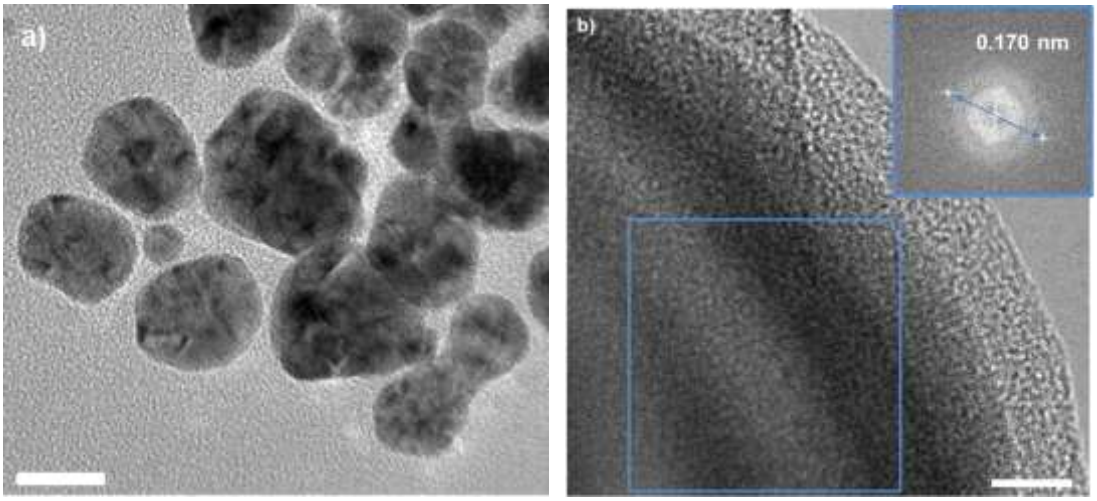


Figure 4.12 a) BF-TEM images of NiNPs stabilised by NHCs; b) HR-TEM of NiNP stabilised by NHCs and d spacing extracted from FFT (Fast Fourier Transform) of the area equal to 0.170 nm. Scale bars are 20 nm (a) and 10 nm (b).

4.3.5 Comparison of TOP and NHCs stabilised nickel nanoparticles

The TEM images in Figure 4.12 clearly illustrate that in both case the synthesis of nanoparticles was possible. The NiNP-TOPs present regular geometry and size distribution compared to NiNP-NHCs. The difference in average size can be attributed to the spatial distribution of the organic capping layer used and available while the reaction takes place. The capping layer of the NiNP-NHCs is more sterically hindered than NiNP-TOPs, thus the amount of capping layer is less accessible while the thermal decomposition of acetylacetonate-oleylamine Ni complex takes place.[46] Oleylamine plays a role in the formation of nanoparticles as solvent and mild reducing agent.[40] The reaction mechanism of the nanoparticles formation is credited to the reduction of the nickel (II) into hexagonal and cubic Ni phases. [40, 47]

The presence of the organic coating layer is investigated with TGA for both NiNPs sample stabilised by TOP and NHCs. In order to determine the quantity of organic capping layer of the NiNPs TGA experiments were performed under atmospheric pressure conditions in air. The air flow rates were set as 10 cm min^{-1}, Figure 4.13 a) and b). The TGA show an excess of stabiliser in the NiNP-NHCs, Figure 4.13 b). The oxidation process which affects the particles shows that only 14.48% of the sample is made of metal which is able to resist through the thermic process as it needs higher temperature to be boiled off which is extremely high (over 2000 °C).

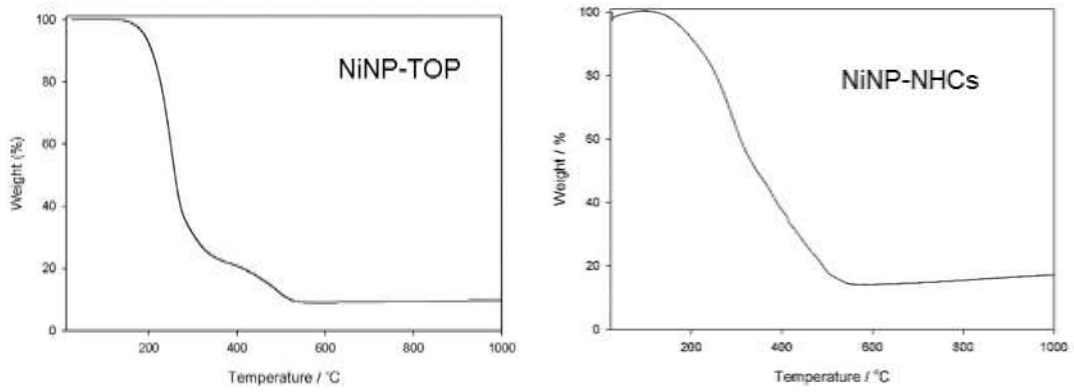


Figure 4.13 a) TGA of NiNP-TOPs of y in Weight percentage over x in degree Celsius, the weight percentage of residual NiNPs is 9 %; b) TGA of NiNP-NHCs of y in Weight percentage over x in degree, the weight percentage of residual NiNPs is estimated to be 14 %. Measurements were conducted in air at a rate of 10 ºC·min^{-1} up to 1000 ºC.

The onset peak is at 155 °C with weight loss around 0.8 % for the NiNP-TOPs whereas for the NiNP-NHCs the onset peak is at 134 °C with weight loss of 2 %. The dramatic weight loss for the former is present at 252 °C and correspond to 42 %. By contrast, the nanoparticles stabilised by NHCs present a dramatic weight loss at 295 °C which corresponds to 35 %. The loss of the total weight in both cases is related to the thermal decomposition of the organic layer.[48, 49] The oxidation of the specimens in air proceed towards a multi-steps curve approaching a constant value and a plateau above 600 °C indicating the complete oxidation of the capping layer. Both curves present similar thermal decomposition pattern which shows a significant difference of the weight percentage at $T_{f,3}$ in the sample of NiNP-TOPs compared to the NiNP-NHCs, 9 % and 14 % respectively, Table 4.2.[49]

Table 4.2 Measured values of T_i (procedural decomposition temperature, peak onset), T_f (final temperature), and Tp (temperature associated with the first derivative where the greatest rate of change of the slope in the weight loss profile correspond to the weight at Tp (%)

Sample	**$T_{i,1}$ (ºC)**	**$T_{f,2}$ (ºC)**	**$T_{f,3}$ (ºC)**	**Weight (%)**	**T_p (ºC)**	**Weight at T_p (%)**
NiNP TOP	155			99	252	58
		363		23		
			540	9		
NiNP NHCs	134			98	295	65
		304		61		
			545	14v		

The presence of a sterically hindered capping layer in the second case allow the formation of bigger nickel cluster, surrounded by a thicker organic layer, Figure 4.14 b) compared to the nickel nanoparticles stabilised by TOP, Figure 4.14 a).

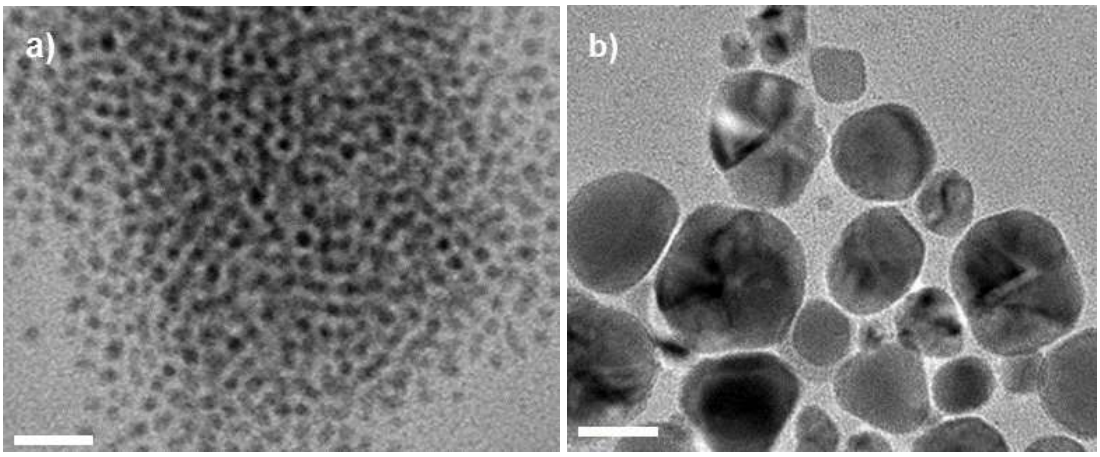


Figure 4.14 a) BF-TEM images of TOP NiNP-TOPs; b) BF-TEM images of NiNP-NHCs. Scale bars are both 20 nm (a) and (b).

4.3.6 IR Trioctyl phosphine and N-Heterocyclic Carbene stabilised Nickel nanoparticles

IR spectroscopy is a useful tool to understand the stretching modes and bending modes of the organic molecules attached to the nanoparticles and the free molecules surrounding the nanoparticles capping layer. The IR spectra are all recorded in the range 400-4000 cm^{-1}, Figure 4.15 and Figure 4.16. The broad and intense band centred at 3332 cm^{-1} is assigned to the O-H stretching vibration of the interlayer water molecules and of the H-bound OH group or some literature ascribed this vibration mode to carbon chains, Figure 4.15.[50]

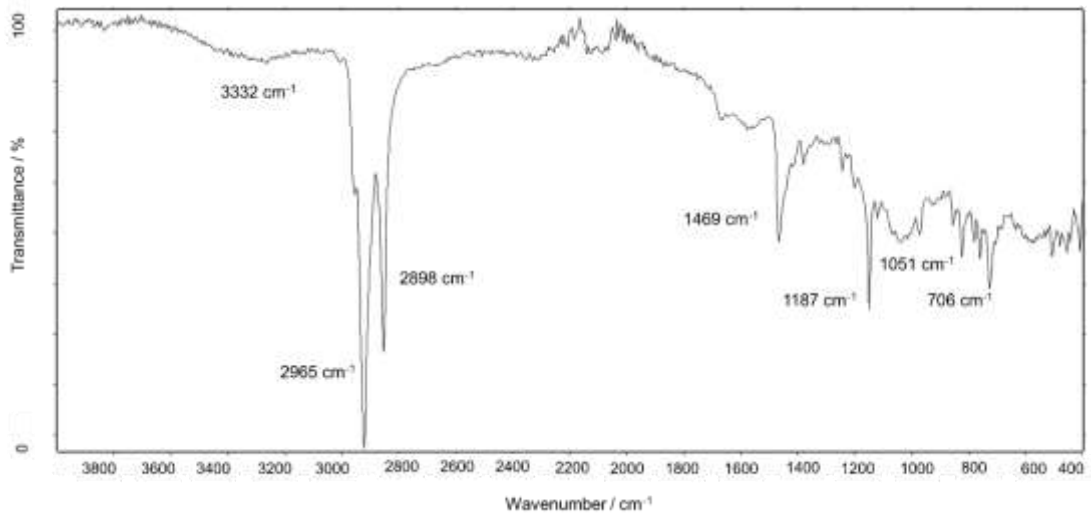


Figure 4.15 FT-IR spectra of NiNPs stabilised by trioctylphosphine.

The two narrow and strong peaks at 2965 cm^{-1} (asymmetric stretching band CH_3) and 2989 cm^{-1} (asymmetric stretching band CH_3) are associated to the C-H stretching modes of the ligand carbon chain. The peak at 1469 cm^{-1} represents the CH_2 bending mode. The peak at 706 cm^{-1} indicates the rocking mode of long chains.[51]The shift from the typical 720 cm^{-1} can be explained by the presence of P which is more electronegative than the atoms present in the chain.[51]

The peak at 1187 cm^{-1} correspond to P=O stretching mode. Unfortunately the asymmetric deformation of CH_3 is overlapped with the CH_2 bending mode. The absence of the two clear peaks in the finger print region (400-1000 cm^{-1}) expected at 522 cm^{-1} and 470 cm^{-1} associated to the Ni–O vibration bond are a clear indication that the particles are metallic.[52] The IR results are in contrast with the EDX run in TEM mode.[53] Some of the oxygen detected in EDX might come from the capping layer of the NiNPs as shown in Figure 4.15.[15] However, the oxygen seen in EDX is not ascribable to the nickel particles. A hypothetical nickel monoxide particle

should present two distinct peaks. The FT-IR spectrum of the NiNP-NHCs present similar features compare with the FT-IR spectrum of the NiNP-TOPs, Figure 4.16.

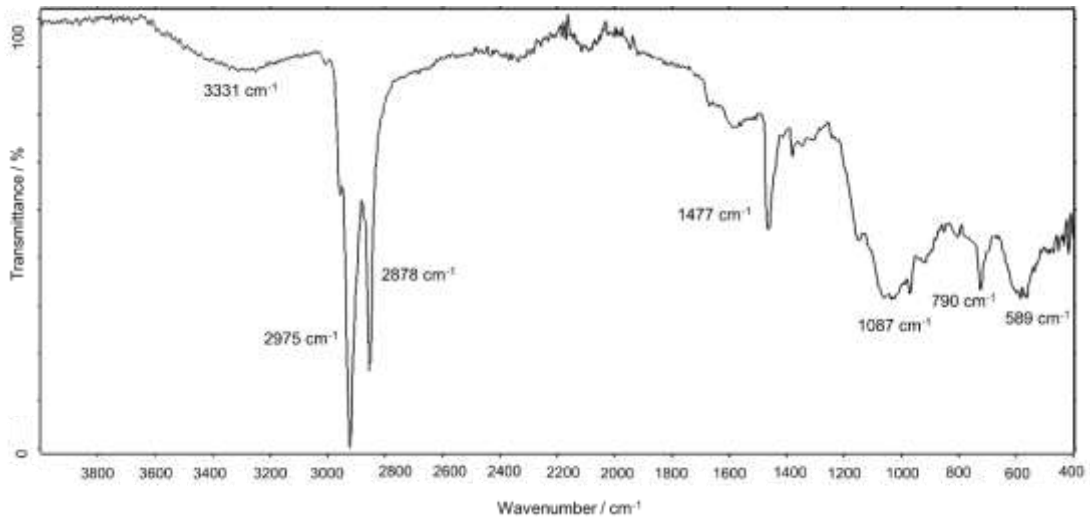


Figure 4.16 FT-IR spectra of Ni nanoparticles stabilised by NHCs.

The broad and intense band centred at 3331 cm^{-1} is assigned to the O-H stretching vibration of the interlayer water molecules and of the H-bound OH group or some literature ascribed this vibration mode to carbon chains.[50] The two narrow and strong peaks at 2975 cm^{-1} and 2878 cm^{-1} are associated to the C-H stretching modes of the ligand carbon chain. The peak at 1477 cm^{-1} represent the C-H bending mode. The peak at 790 cm^{-1} indicates the rocking mode of long chains. The broad signal at 589 cm^{-1} is related to the presence of the aromatic structure of the capping agent. Again, The lack of the two peaks in the finger print region (400-1000 cm^{-1}) expected at 522 cm^{-1} and 470 cm^{-1} for the Ni–O stretching are a clear indication that the particles are metallic.[53]

4.4 Encapsulation of nickel nanoparticles into multi-walled nanofibers: host-guest interactions

In this work has been used graphitised nanoparticles which are quite large hollow structure compared to nanotubes. The interaction between nanoparticles and nanofibers depends upon the size of the nanoparticle and both the internal diameter of the nanofibers and the high of step edges. The technical details of the nanoparticles are described in paragraph 4.1 the internal diameter of a graphitised nanofibers is between 50 to 80 nm. The nanoparticles used in this work present different sizes as explained in paragraph 4.3.4. However, in both cases, the two type of nanoparticles generated are smaller than the size diameter of the nanofibers. In

the case of the NiNP-NHCs their size is bigger than the height of the step edges. In general, three different cases can be spotted when GNFs and nanoparticles interact to generate hybrid systems. Firstly, the step edges are too small compared to the nanoparticles size, and this hinders the possibility to anchoring the nanoparticles at the edges. Secondly, the step edge is too big compared to the nanoparticles size creating weak electrostatic interaction between the two, hindering the anchoring of the nanoparticles at the GNFs step edges. Thirdly, the step edges size is comparable to the nanoparticles size matching a favourable electrostatic interaction with the GNF step edges.

The contact surface between nanoparticles of different size and the step edges of the nanofibers is generated by van der Waals and electrostatic interactions.[12, 11] This is the reason why the three situations listed above present three different outcomes. The corrugated walls of the GNF follow a certain periodicity represented by the step edges as anchoring points for the nanoparticles.[30] The step edge allows the anchoring of the particle towards two directions in respect of the GNF‘s main axis. The first direction is parallel to the main axis as the step edge can accommodate several small particles as shown in Figures 4.17a and 4.19a. The second direction is perpendicular to the main axis as shown in Figure 4.19b, forming linear arrangement as highlighted by the rectangles. In both cases the most efficient interaction is when the size of the particles matches the geometry of the step edge Figure 4.17a and 4.19 a-b.

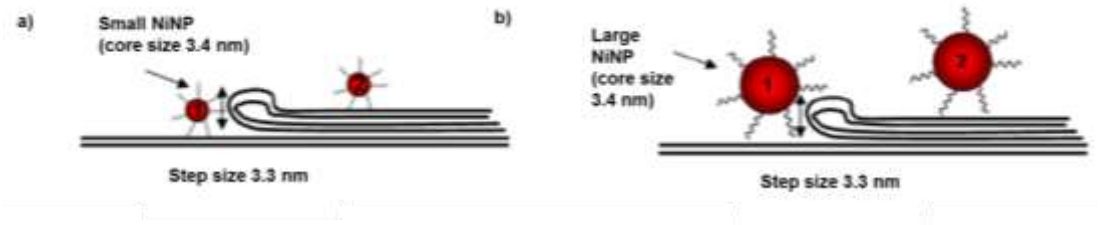


Figure 4.17 Section of GNF step edge: two dimensional representations of a three dimensional structure. Representation of TOP and NHCs NiNPs of different sizes located at the internal step edges of a GNF: a) the NP at the step edge presents a high surface area in contact with the GNF compared to the NP deposited on a flat area; b) the NP at the step edge present limited surface area of contact due to the comparable size in comparison with the diameter of the nanoparticle. The perfect match between NPs and GNF is achieved when the height of the step edge is comparable to the NPs size.

4.4.1 Insertion of nickel nanoparticles into graphitised nanofibers

The Ni-NPs stabilised with TOP are encapsulated in GNF via capillary filling. As it has been briefly discussed in the introduction of this chapter, the GNF present an irregular interior corrugated surface. The GNF step edges present the most favourable morphology for the attachment of NiNP-TOPs as the particles average size diameter 3.4 nm ± 0.7 nm matches the height of the step edges 3.4 nm. As received GNF were heated at 500 °C for 30 minutes in air and then added to a suspension of NiNP-TOPs in a round bottom flask under atmosphere of Argon. The pressure inside the flask was cycled between 10^{-3} mbar and atmospheric pressure a total of three times and the resultant mixture vigorously stirred for 24 hours, Figure 4.18.[54,55]



Figure 4.18 Schematic representation of the filling of NiNPs into GNF via capillarity forces.

The material characterisation is completed by TEM, imaging to investigate the mechanistic aspects of the interactions between NiNP-TOPs and the step edges of the GNF. The lengths of the GNF vary and consequently the total NPs distribution

versus area varies. The NiNP-TOPs samples present a homogeneous distribution at the step edges alongside the two preferential directions arrowed in Figure 4.19 a, and highlighted with the two rectangles in Figure 4.19b.

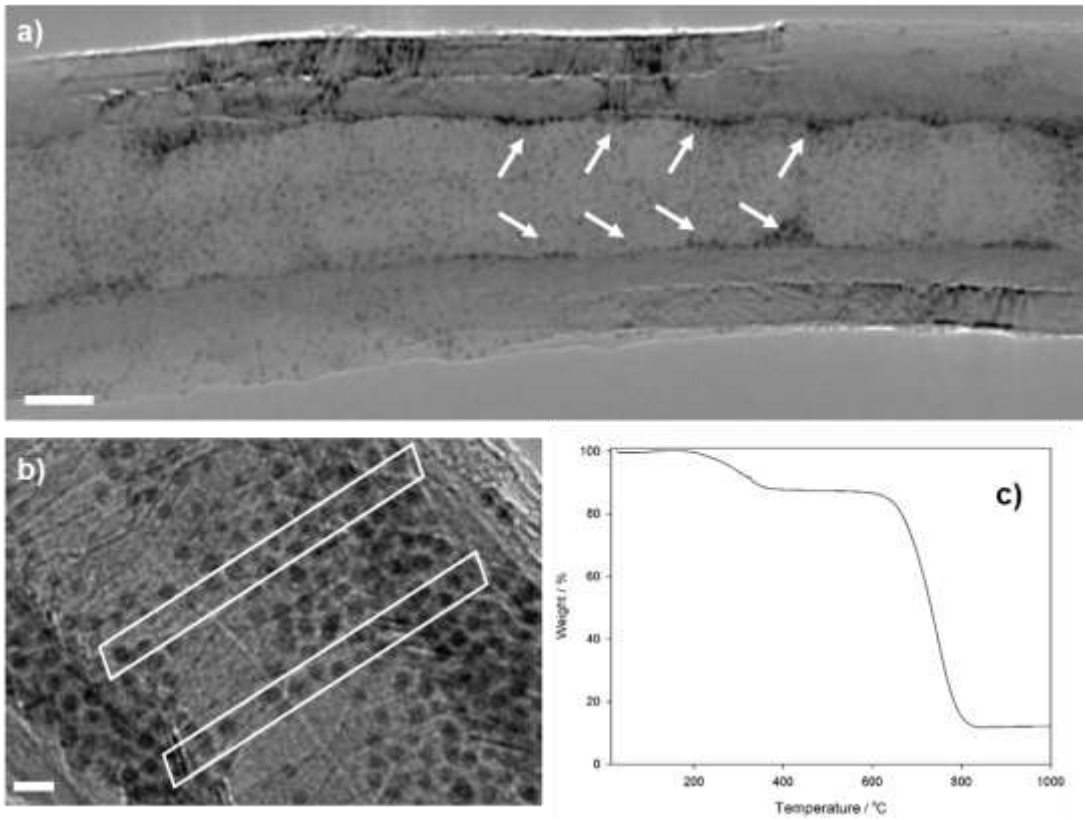


Figure 4.19 a) BF-TEM image of Ni-NPs into GNF. The white arrow indicate the step edges formed by stacked cups suitable as anchoring points for the NP. b) BF-TEM image of NiNPs residing within the cavities of GNF the two rectangular features highlight the particle residing along the step edges. c) TGA of NiNP-TOPs@GNF where the onset temperature is at 741 °C with 44 % of left specimen and T_f is 845 °C with 10 % left of the sample which corresponds to the Ni.

As the interaction between NiNPs and GNF are based upon van der Waals forces driven by the contact surfaces and electrostatic interactions driven by the thickness of the step edges.[12] The concentration of the NiNPs inside the GNF is higher at the proximity of the step edges and lower along the interior wall of the GNF. The entity of the enhanced interactions between the nanoparticle and the GNF can also be explained in terms of host guest interaction in which a quasi-snug fit scenario can be envisaged at the step edges. As it can be seen by the 2D projection, Figure 4.19 a-b a small amount of NiNPs is located on the external surface of the GNFs. The acetone molecules play a crucial role as lubricant (Surface tension of acetone is 25.20 N/m^2 at 20 °C) facilitating the surface diffusion and transport of the NiNPs

from the exteriors to the interiors of the GNFs.[28] The Thermal gravimetric analysis shows the decomposition of the organic capping layer which corresponds to the onset peak at 344 °C with weight loss of 11 % for the NiNP-TOP@GNF. The presence of the metal in the NiNPs is 12 % demonstrated by the residual at 825 °C, Figure 4.19 c).

4.4.2 Insertion of NiNPs stabilised by N-Heterocyclic carbene into graphitised nanofibers

The NiNPs are encapsulated inside the GNF via capillary filling as described above, Paragraph 4.4.1. The GNF used are the PR-19 which show an inner corrugated and irregular surface of graphene layers. As discussed above, paragraph 4.3.3, the NiNPs present a core diameter of 15 ± 4.4 nm significantly larger than the size of the internal step-edge of the GNF which is approximately 3.3 nm. The NiNP-NHCs do not present a favourable morphology for anchoring them at the GNFs step edges. These assumptions are evaluated with TEM imaging which allows a complete material characterisation, Figure 4.20.

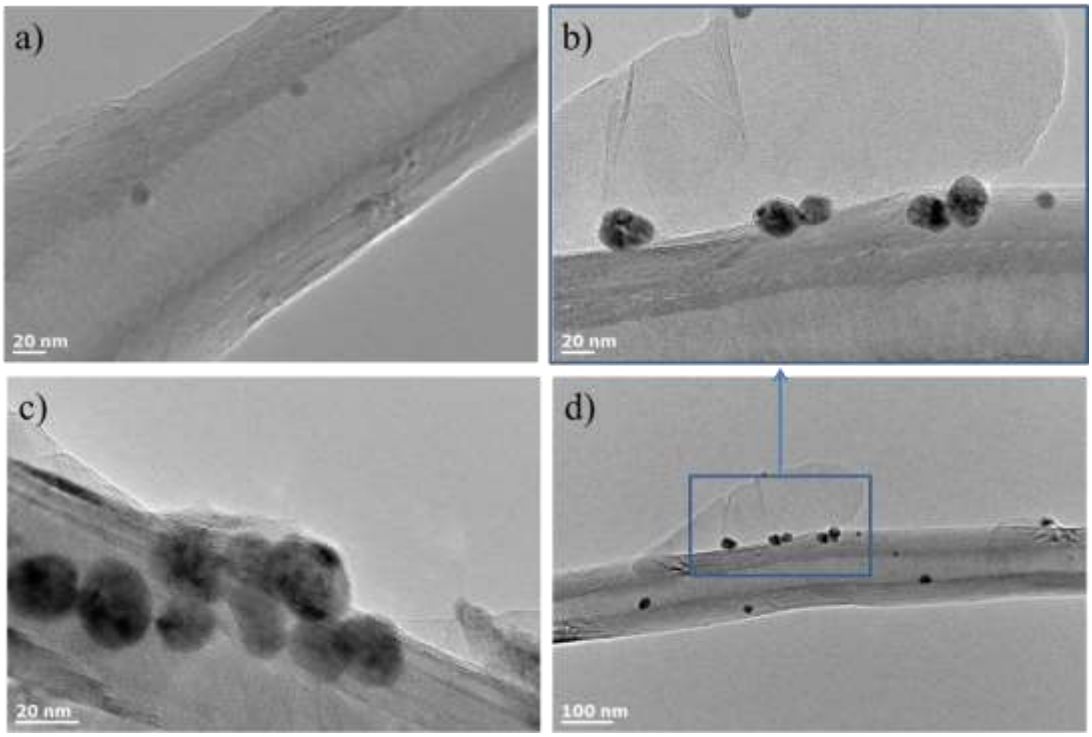


Figure 4.20 a) BF-TEM image of NiNPs inside GNF. b) BF-TEM of NiNPs residing on the external graphitised surface;(high magnification of the rectangle in figure d as shown by the blue arrows; c) BF-TEM image of NiNPs with a diameter of 23.4 ±4.5 nm residing on the outer surface of GNFs; d) BF-TEM of GNF where the NiNPs are randomly distributed on the GNF outer surface. Scale bars are 20 nm (a), 20 nm (b), 20 nm (c) and 100 nm (d).

In opposition to the high concentration of the NiNP-TOP observed at the step edges in section 4.4.1, the NiNP-NHCs larger than the step edges present a host-guest interaction less effective. The NiNP-NHCs appears to be outside the GNF and very few of them are seen inside the GNFs. The NiNP-NHCss were solely confined in defective nanofibers in which the channels were obstructed by internal defects as red arrowed in Figure 4.21. They would not be usable as nanoreactors as the channels are obstructed by internal defects.

The tabulated EDX results provide a semi-quantitative view of the elemental composition in units of both weight percent and atomic percent. The results reveal 5 main elements present within the size of field inspection, Table 4.3.

Table 4.3 Tabulated results of the elemental composition in units of both weight percent and atomic percent.

Element	Weight %	Atomic %
C	63.32 ± 0.69	88.58
Cu	25.52 ± 0.59	6.75
Ni	8.12 ± 0.34	2.32
O	1.17 ± 0.19	1.23
Si	1.86 ± 0.16	1.11

The atomic percentage of nickel and oxygen determined with EDX is nearly 2:1. The weight percentage composition and the atomic percentage of the elements present in the sample reveal the presence of carbon, oxygen, nickel, copper (from the TEM grid) and Si (artefact of the EDX detector). The content of oxygen might be due to the formation of some metal oxide on the Nickel nanoparticles surfaces with some contribution from the residual oxygen present in the TEM vacuum chamber and some residual moisture residing on the amorphous carbon support contained in the TEM grid.

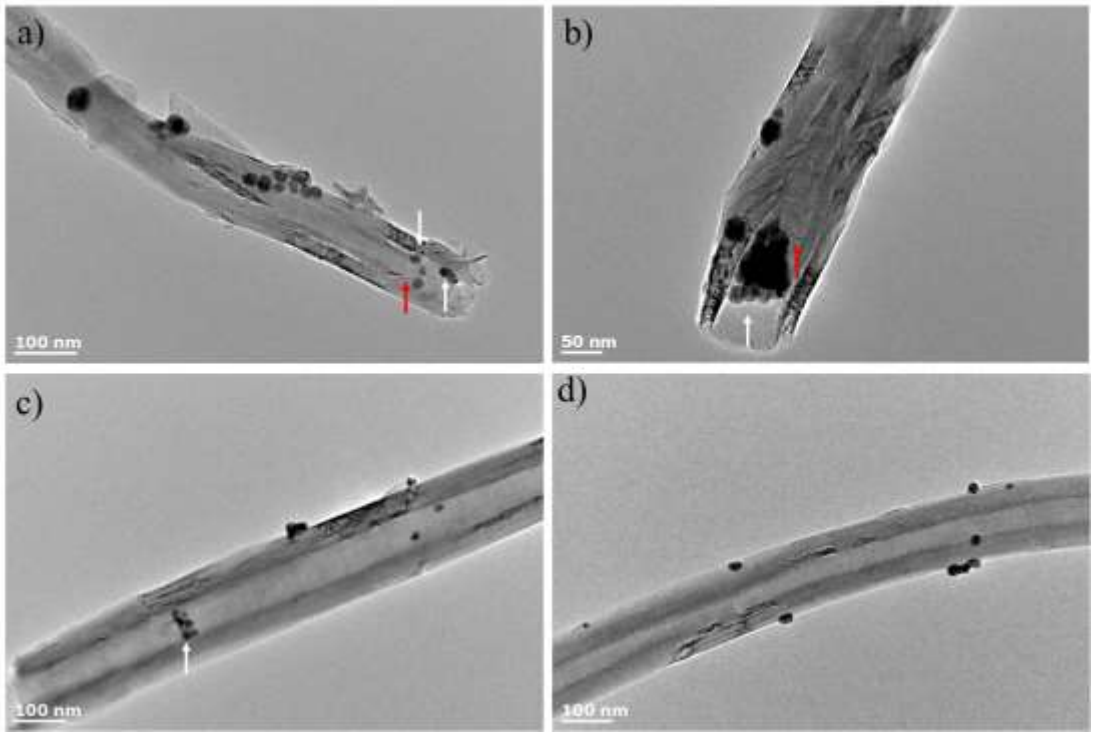


Figure 4.21 a) BF-TEM image of NiNP in and on GNF. The NPs appear randomly distributed; b) and c) BF-TEM image of NiNPs mostly residing in the inner surface of GNFs; d) BF-TEM of NiNPs are solely seen on the external surface. The white

arrow indicates the sporadic examples of particles confined in GNF; presumably they were retained due to internal GNF defects as shown in figures (a) and (b) arrowed in red. The scale bars are 20 nm (a), 20 nm (b), 20 nm (c) and 100 nm (d).

4.4.3 TEM Imaging: EDX mapping on nanoparticles

The EDX mapping allows to detect the percentage of each element present in the NiNPs stabilised by NHCs sample and to combine the separated signals to obtain a composition mapping of the surface.[56] This unique characterisation is run using a High-Angle Annular Dark Field (HAADF) detector in Scanning Transmission Electron Microscopy (STEM) mode. The HAADF-STEM allows imaging the incoherent scattering which gives the image contrast.[57] This analysis allows to unambiguously determining the elemental composition of the particles used.The mapping for nickel and carbon can be clearly seen in the figure represented by the blue pixels and the green pixels, Figure 4.22 b) and d) respectively. The other element seen previously oxygen, silicon and copper are absent in the NiNPs inspection field the only two elements present are nickel and carbon indicated as “Ni on NP” and “C on NP”, Figure 4.22 b) and d) respectively.

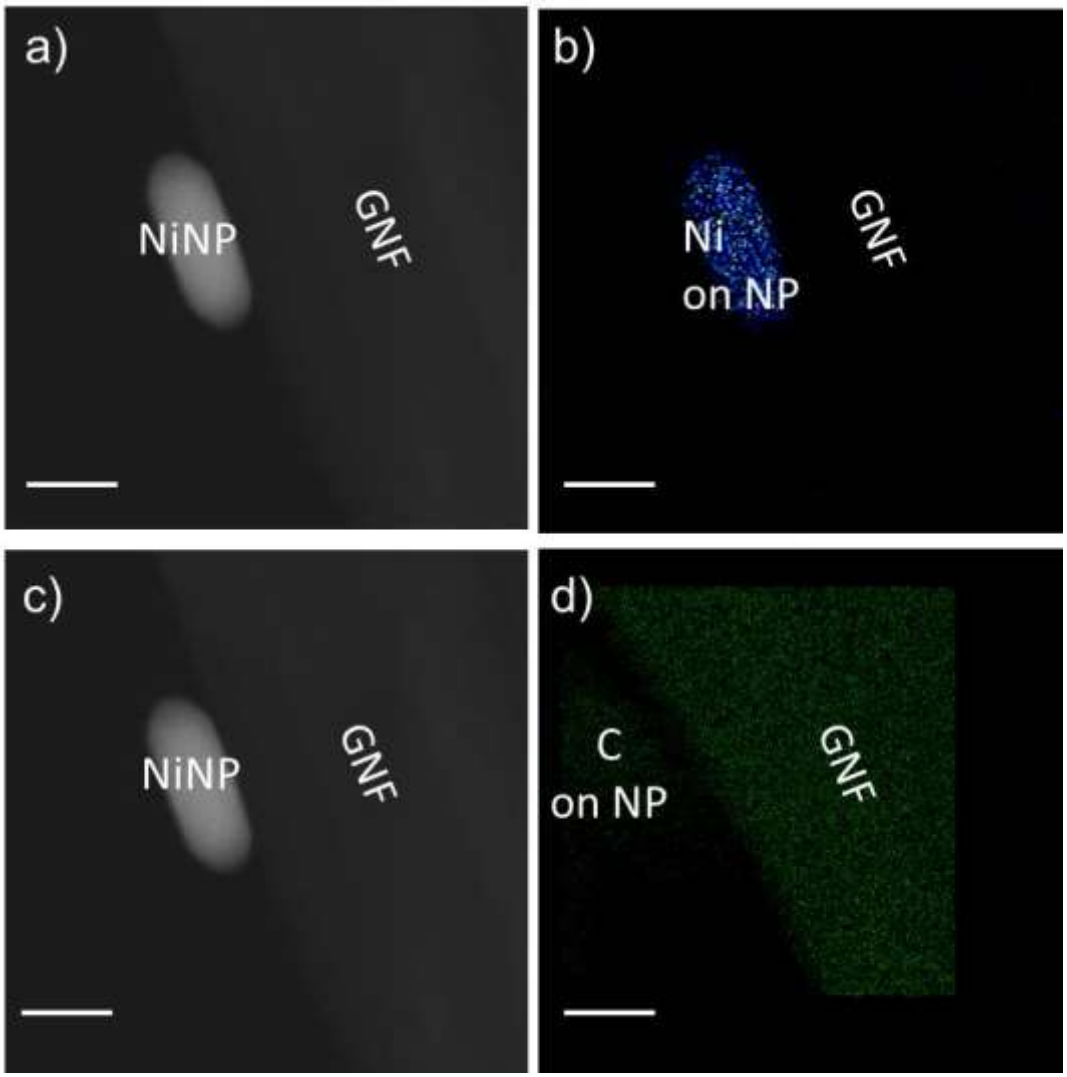


Figure 4.22 HAADF-STEM of the nickel nanoparticles residing at the edge of the GNF (a-c). Elemental distribution of Ni (b) and C (d); The EDX mapping shows the presence of metallic nickel and carbon in the area in which the particle is observed in the imaging b and d respectively. Oxygen was not detected in the proximity of the particles and GNF.

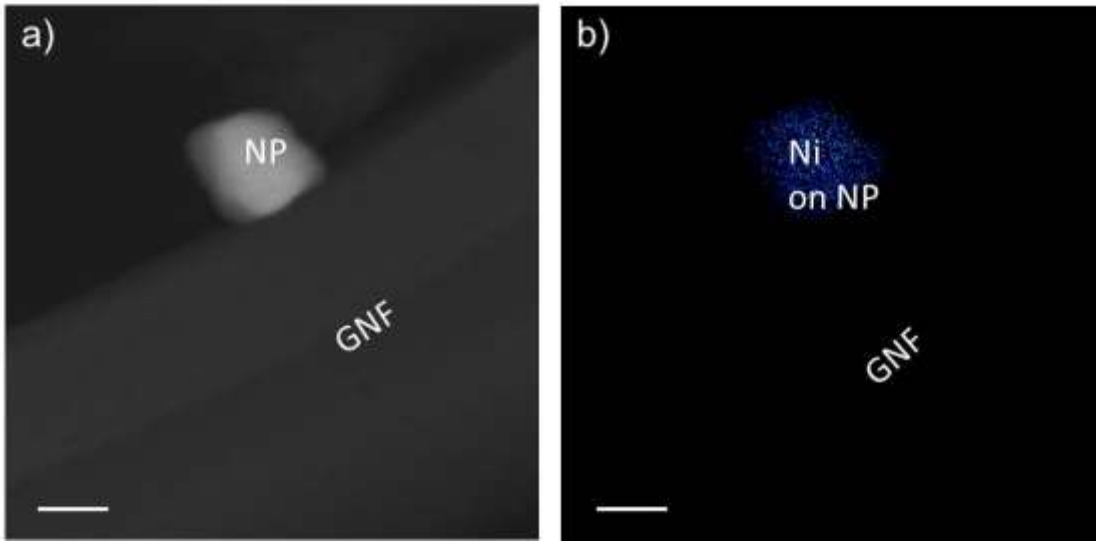


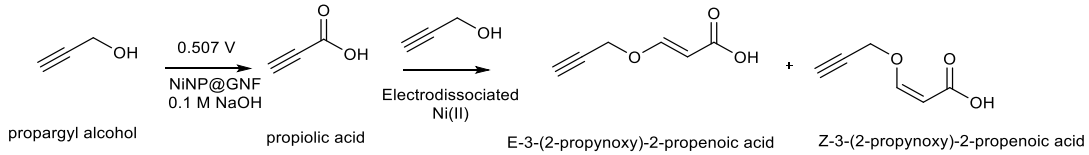
Figure 4.23 a) HAADF-SEM of the nickel nanoparticles residing at the edge of GNF; Elemental phase distribution of nickel (b), the presence of metallic nickel in the area is highlighted by the blue dots.

Again, the EDX mapping of another nanoparticle shows the presence of nickel in the area in which the particle resides. The EDX mapping clearly matches the outcome observed for the IR spectrum for NiNP-NHCs. The combination of these complementary spectroscopic techniques have confirmed the metallic nature of NiNP-NHCs.

4.5 Electrochemical nanoreactor: The proof of concept

There is an urgent need to address the complete control over reaction pathways to selectively obtain the desired product.[58] One of the major challenge in organic chemistry is to open new synthetic strategies to target new molecules and important building blocks.[59] Nowadays, at the forefront of current research routes, there are highly selective catalyst based on complex multi-steps synthetic procedure, and expensive starting materials, which hinder their exploitation and affect their sustanaibility.[60,61] These challenges might be overcome with the replacement of precious metals with sustainable elements, and the development of reaction in confined spaces.[33,32] Nickel due its relatively low cost and toxicity compared to other precious metal used in catalysis might represent a real sustainable alternative. In addition, the use of a carbon support for nickel might maximise its catalytic activity, reusability and recyclability.[62]

The reaction pathways investigated in this work is the oxidation of propargyl alcohol (PGA), Scheme 4.3.



Scheme 4.3 Nickel catalysed electrochemical oxidation of propargyl alcohol to propiolic acid, and subsequent alkoxy migration catalysed by electro dissociated nickel (II) cations to form both E- and Z- isomers of 3-(2-propynoxy)-2-propenoic acid.

The reaction involves the oxidation of PGA to propiolic acid that reacts through an intermolecular mechanism to be rearranged to form both E- and Z- isomers of 3-(2-propynoxy)-2-propenoic acid.[33] The reaction evolves inside the graphitised nanofibers and the confinement of the reactants lead the reaction to two consecutive rearrangements from intermolecular to intramolecular mechanism. The effect of the confinement on a reaction pathways has been studied before.[32] Moreover, different supports show different yields.

4.5.1 Testing the catalytic activity of the nickel nanoparticles for the oxidation of propargyl alcohol

In order to test the catalytic activities of the NiNPs two types of nanoreactors were used. All materials were prepared using methods reported in paragraphs 4.3 and 4.4. The encapsulation procedure relies on capillary filling and is described in

paragraph 4.4.1. The first system investigated was the TOP stabilised nanoparticle in GNF PR24 (NiNP-TOPs@GNF). The nickel loading for NiNP-TOPs@GNF was quantified by thermogravimetric analysis TGA, Figure 4.24 and estimated to be 11.8 %.

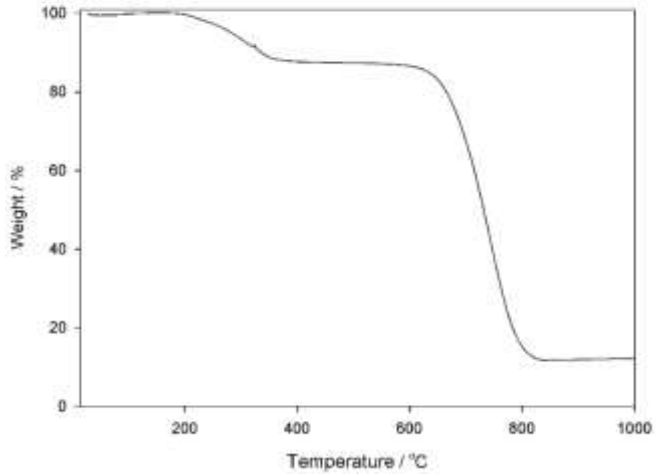


Figure 4.24 TGA of NiNP-TOPs@GNF of y in Weight percentage over x in degree, the weight percentage of residual NiNP is estimated to be 11.8 %; Measurements were conducted in air at a rate of 10 °C·min^{-1} up to 1000 °C.

The TGA shows two steps thermal decomposition profile Tp1 which correspond of a weight loss of 7.48 % at 309.76 °C and Tp2 which correspond of a weight loss of 54.73 % at 739.34 °C. At a temperature higher than 800 °C the weight loss reach a plateau which correspond to 88.2 %.

The vast majority of nanoparticles appear to be inside the GNF and only a minority of them are present on the outer layer which influence the catalytic activity of the nanoreactor.[11] EDX show the elemental composition of the NiNP-TOPs anchored to the graphitic step edges surface, Figure 4.25.

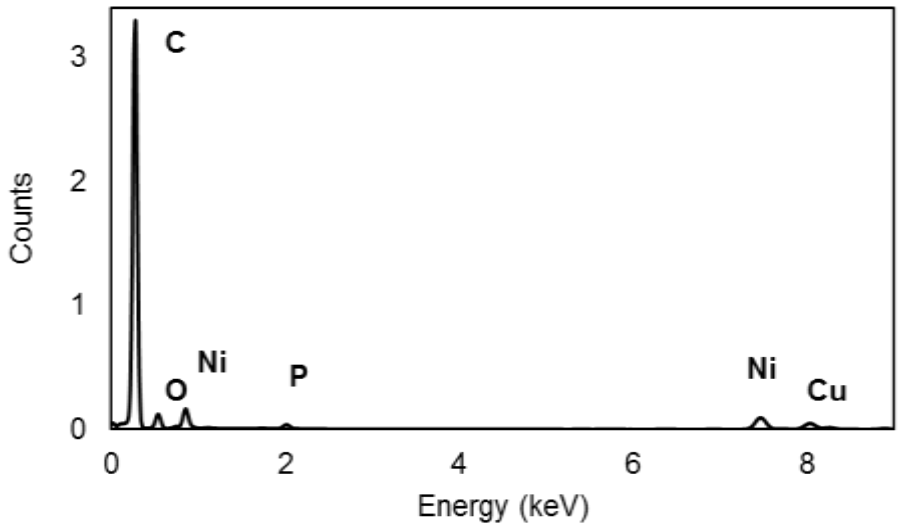


Figure 4.25 EDX spectrum of the NiNP-TOPs@GNF showing the presence of nickel. copper is due to the TEM sample grid.

In order to show the catalytic activity of the first system investigated (NiNP-TOPs@GNF), it was tested the electrochemical response of an alkali solution containing propargyl alcohol (PGA). Cyclic voltammetry (CV) measurements of the sample deposited onto a glassy carbon electrode soaked in an alkali solution containing PGA demonstrated a clear electrochemical response at 0.570V. The increment in current shown as a peak corresponds to the oxidation of PGA to propiolic acid (PA), Figure 4.23. The concentration of PGA was gradually increased to confirm the position of the electrochemical response, Figursc.

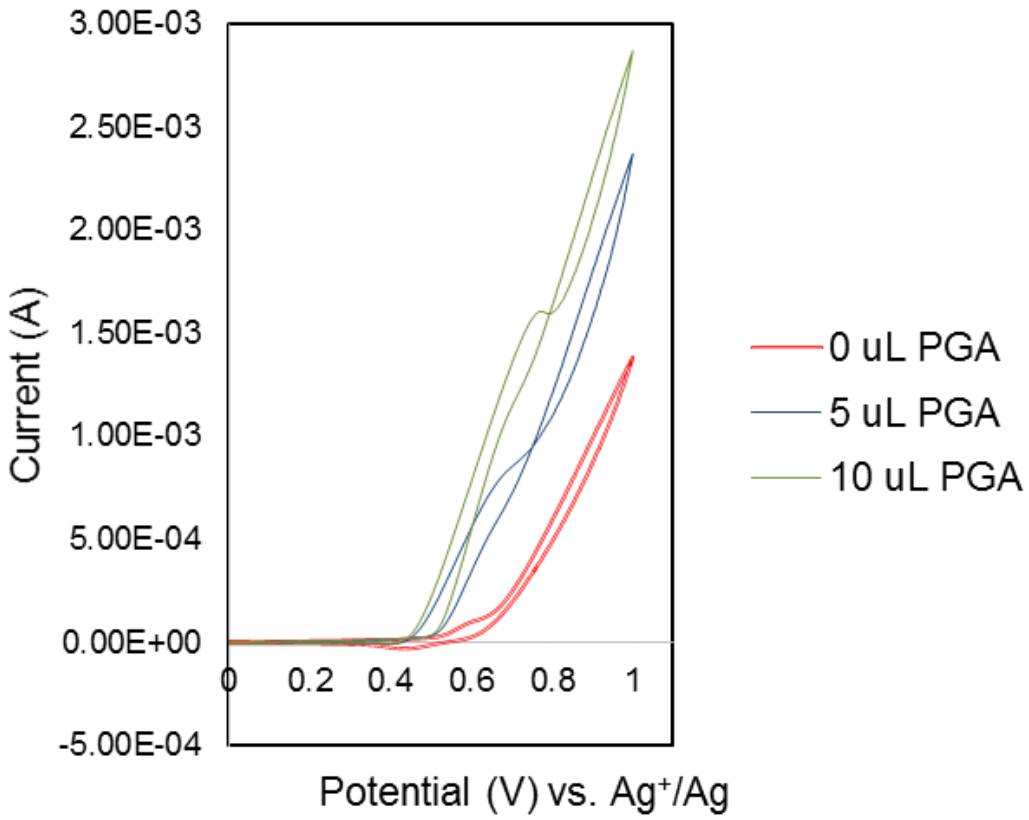


Figure 4.26 Cyclic voltammetry (CV) measurements of the sample deposited onto a glassy carbon electrode immersed in an alkali solution containing PGA demonstrated a clear electrochemical response at 0.570V.

To confirm the catalytic response of the NiNPs in GNF was carried out a control experiment with empty GNF. In this case no electrochemical response was observed. Therefore, 0.570 V was used as an oxidation potential for the electro catalytic reaction on nickel centres for the supported NiNPs in the preparative reactions.

The second system NiNP-NHCs@GNF was also investigated (TGA and EDX analysis are reported in the appendix). It has been found out that the effect of the nickel nanoparticles stabiliser might plays a key role on the catalytic activity. In addition, the NiNP-TOPs@GNF and NiNP-NHCs@GNF results (Table 4.4, rows 3 and 4) were compared to the tests carried by Garcia-Cruz who described the use of a nickel-carbon composite catalyst NiNP/C-Black for the electro catalytic oxidation of propargyl alcohol (Table 4.4, rows 1 and 2).

Table 4.4 Reactant conversion and product distribution for electro catalytic oxidation of propargyl alcohol comparison with value reported in the literature 1-2 rows) 3-were performed with 2.25 mmol of PGA in 30ml 0.1M aqueous NaOH solution.

Material	Ni [wt %]	PGA conversion [%]	Product Distribution [%]		
			PA	**E-PPA**	**Z-PPA**
NiNP/C-Black[33] *****	6.7	81	0	7	93
NiNP/C-Black[33] *****	20.0	81	0	2	98
NiNP-TOP@GNF	9.2	60	100	0	0
NiNP-NHCs@GNF	14.5	-	-	-	-

*Summary of the electrolysis products ratios Z-PPA: E-PPA : PA obtained from the electrooxidation of PGA at NiNP/C Black electrode. 250 mM PGA starting concentration. Electrosynthesis were performed at 0.540 V vs Ag/AgCl. Geometric area of the electrode: 3.8 x 3.8 cm^2.

The system proposed by Garcia mainly produced the Z-PPA product. Conversely the NiNP-TOPs system has shown the PGA to be the only product obtained with a yield of 100%. In the case of NiNP/C-Black the Ni(II) promoted mainly the second step of the reaction, hence E-PPA and Z-PPA respectively. In the NiNP-TOPs@GNF system the stabiliser creates a coating layer which prevents the oxidation of the NiNP, hence, the second step of the reaction which would be generated by the presence of Ni(II) does not occur. In the case of NiNP-NHCs@NiNPs even the first step of the reaction does not take place.

The first observation is the dependence of the products on the loading of NiNP/C-Black. In the values reported from Garcia-Cruz the highest concentration of Ni(II) in NiNP/C-Black produces the highest yield in the second step of the reaction. By contrast, the metallic nature of the particles stops the reaction to the first step which consolidates the previous assumption of the high stability of NiNP-TOPs. Hence, the second step of the reaction which would be generated by the presence of Ni(II) does not occur. The capping layer creates a coating layer which prevent the oxidation of the NiNPs. The interactions of organic molecules within the cavities of GNF increases the local concentration of reacting molecules.[12] The formation of the acid is driven by thermodynamic and mechanistic forces enhance by the nanoconfinement. In addition the step-edges of GNF create a pocket acting as a nano-electrode that conveys electrons to/from the reacting molecules trapped inside due to the lipophilic nature of the graphic surfaces. Organic substrates are spontaneously attracted into the hydrophobic space of the GNF from an aqueous

solution where are dispersed the electrolytes. The graphic surface of the GNF is recognised as one of the most conductive material in the world and is an ideal environment for electro catalysis.

It was expected for the bulky capping layer (NiNP-NHCs@GNF) nanoparticles to present negligible catalytic activity as the NHCs carbene might poison the catalyst.[63] By contrast, it has been found that NiNP-TOPs@GNF present catalytic activity as TOP is a less bulky capping layer. Moreover, they offer a suitable platform for the reaction of oxidation of PGA and they are extremely selective for the product. The catalytic side of NiNP-TOPs is not accessible for another molecule of PGA to attack the acid. Hence, the reaction is stopped at the first step. As the second step does not take place due to the absence of Ni(II), therefore the NiNP-TOPs are not oxidised and the nickel is purely metallic. The presence of the nanoparticles at the GNF step edges is responsible for the confinement effect which influence the reaction. The GNF act as a polarised electrode.

4.6 Summary and future work

In conclusion, the synthesis and characterisations of Ni-NHCs and Ni-TOPs are reported. ***The synthesis and characterization of NiNP-TOPs has been optimised.*** Park *et al* claim the presence of nickel monoxide in NiNP-TOPs using the same reaction conditions. Conversely, in this thesis, it has been shown via an electro-catalytic reaction the metallic nature of Ni-TOPs. Complementary spectroscopic techniques, has also revealed the metallic nature of the Ni-TOPs and the presence of the P on the external layer of NiNP-TOPs. In the case of Ni-NHCs, it has been shown for the first time the synthesis of metallic Ni-NHCs characterized by HAADF-STEM and IR. The thermogravimetric analysis allows insight into the long-term thermal decomposition behaviours of the NiNPs samples reflected by the high decomposition temperature. All the samples are analysed in air to determine the oxidative process. The weight percentage of residual NiNP-TOPs is estimated to be 9 % whereas the weight percentage of residual NiNP-NHCs is estimated to be 14 %. The insertion of NiNPs into GNF is performed under vacuum. The acetone used as solvent acted as a lubricant to facilitate the distribution of the NiNPs.[28] The anchoring of the NiNPs to the GNF step edges is associated to the host-guest interaction which is correlated to the diameter of the nanoparticles. As result, the positional control is induced only generating nanoparticles of well-ordered size. In fact, only NiNPs with a diameter smaller than the graphitic step-edges find the favourable geometry to achieve the best interactions. The EDX analysis allows to determine the composition of the NiNPs surface which is mostly made of Ni and some C. The IR analysis for the two particles allows confirming the presence of metallic NiNPs due to the absence of the characteristic Ni-O stretching peak expected at 522 and 450 cm^{-1} a clear indication that the NiNPs are purely metallic with an organic protecting layer.

In this chapter an example of electro catalysis by NiNPs@GNF has been demonstrated, showing the catalytic activity of the encapsulated capped nanoparticles in the oxidation of propargyl alcohol (PGA). The reaction demonstrated the correlation of the selectivity of the reaction imposed by nanoscale confinement. By encapsulating the catalyst is possible to tune the reaction pathway stopping the reaction of the PGA oxidation at the first step. Remarkably, the results show the importance of both nanoconfinement and presence of capping layer. The host-guest interaction between NiNPs and GNF is enhanced by the electro catalytic reaction which proves the presence of capping layer as a protective agent against the oxidation of the nanoparticle. In fact, the second step of the reaction is driven by the high concentration of Ni(II) which seems not the case. The presence of the step-

edges seems act as confinement for the substrates effect that is enhanced in the case of Ni-TOP and it would be absent in the case of Ni-NHCs too big compared to the step edge.

In the future, it would be interesting to ripen the Ni-TOPs to the same size of the Ni-NHCs to confirm the hypothesis that NiNP-TOPs@GNF possesses a higher catalytic activity than NiNP-NHCs@GNF simply because of a much larger electrochemically active surface area of smaller NiNP-TOPs. Another hypothesis is based on the NHCs carbene which might poison the catalyst as already observed for $[C_1OC_2mim][Tf_2N]$ with metal complex catalyst.[64,1]

4.7 Bibliography

1 J. Dupont and L. Kollár, *Ionic Liquids (ILs) in Organometallic Catalysis*, Berlin, Heidelberg, Springer., 2015.

2 W. Chen, J. R. Davies, D. Ghosh, M. C. Tong, J. P. Konopelski and S. Chen, *Chem. Mater.*, 2006, **18**, 5253–5259.

3 M. H. G. Prechtl, P. S. Campbell, J. D. Scholten, G. B. Fraser, G. Machado, C. C. Santini, J. Dupont and Y. Chauvin, *Nanoscale*, 2010, **2**, 2601–2606.

4 C. Roukoss, S. Fiddy, A. de Mallmann, N. Rendón, J.-M. Basset, E. Kuntz and C. Copéret, *Dalt. Trans.*, 2007, 5554–5560.

5 L. S. Ott, M. L. Cline, M. Deetlefs, K. R. Seddon and R. G. Finke, *J. Am. Chem. Soc.*, 2005, **127**, 5758–5759.

6 T. Tu, W. Assenmacher, H. Peterlik, G. Schnakenburg and K. H. Dötz, *Angew. Chemie - Int. Ed.*, 2008, **47**, 7127–7131.

7 T. Tu, W. Assenmacher, H. Peterlik, R. Weisbarth, M. Nieger and K. H. Dötz, *Angew. Chemie Int. Ed.*, 2007, **46**, 6368–6371.

8 J. Park, E. Kang, S. U. Son, H. M. Park, M. K. Lee, J. Kim, K. W. Kim, H. J. Noh, J. H. Park, C. J. Bae, J. G. Park and T. Hyeon, *Adv. Mater.*, 2005, **17**, 429–434.

9 M. Endo, Y. A. Kim, T. Hayashi, Y. Fukai, K. Oshida, M. Terrones, T. Yanagisawa, S. Higaki and M. S. Dresselhaus, *Appl. Phys. Lett.*, 2002, **80**, 1267–1269.

10 Y. Zhao, C. Li, K. Yao and J. Liang, *J. Mater. Sci.*, 2007, **42**, 4240–4244.

11 A. La Torre, M. W. Fay, G. A. Rance, M. Del Carmen Gimenez-Lopez, W. A. Solomonsz, P. D. Brown and A. N. Khlobystov, *Small*, 2012, **8**, 1222–1228.

12 A. La Torre, M. del Carmen Gimé nez-Ló pez, M. W. Fay, G. A. Rance, W. A. Solomonsz, T. W. Chamberlain, P. D. Brown and A. N. Khlobystov, *ACS Nano*, 2012, **6**, 2000–2007.

13 C. A. Bessel, K. Laubernds, N. M. Rodriguez and R. T. K. Baker, *J. Phys. Chem. B*, 2001, **105**, 1115–1118.

14 T. W. Chamberlain, T. Zoberbier, J. Biskupek, A. Botos, U. Kaiser, A. N. Khlobystov, A. Merigo, G. F. Strouse, H. W. Kroto and S. F. A. Acquah, *Chem. Sci.*, 2012, **3**, 1919–1924.

15 S. Carenco, C. Boissière, L. Nicole, C. Sanchez, P. Le Floch and N. Mézailles, *Chem. Mater.*, 2010, **22**, 1340–1349.

16 C. B. Murray, S. Sun, H. Doyle and T. Betley, *MRS Bull.*, 2001, **26**, 985–991.

17 M. Green and P. O ’Brien, *Chem. Commun.*, 2001, 1912–1913.

18 L. Chen, J. Chen, H. Zhou, D. Zhang and H. Wan, *Mater. Sci. Eng. A*, 2007, **452**–**453**, 262–266.

19 H. T. Zhang, G. Wu, X. H. Chen and X. G. Qiu, *Mater. Res. Bull.*, 2006, **41**, 495–501.

20 A. La Torre, F. Ben Romdhane, W. Baaziz, I. Janowska, C. Pham-Huu, S. Begin-Colin, G. Pourroy and F. Banhart, *Carbon N. Y.*, 2014, **77**, 906–911.

21 J. Jiao and S. Seraphin, *J. Appl. Phys.*, 1998, **83**, 2442–2448.

22 V. S. Budhiraju, R. Kumar, A. Sharma and S. Sivakumar, *Electrochim. Acta*, 2017, **238**, 337–348.

23 A. M. Bazargan, M. Esmaeilpour and M. Keyanpour-rad, *J. Nanostructures*, 2016, **6**, 52–57.

24 X. Wu, W. Xing, L. Zhang, S. Zhuo, J. Zhou, G. Wang and S. Qiao, *Powder Technol.*, 2012, **224**, 162–167.

25 P. M. Mortensen, J.-D. Grunwaldt, P. A. Jensen and A. D. Jensen, *Catal. Today*, 2016, **259**, 277–284.

26 S. R. Challa, A. T. Delariva, T. W. Hansen, S. Helveg, J. Sehested, P. L. Hansen, F. Garzon and A. K. Datye, *J. Am. Chem. Soc.*, 2011, **133**, 20672–20675.

27 A. Heilmann and J. Werner, *Thin Solid Films*, 1998, **317**, 21–26.

28 A. La Torre, G. A. Rance, J. El Harfi, J. Li, D. J. Irvine, P. D. Brown and A. N. Khlobystov, *Nanoscale*, 2010, **2**, 1006–1010.

29 G. Rosenfeld, K. Morgenstern, I. Beckmann, W. Wulfhekel, E. Lægsgaard, F. Besenbacher and G. Comsa, *Surf. Sci.*, 1998, **402**, 401–408.

30 A. La Torre, M. del Carmen Gimenez-Lopez, M. W. Fay, C. H. Lucas, P. D. Brown and A. N. Khlobystov, *Small*, 2015, **11**, 2756–2761.

31 T. W. Hansen, A. T. DeLaRiva, S. R. Challa and A. K. Datye, *Acc. Chem. Res.*, 2013, **46**, 1720–1730.

32 M. A. Lebedeva, T. W. Chamberlain, A. Thomas, B. E. Thomas, C. T. Stoppiello, E. Volkova, M. Suyetin and A. N. Khlobystov, *Nanoscale*, 2016, **8**, 11727–11737.

33 L. García-Cruz, A. Sáez, C. O. Ania, J. Solla-Gullón, T. Thiemann, J. Iniesta and V. Montiel, *Carbon N. Y.*, 2014, **73**, 291–302.

34 Y. Leng, Y. Zhang, T. Liu, M. Suzuki and X. Li, *Nanotechnology*, 2006, **17**, 1797–1800.

35 N. Chopra, L. Claypoole and L. G. Bachas, *J. Nanoparticle Res.*, 2010, **12**, 2883–2893.

36 M. Han, Q. Liu, J. He, Y. Song, Z. Xu and J. M. Zhu, *Adv. Mater.*, 2007, **19**,

1096–1100.

37 V. Tzitzios, G. Basina, M. Gjoka, V. Alexandrakis, V. Georgakilas, D. Niarchos, N. Boukos and D. Petridis, *Nanotechnology*, 2006, **17**, 3750–3755.

38 T. Hinotsu, B. Jeyadevan, C. N. Chinnasamy, K. Shinoda and K. Tohji, *J. Appl. Phys.*, 2004, **95**, 7477–7479.

39 C. N. Chinnasamy, B. Jeyadevan, K. Shinoda, K. Tohji, A. Narayanasamy, K. Sato and S. Hisano, *J. Appl. Phys.*, 2005, **97**, 10J309.

40 S. Mourdikoudis and L. M. Liz-Marzán, *Chem. Mater.*, 2013, **25**, 1465–1476.

41 S. N. Sharma, H. Sharma, G. Singh and S. M. Shivaprasad, *Mater. Chem. Phys.*, 2008, **110**, 471–480.

42 B. Fultz and J. Howe, *Transmission Electron Microscopy and Diffractometry of Materials*, Berlin, Heidelberg, Springer., 2008.

43 A. Michalcová, P. Svobodová, R. Nováková, A. Len, O. Heczko, D. Vojtěch, I. Marek and P. Novák, *Mater. Lett.*, 2014, **137**, 221–224.

44 M. Salavati-Niasari, N. Mir and F. Davar, *J. Alloys Compd.*, 2010, **493**, 163–168.

45 A. Kumar, A. Saxena, A. De, R. Shankar and S. Mozumdar, *Adv. Nat. Sci. Nanosci. Nanotechnol.*, 2013, **4**, 1–9.

46 A. Kraynov and T. E. Müller, *Concepts for the Stabilization of Metal Nanoparticles in Ionic Liquids*, Rijeka (Croatia), InTech., 2011.

47 Y. Chen, D.-L. Peng, D. Lin and X. Luo, *Nanotechnology*, 2007, **18**, 505703.

48 S.-H. Wu and D.-H. Chen, *J. Colloid Interface Sci.*, 2003, **259**, 282–286.

49 P. Song, D. Wen, Z. X. Guo and T. Korakianitis, *Phys. Chem. Chem. Phys.*, 2008, **10**, 5057–5065.

50 F. Cataldo, *Polyynes Synthesis, Ptoperties and Applications*, Boca Raton, CRC Press., 2006.

51 L. J. Bellamy, *The Infrared Spectra of Complex Molecules: Volume Two Advances in Infrared Group Frequencies*, London, Springer., 2012.

52 A. Rahdar, M. Aliahmad and Y. Azizi, *J. Nanostructures*, 2015, **5**, 145–151.

53 F. Davar, Z. Fereshteh and M. Salavati-Niasari, *J. Alloys Compd.*, 2009, **476**, 797–801.

54 Y. Chen, D.-L. Peng, D. Lin and X. Luo, *Nanotechnology*, 2007, **18**, 1–6.

55 A. La Torre, University of Nottingham, 2013.

56 C.-M. Wang, A. Genc, H. Cheng, L. Pullan, D. R. Baer and S. M. Bruemmer, *Sci. Rep.*, 2014, **4**, 3683–3687.

57 S. Utsunomiya and R. C. Ewing, *Environ. Sci. Technol.*, 2003, **37**, 786–791.

58 B. M. Trost and D. L. Van Vranken, *Chem. Rev.*, 1996, **96**, 395–422.

59 S. Hosseyni, Y. Su and X. Shi, *Org. Lett.*, 2015, **17**, 6010–6013.

60 M. P. Carroll and P. J. Guiry, *Chem. Soc. Rev.*, 2014, **43**, 819–833.

61 F. Cavani, *Catal. Today*, 2010, **157**, 8–15.

62 B. Liu, Q. Xia and W. Chen, *Angew. Chemie - Int. Ed.*, 2009, **48**, 5513–5516.

63 X. Yang, Z. Fei, T. J. Geldbach, A. D. Phillips, C. G. Hartinger, Y. Li and P. J. Dyson, *Organometallics*, 2008, **27**, 3971–3977.

64 B. Sjögren, S. Svensson, A. N. de Brito, N. Correia, M. P. Keane, C. Enkvist and S. Lunell, *J. Chem. Phys.*, 1992, **96**, 6389–6398.

Conclusions and future work

In this *Thesis*, the synthesis, characterisation and application of bis(benzimidazolin-2-ylidene) molecules is extensively discussed. The fabrication and characterisation of nanoparticles materials stabilised by ionic liquids have gained interest in recent years.[1] Considerable effort has been devoted to utilise X-Ray Photoelectron Spectroscopy (XPS) to provide information concerning the electronic environment of ILs.[2] Bis(benzimidazolin-2-ylidene) compounds have been used for the first time as a stabiliser for nickel nanoparticles. The capping layer acts as protective layer against the corrosion. It avoids the physical contact between the nanoparticles and the supports in which they reside. This unique morphological feature of the capped nanoparticles can be combined with other nanomaterials to design and realise composite materials possessing advanced functional properties (catalytic, electrical, magnetic, mechanical or chemical). In this work, capped nanoparticles have been anchored at the step edges of GNF to create state of the art nano reactor. As a results of the interaction between guest-species (nanoparticles) and host-species (GNF) different synergic property has arisen. Two types of capped nanoparticles, NiNP-TOPs and NiNP-NHCs have been compared for the electrochemical oxidation of propargyl alcohol. Solely NiNP-TOPs show catalytic activity for the reaction which yielded 60% product.

The thesis contributes to this area of research on four different levels. The first aim is to develop and validate the deconstruction of the C1s region for a series of bis(benzimidazolin-2-ylidene) ionic compounds based upon previous work which developed the fitting model for imizadolium-based ILs, pyridinium-based ILs combination of them to create Gemini ILs. The cation-anion interaction is investigated to explain the electronic effect of anion on the cation. A systematic study is carried out for different chain length and anions ILs to confirm the consistency of the model.

The second aim is to understand the fundamental of the mechanism governing the nanoparticles when anchored at the step edges of graphitised nanofibers. There are two preferential sites in which the particles reach their maximum host-guest interaction. The first site is parallel to the main axis and the second site is perpendicular to the main axis. In both cases the most efficient interaction is when the size of the particles matches the geometry of the step edge. The capping layer possesses remarkable ability to isolate the particles to moisture and atmospheric oxygen and avoid the oxidation of the nanoparticles.

The third aim is to show the metallic nature of the capped nanoparticles. Complementary electron and spectroscopy techniques have shown the metal nature

of the particles which maintains their metallic nature post synthesis when constantly exposed to air. In addition, the electrochemical reaction with of NiNP-TOPs@GNF is crucial to unambiguously confirm the metallic nature of the particles. The lack of nickel(II) stopped the oxidation of propargyl alcohol to acid. In the Ni-NHCs system the combination of EDX mapping, IR and electron diffraction showed the possibility to determine the metallic nanoparticle crystal phase.

The fourth thrust is aimed at showing the natures of the interaction generated between nanoparticles and stabiliser. The capping layer is connected to the surface of the particle via the electrostatic interactions, as it is generally assumed that the approach of negatively charge anions to a metal sphere induce a positive charge on the surface.

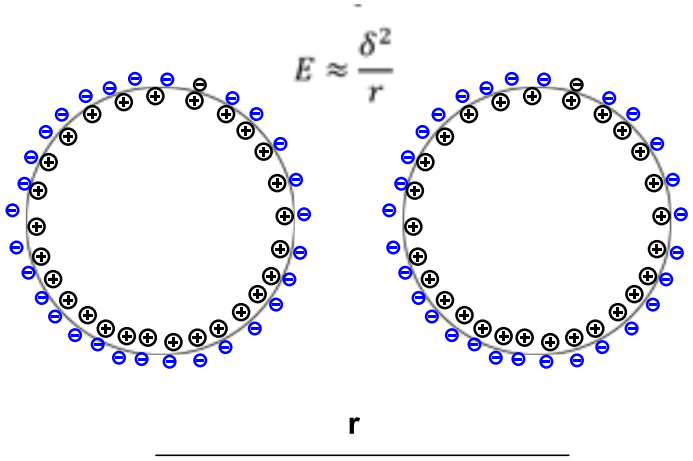


Figure 1 Coulombic repulsion between partly charged particles as the origin of electrostatic stabilization.

In the case of the bis(benzimidazolin-2-ylidene) molecules the surface distribution may be hindered presenting the anion on the external layer of the nanoparticle and the positive charge of the cation outside to form a circle, Figure 2.

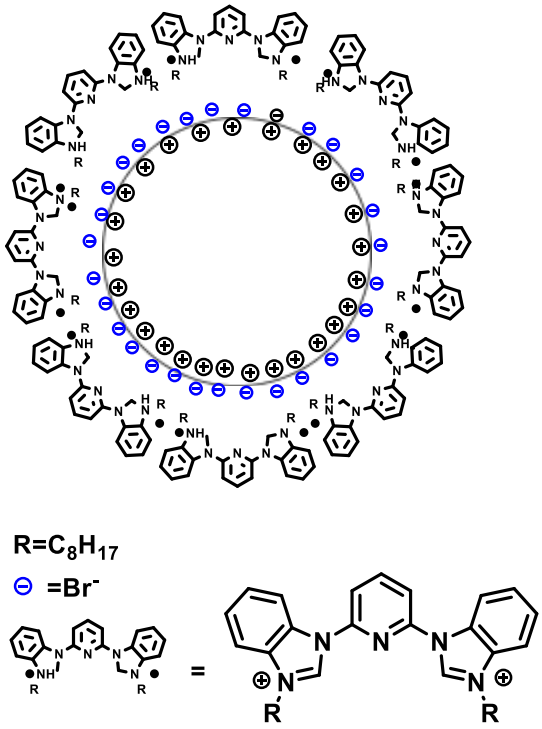


Figure 2, Representation of the nanoparticle stabilised by bis(benzimidazolin-2-ylidene) the centre of the nanoparticle is neutral; the Π-Π stacking interactions contribute to the possibility of having several layers of NHCs on the top of the NHCs molecules electrostatically interacting with the particles.

The size of ion determines the distance from the surface of the nanoparticle and the number of ions around it. Hence, the electrostatic energy of the system varies according to them. When the ions are weakly coordinating (such as in the case of $[Ntf_2]^-$) the interaction energy with the metal nanoparticle is electrostatic and it is influenced by both the particle size and the distance between the particle and the ion.[3] The size of the ion determines also the maximum number of ions around the nanoparticle which also influences and the stability of the nanoparticles. Ions such as halide, used in this work, are high coordinating, hence provide good stabilisation. Also, the cation of ILs plays an important role in the stabilisation of ionic liquids. Important examples are functionalised ILs such as NHCs which enhance stabilisation via a strong coordination well known for many metals. In both cases the chains might be linen on the faceted face of the Ni-NHCs .The supramolecular assembly on the metal nanoparticle core might create a very thick coverage.

The methodology for NiNP-NHCs synthesis has been established. Hence, it can be embraced for a wide range of ionic compounds to generate capped nanoparticles. There are a number of exciting opportunities in catalysis for the application of capped nanoparticles encapsulated in GNF. The reaction path can be controlled

with hindered nanoparticles, opening new possibilities in synthetic chemistry. Moreover interesting electric properties can be studied which may enable to generate nanoscale catalytic devices. The electrical properties of carbon chains can be changed when they are stretched. The length of the chain is responsible to the Ni-NHCs optical properties.[4,5,6]

Bibliography

1 J. Dupont and L. Kollár, *Ionic Liquids (ILs) in Organometallic Catalysis*, Berlin, Heidelberg, Springer., 2015.

2 E. F. Smith, F. J. M. Rutten, I. J. Villar-garcia, D. Briggs and P. Licence, *Langmuir*, 2006, **22**, 9386–9392.

3 A. Kraynov and T. E. Müller, *Concepts for the Stabilization of Metal Nanoparticles in Ionic Liquids*, Rijeka (Croatia), InTech., 2011.

4 A. La Torre, A. Botello-Mendez, W. Baaziz, J.-C. Charlier and F. Banhart, *Nat. Commun.*, 2015, **6**, 6636.

5 B. Pan, J. Xiao, J. Li, P. Liu, C. Wang and G. Yang, *Sci. Adv.*, 2015, **1**, 1–10.

6 F. Cataldo, *Polyynes Synthesis, Ptoperties and Applications*, Boca Raton, CRC Press., 2006.

Appendix

IR spectroscopy of nanoparticle stabilisers (TOP, NHCs), Trioctylphosphine nanoparticles (NiNP-TOPs) and Benzymidazoline nanoparticles (NiNP-NHCs)

Table 1 Indication of different bands and the region in which they appear for NiNP-TOPs and NiNP-NHCs

Band	**Wavelenght (cm^{-1})**
Stretching band of OH group	3330
Asymmetric stretching band of CH_3	2960 (strong)
Symmetric stretching band of CH_3	2870 (overlapped)
Asymmetric stretching band of CH_2	2930 (strong)
Symmetric stretching band of CH_2	2850 (strong)
Bending band of CH_2	1450 (medium)
Bending band of CH_3	1350 (weak)
P=O stretching band	1187
Rocking band due to long chains	730

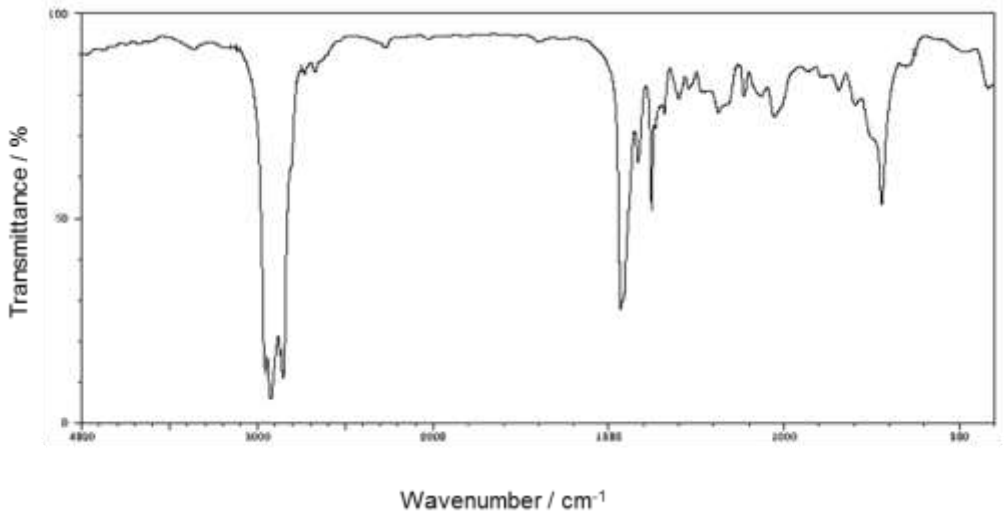


Figure 1 IR spectrum of TOP

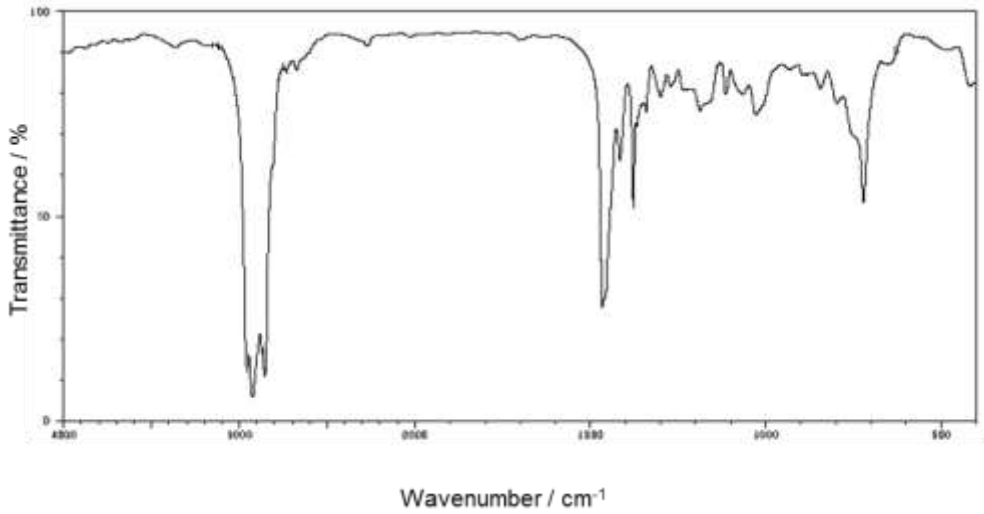


Figure 2 IR spectrum of $(C_8BzIm)_2Py]_2Br_2$